PL-TR-94-2133

AD-A283 245

E 2 0 2 1M

Monitoring Research at the Center for Seismic Studies

M. Ya Balbachan
J. Coyne
M.B. Gokhberg
L. Grant
A. Henson
H. Israelsson

C. Romney
V. Ryaboy
F. Ryall
V. I. Tskanovskii
R. Willemann

Science Applications International Corporation
Center for Seismic Studies
1300 N. 17th Street, Suite 1450
Arlington, VA 22209

DTIC
S ELECTE
JUL 2 6 1994
F

27 April 1994

Final Report
August 1993 - December 1993

Approved for Public Release; Distribution Unlimited

94-23454

PHILLIPS LABORATORY
Directorate of Geophysics
AIR FORCE MATERIEL COMMAND
HANSCOM AIR FORCE BASE, MA 01731-3010

94 7 25 110

DTIC QUALITY INSPECTED

This technical report has been reviewed and is approved for publication.

_____
JAMES F. LEWKOWICZ
Contract Manager
Earth Sciences Division
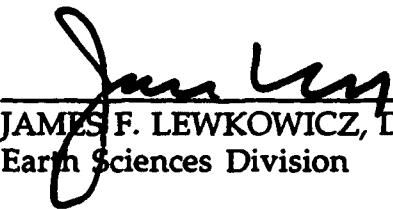
_____
JAMES F. LEWKOWICZ, Director
Earth Sciences Division

REPORT DOCUMENTATION PAGE

Public reporting burden for this collection of information is estimated to average 1 hour per response, including the time for reviewing instructions, searching existing data sources, gathering and maintaining the data needed, and completing and reviewing the collection of information. Send comments regarding this burden estimate or any other aspect of this collection of information, including suggestions for reducing this burden, to Washington Headquarters Services, Directorate for Information Operations and Reports, 1215 Jefferson Davis Highway, Suite 1204, Arlington, VA 22202-4302, and to the Office of Management and Budget, Paperwork Reduction Project (0704-0188), Washington, DC 20503.

1. AGENCY USE ONLY (Leave blank)	2. REPORT DATE April 27, 1994	3. REPORT TYPE AND DATES COVERED Final (August 1993 – December 1993)

4. TITLE AND SUBTITLE

Monitoring Research at the Center for Seismic Studies

5. FUNDING NUMBERS
F19628-93-C-0194

PE62301E
PRNM93 TA GM
WU AM

6. AUTHOR(S)

M. Ya Balbachan*	A. Henson	F. Ryall
J. Coyne	H.Israelsson	V.I. Tskanovskii**
M.B.Gokhberg*	C.Romney	R. Willemann
	V.Ryaboy	

7. PERFORMING ORGANIZATION NAME(S) AND ADDRESS(ES)

Science Applications International Corporation
Center for Seismic Studies
1300 N. 17th Street, Suite 1450
Arlington, VA 22209

8. PERFORMING ORGANIZATION REPORT NUMBER

C94-03

9. SPONSORING/MONITORING AGENCY NAME(S) AND ADDRESS(ES)

Phillips Laboratory
29 Randolph Road
Hanscom AFB, MA 01731-3010

Contract Manager: James Lewkowicz/GPEH

10. SPONSORING/MONITORING AGENCY REPORT NUMBER

PL-TR-94-2133

11. SUPPLEMENTARY NOTES

* Institute of Physics of the Earth,Russian Academy of Science
** Institute for Dynamics of the Geospheres, Russian Academy of Science

12a. DISTRIBUTION/AVAILABILITY STATEMENT

Approved for Public Release
Distribution Unlimited

12b. DISTRIBUTION CODE

13. ABSTRACT (Maximum 200 words)

Several of the reports included herein are essentially preliminary progress reports. This report includes a description of a strategy for optimizing the station specific parameters used for automatic processing of data from individual stations; the developmnet of an improved mean regional travel time curve for Pn appropriate for stations connected to the IMS; the study of an event detected by the IMS; an update to a report describing a Ground Truth Database; and reports describing work initiated to exploit data from large mining blasts in the Former Soviet Union.

14. SUBJECT TERMS

IMS
Travel Time Curves
Deep Seismic Sounding Data
Ground Truth Database   Tyrnyauz
Lop Nur
Global Network

15. NUMBER OF PAGES
142

16. PRICE CODE

17. SECURITY CLASSIFICATION OF REPORT UNCLASSIFIED	18. SECURITY CLASSIFICATION OF THIS PAGE UNCLASSIFIED	19. SECURITY CLASSIFICATION OF ABSTRACT UNCLASSIFIED	20. LIMITATION OF ABSTRACT SAR

Table of Contents

List of Figures

List of Tables

Report Summary

This report documents work on several subtasks of a nuclear monitoring research program initiated in August 1993, but terminated in December 1993. For that reason, several of the reports included herein are essentially preliminary progress reports.

An important thrust of the research program was to develop improvements to the Center for Seismic Studies' operational system, the Intelligent Monitoring System (IMS). This report includes a description of a strategy for optimizing the station-specific parameters used for automatic processing of data from individual stations, and illustrates this strategy by a case study of its application to two stations. Another study reports on the development of an improved mean regional travel time curve for Pn appropriate for stations connected to the IMS and on a method for inferring local corrections to this mean curve. This study also applies Deep Seismic Sounding data from the region to demonstrate that phases commonly identified as Pg and Lg are actually PmP and SmS, and that application of this knowledge to epicenter determination removes a bias in distance previously noted in IMS results.

The report includes a study of an event detected by the IMS, possibly on the Lop Nur nuclear testing site based on IMS Data alone. The importance of data contributed by a global network was demonstrated by establishing with high confidence that the event did not occur at previously known explosion testing areas, and occurred at a depth inconsistent with nuclear testing.

A previous report described a Ground Truth Database, consisting of waveforms and carefully measured phase parameters from events independently known to be earthquakes, or known to be explosions or explosion-related. This report updates the previous report, adding additional events that may be found to be useful for event discrimination research.

Finally, this report describes work initiated to exploit data from large mining blasts in the Former Soviet Union (the Tyrnyauz Mine in the Northern Caucasus) to improve location and discrimination of seismic events. The work was done in cooperation with scientists of the Russian Institute of Physics of the Earth and Institute for Dynamics of the Geospheres, Russian Academy of Sciences. Their attempts to measure mechanical-electrical-magnetic phenomena and to provide precise data on the sequence of ripple-fired explosions are included here. Additional work on this latter topic, accomplished jointly with scientists of SMU, will be reported elsewhere in a report on Contract F29601-91-D-DB20.

Tuning of Detection and Feature Extraction for the GSETT-3 IDC

Anne Suteau-Henson and Ray Willemann

Summary

This report describes a strategy developed to rapidly optimize the parameters ("tuning") used for automated processing of data from candidate seismic stations for the global network proposed for *GSETT-3*, an experiment planned by the Group of Scientific Experts of the Conference on Disarmament. The application of this strategy to the tuning of detection and feature extraction is outlined here. The tuning of other automated processes (including, for example, phase identification and magnitude estimation) is beyond the scope of this report. The following topics are addressed here:

- objectives of the tuning process in relation to the new GSE concepts;

- selection of an appropriate set of continuous waveform data to be requested from each station for initial tuning purposes;

- automated signal processing of tuning data, using standardized sets of processing parameters ("recipes");

- analyst review of the results of automated signal processing;

- optimization of the detector, and of the measurement of useful characteristics of detected signals ("feature extraction"), such as polarization attributes;

- tuning update as new data become available.

The proposed strategy is illustrated with a *case study*: the actual tuning of feature extraction at two stations, as it was performed for the first prototype of the *GSETT-3* International Data Center (IDC).

Introduction

The Group of Scientific Experts (*GSE*) of the Conference on Disarmament is planning a third Technical Test of its concepts for a global nuclear monitoring network ("*GSETT-3*"). This network will include three different classes of stations: "*alpha*" (about 50), which transmit continuous waveform data to the IDC, where they are used for detec-

1

tion and location of events; *"beta"* (75 to 150), providing waveform segments requested by the IDC for refinement of locations of regional events formed from the *alpha* network data; and *"gamma"*, supplying additional regional data to further improve the near real-time bulletin produced by the *alpha-beta* network. A small prototype network has been used since May 1993 at the International Data Center (IDC) of the *Center for Seismic Studies,* for an experiment referred to here as "V0", Version 0 of the IDC Testbed (GSE/US/85, 1993; Stead *et al.,* 1993).

Candidate *alpha* and *beta* stations for the *GSETT-3* network need to be evaluated. For each selected station, optimized parameters for automated processing must be determined (we refer to this process as "tuning" the station). The advantages of determining station-specific processing parameters for detection, feature extraction, phase identification, location, and magnitude estimation have been demonstrated in previous work (e.g., Suteau-Henson, 1991; Riviere-Barbier *et al.,* 1992; Suteau-Henson *et al.,* 1992). Here, we build on this previous experience with knowledge acquisition to develop standardized and automated tuning methods that can be used to improve the IDC system performance.

This report describes the strategy developed for rapidly evaluating, selecting and tuning *GSETT-3* candidate stations. It is based on experience acquired during V0. The following requirements for tuning emerge from the new GSE concepts:
- *rapid knowledge acquisition:* region-specific knowledge for each of the many

  stations of the proposed global network must be rapidly acquired and incorpo-

  rated into the IDC system;

- *optimized automated processing:* large volumes of data will be processed near

  real-time to produce event bulletins, so the best possible automated bulletin must

  be obtained to reduce the human analysis load.

The strategy described here reflects our attempts at meeting these two requirements. An iterative approach is proposed. First, an initial tuning is performed, using an appropriate data set of continuous waveform data. Then, updates are performed, by "re-tuning" stations already used in the experiment, by adding new data that have become available. This process is repeated until a given performance goal is achieved or no further improvement can be obtained.

Selecting Initial Tuning Data

The first step in tuning a candidate *GSETT-3* station consists of requesting a set of continuous waveform data from the station. This is done preferably before the station starts being used in the experiment (i.e., before the start of data transmission), for the following reasons:

- some initial tuning can be performed, so that tuned parameters can be used as soon as the station comes on-line;

- the analysts have the opportunity to familiarize themselves with the station before they have to analyze data from it in near real-time;

- the station can be evaluated.

The following requirements drive the selection of initial tuning data sets:

- for a given station, the tuning data must produce detections (from noise, real seismic signals, and coda) forming a sample representative of the detections that will be produced at this station during the experiment;

- recent data are preferred, because they are more likely to reflect the conditions (instrumentation, noise, natural and industrial seismic activity) that will prevail at the station during the experiment;

- efficient use must be made of the analyst's time during the review of the results from automated processing of the tuning data, as this analyst review is the most labor-intensive part of the tuning process.

The first and third requirements prompt us, whenever feasible, to select specific time periods for tuning purposes. Using bulletin information (e.g., from NEIS and/or regional catalogs), time periods can be selected on the basis of their including a sizeable set of representative events. Because of the second requirement, the most recent data offering a good event selection are preferred. Also, the instrumentation at the station (and configuration for arrays) during the time period covered by the tuning data must be identical to that in effect during the actual experiment.

Based on our experience, a representative data set that can be used for initial tuning of detection and feature extraction should provide:

- at least 100 noise detections, spanning at least a whole continuous 24 hours, on a week day;

- at least 30 detections of real seismic signals representing each phase type

3

(regional P, regional S, teleseismic).

The requirements for the second category (real signals) are somewhat different for *alpha* and *beta* stations. During the IDC V0 experiment, data from a particular *beta* station were requested only when an event had been detected and located within 5° of the station by the IDC based on the *alpha* network data. Therefore, relevant arrivals were local / regional P and S phases. *Alpha* stations, however, can detect and locate events from any epicentral distance, and thus teleseismic signals are also relevant. Because of the density of the *alpha* network, emphasis is put on the far-regional range.

To be representative, the sample of events included in the tuning data set ideally should cover a variety of distances (within the range relevant for the station type), azimuths and signal-to-noise ratios (SNR). In practice, data sets biased toward a particular epicentral location should be avoided.

An initial tuning data set can be obtained through a request for continuous waveform data covering a time period of a few days to a few weeks. Although such a data set may not always be representative enough, this shortcoming can be remedied by performing tuning updates during the experiment, as described in a later section.

Processing and Analysis of Tuning Data

Automated Signal Processing

The waveform data selected for tuning are run through an automated signal processor (*SigPro*), including a detector and a post-detection processor that measures detection characteristics (Bache *et al.*, 1990). Standard recipes are used for a given type of station (such as three-component, broad-band, sampled at 20 Hz). As detector optimization is performed based on results from this process, the detector recipes should include a number of "beams" filtered in overlapping narrow frequency bands, with detection thresholds set low so as to minimize the number of missed real arrivals. This is described in more detail in the section on detector optimization.

Analyst Review

The results from automated signal processing are then reviewed by an experienced seismic analyst. The objectives of this analyst review are as follows:

- perform final identification for a representative sample of detections (noise, signal, and coda);

- evaluate the station, in terms of noise and signal characteristics, any specific

problems (noise, timing), seismic activity.

In practice, the first objective requires the following steps:

- analyze at least one day of continuous data, identifying each detection (including noise), and adding any missed real signal;

- analyze time segments containing events of interest for the remaining days, identifying each detection, and adding any missed real signal.'

To save time and ease the task of the analysts, it is useful to make available to them any relevant event bulletins (NEIS, regional catalog). This also helps insure the accuracy of phase identification from analyst review, which is important because it is the reference against which the performance of automated processing is evaluated.

Optimization

Detector

The first step in tuning *per se* consists of optimizing the detector. A method to perform detector optimization was developed and is summarized here. For every detection, SNR is measured on every filtered detection "beam" from the appropriate standard recipe, using the lowest threshold that might be useful on this beam to detect real signals. The optimum thresholds are those that minimize the function:

$$F(t) = Ff(t, n) + \sum_{i=1}^{n_p} w_i \times Ft(t, p_i) + \sum_{j=1}^{n_b} (t_j - 10)^2 / 1000$$

where t is a vector of beam thresholds, n represents noise detections and p_i real arrivals, n_b is the number of beams, n_p is the number of real phase types, and w_i are weights that reflect the importance of detecting each phase type. The functions Ff and Ft are ramp functions that increase when the thresholds detect "false" arrivals or fail to detect "true" arrivals, respectively. The purpose of the last term is to stabilize the minimization algorithm with respect to thresholds outside the SNR range of the tuning data.

At three-component stations, the optimization is performed using different options for the "beams" formed from the vertical, north-south and east-west channels (Z, N, E, respectively), and the rectified sum of the horizontal channels (H). For example, the following beams can be used:

- Z, N, E, H, with thresholds set independently;

- Z, N, E, H, constraining the thresholds for N and E to be equal;

- Z, H, with independent thresholds.

Clearly, not all of these options have the advantage of avoiding azimuthal bias. Directional preferences, however, may be desirable for some stations, to take advantage of any knowledge about specific directions for noise or seismic sources.

Feature Extraction

In order to optimize automated phase identification, it is important to first perform the best possible measurement of characteristics ("feature extraction") for each detection. A feature extraction process is considered as optimized when it results in the best classification of detections of different types (i.e., noise, regional P, regional S, and, for *alpha* stations, teleseismic), the identification given by the analyst being used as reference.

For an array station, the most useful feature extraction process for phase identification is *f-k* analysis (or any other process deriving the slowness vector from the 2-D wavefield). For a three-component station, the equivalent process is polarization analysis.

The optimization consists of exploring the parameter space for the recipe used, and selecting the set of parameters that results in the best classification performance. In practice, our experience with data from a variety of stations makes it possible to place reasonable limits on the range of the various parameters explored. To optimize polarization analysis, for example, a set of 45 standard recipes has been developed for data sampled at up to 80 Hz (see case study below).

The data set of detections used for optimization of feature extraction is a subset of that produced by the standard detector used for detector optimization. It includes only those noise and coda detections that passed the detection test of the *optimized* detector, as they are those relevant for phase identification.

In practice, this optimization requires the following steps:

- re-run the post-detection processor (such as polarization or *f-k* analysis) off-line

  for each detection in the selected set and for each of the standard recipes;

- for each recipe, automatically classify each detection using, for example, classi-

  cal discriminant analysis (Suteau-Henson, 1991);

- select the recipe with the highest classification performance.

Following tuning of feature extraction, tuning of automated phase identification

6

can be performed using a set of detections (and their characteristics) derived after optimization of detection and feature extraction. For example, tuning of initial phase identification at a station of the three-component or small-array type consists of training a neural network (Patnaik *et al.*, 1992; Sereno and Patnaik, 1993). As this optimization process requires a larger set of detections in each phase type than the previous two, it is performed when enough data (from the initial tuning set and from the experiment itself) have become available for a given station. The process of re-tuning after adding new data to the initial data set to increase the sample size is described in more detail in the next section. Further description of the tuning of phase identification is beyond the scope of this work.

Tuning Update

In the previous sections, we addressed the tuning of a station using an initial data set. As more data from this station become available during the experiment itself (continuous data from *alpha* stations and event segments from *beta* stations), it is advantageous to update the tuning by adding such data to the initial set, because:

- this increases the size of the tuning data set, also making it possible to tune processes requiring larger data sets, such as phase identification;

- this increases the quality of the tuning data set, as data from the actual experiment are more relevant;

- the new data are already analyzed as part of routine IDC operations.

In particular, re-tuning is necessary when upgrades have been made to a station. In order to avoid inconsistencies, automated processes should be re-tuned in the same order as that in which these processes occur in the operational data processing pipeline. For example, the tuning of initial phase identification (e.g., training of station-specific neural networks) should be performed using data derived from running an optimized detector and an optimized feature-extraction process.

A Case Study: Polarization Tuning of GRSN Stations MOX and BRG

The proposed tuning method is illustrated with the optimization of polarization analysis at two three-component stations from the German Regional Seismic Network, "GRSN" (GSE/Federal Republic of Germany/39, 1991). These stations, MOX and BRG, are located about 2° north of the GERESS array, in an area with a high level of industrial seismic activity. During V0, they have been used as *beta* stations, the nearest *alpha* station being GERESS. For the purpose of initial tuning, two and three days of continuous data were obtained from MOX and BRG, respectively. The tuning was later updated by adding

events from fifteen days of data recorded during V0, within the period from May 18 to June 20, 1993. Figure 1 shows the locations of the events recorded at MOX and BRG during that period of the experiment.

Polarization analysis was optimized by comparing the performance for classifying noise detections, regional P and regional S, of 45 recipes, spanning a wide range of processing parameters. The most sensitive parameter was found to be the frequency band used in the analysis. Bands including frequencies up to 2, 4, 8, 16, and 32 Hz were tried. The high sample rate (80 Hz) made it possible to investigate the usefulness of high frequencies (16-32 Hz). Note that only results from polarization analysis were used in the classification, and that including other information (such as context) would improve the resulting performance.

The classification performance of the 45 recipes was compared for MOX before and after the tuning update (Figure 2). Figure 3 compares the tuning results for MOX and BRG after the update. Table 1 gives the number of detections used for optimization in

Table 1: Number of Detections for Polarization Tuning at MOX and BRG

Station	Noise	Regional P	Regional S
MOX (initial tuning)	41[a]	21	44
MOX (initial tuning + V0)	81	86	80
BRG (initial tuning + V0)	80	59	88

a. half of the available noise detections were used

each case. At MOX, the update confirms the tuning results based on the initial set (that was somewhat deficient in regional P phases), with a better performance and a higher confidence (Figure 2). Figure 3 shows that at BRG, classification performance is optimized when only frequencies up to 4 Hz are included in the analysis. Such importance of low frequencies at this station (the teleseismic band) is in agreement with the observation that it is the GRSN station contributing the most to the ISC (Manfred Hunger, personal communication). At MOX, the use of frequencies above 8 Hz does not improve the classification performance.

A second update was performed for BRG by adding data obtained during the experiment within the period from June 21 to October 27, 1993. This update confirmed the results of the previous one, which indicates that, in this case, no further improvement was obtained by re-tuning again.
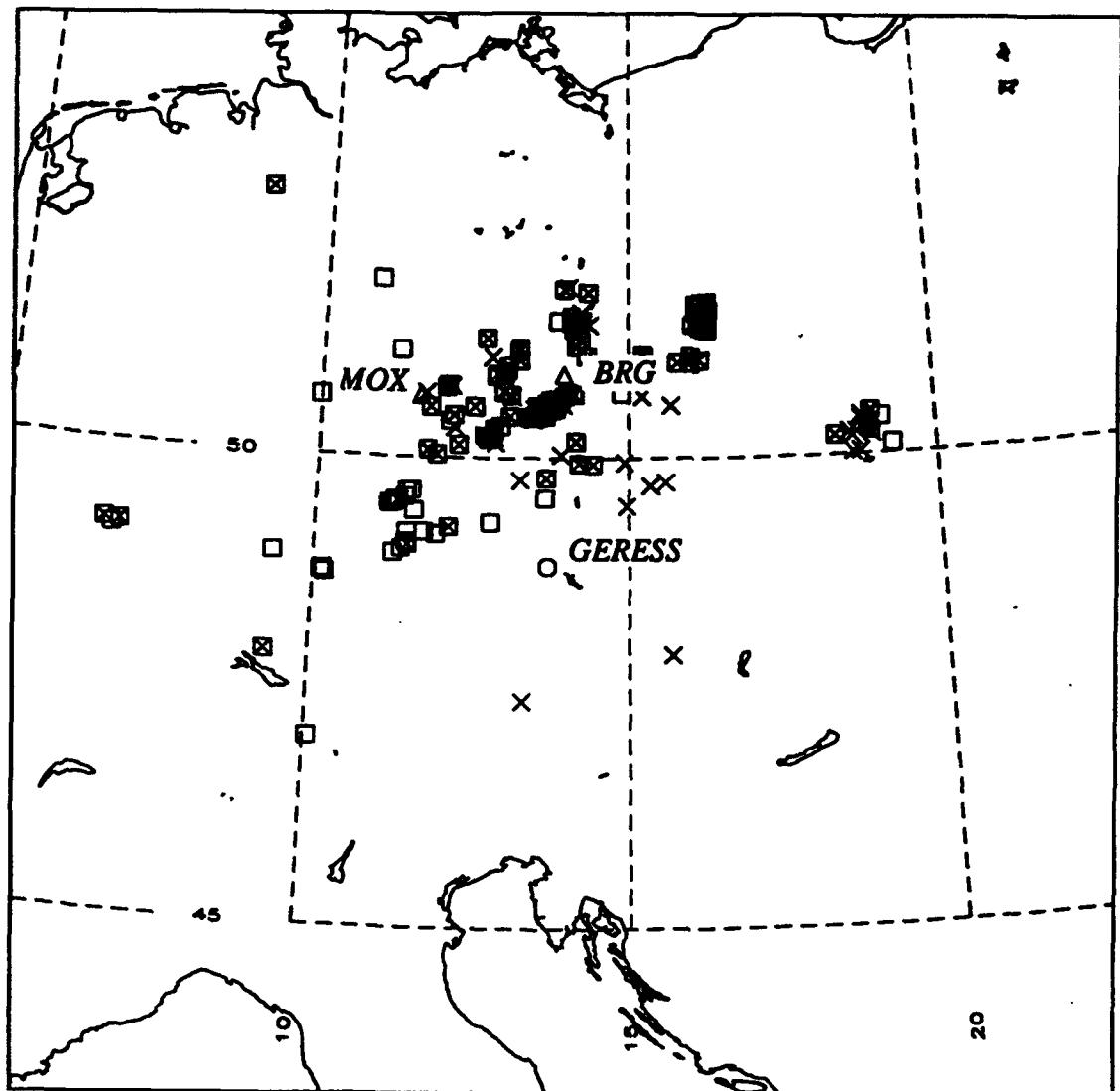
Figure 1: Locations of regional events recorded at *beta* stations MOX (squares) and BRG (crosses) during 15 data days of V0. Triangles denote MOX and BRG, and the circle indicates the GERESS array, used as an *alpha* station.
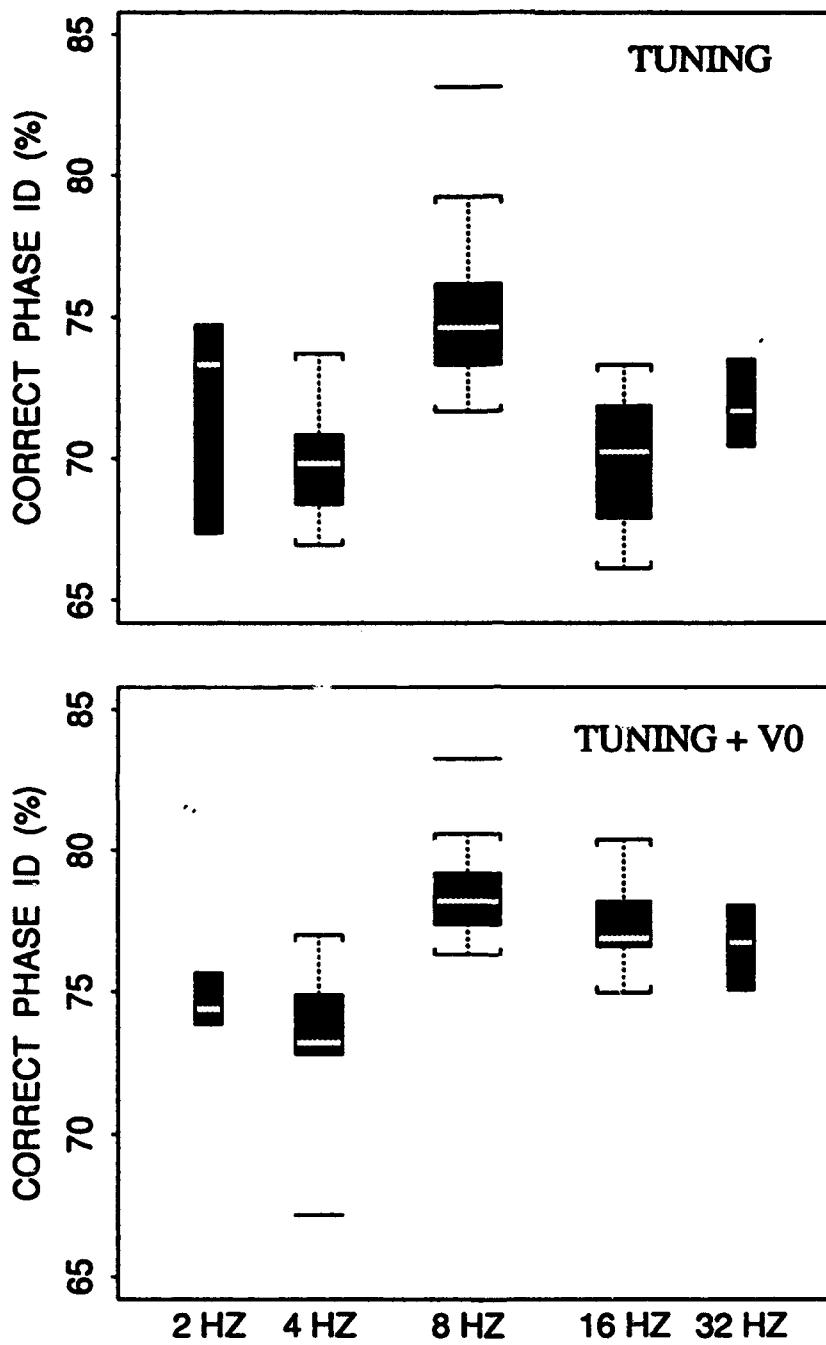
Figure 2: Boxplots describing the distributions of the percentage of correct phase identification at station MOX for polarization recipes grouped by high cutoff of the frequency band used in the analysis. The *top* plot is for the initial tuning set. The *bottom* plot is for a data set including the initial tuning set and 15 days of data obtained during V0.
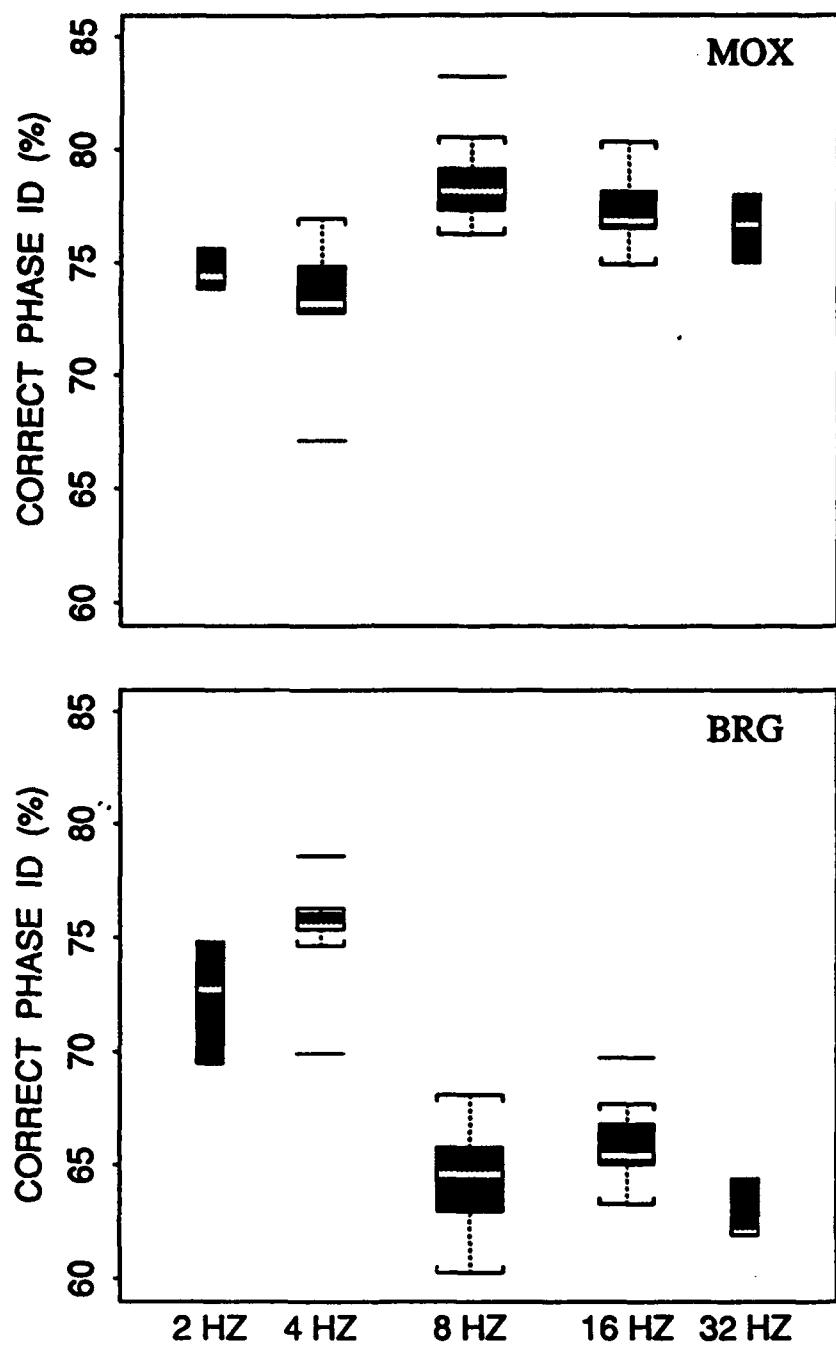
Figure 3: Boxplots describing the distributions of the percentage of correct phase iden-tification for polarization recipes grouped by high cutoff of the frequency band used in the analysis. Both initial tuning data and V0 data were used, for station MOX (*top*), and BRG (*bottom*).

Evaluation and polarization tuning were also performed for other three-component stations used as *beta* stations during V0, as described in Suteau-Henson *et al.*, 1993. In particular, ten GRSN stations were evaluated, and six were selected, including MOX and BRG. At five GRSN stations, a large enough data set was available to tune polarization. A comparison of classification performance as a function of the frequency band used in the analysis shows that, for all stations except BRG, the best results are obtained when using frequencies up to 8Hz.

Conclusions and Recommendations

The proposed strategy for tuning candidate stations for *GSETT-3* has the advantage of helping meet the requirements for rapid knowledge acquisition and optimized automated processing of large volumes of data. An iterative and mostly automated approach makes it possible to start tuning a new station before it is incorporated into the network, and progressively improve this tuning as more data become available during the experiment. Tuning updates can also be performed by using new recipes or new algorithms, with the aim of further improving the automated processing. In practice, we expect that at some point the performance improvement obtained by re-tuning a given station will become negligible. Then, no re-tuning will be needed unless some changing conditions at the station call for further updates.

The proposed approach was described in more detail for the case of optimization of detection and feature extraction. It is, however, a general approach that can be applied to the tuning of other automated processes as well. Also, "metrics" can be developed to objectively quantify the improvement achieved after tuning. This is the object of current and future work aiming at improving the IDC performance.

References

Bache, T. C., S. R. Bratt, J. Wang, R. M. Fung, C. Kobryn, and J. W. Given (1990). The Intelligent Monitoring System, *Bull. Seism. Soc. Am.* **80**, Part B, 1833-1851.

GSE/Federal Republic of Germany/39 (1991). Lessons Learned From GSETT-2, *Technical Presentation at the 32nd Session of the GSE*, Geneva, August 7, 1991.

GSE/US/85 (1993). Proposed Testbed for IDC Development, *United States Delegation to the UN Conference on Disarmament*, February 1993.

Patnaik, G. B., T. J. Sereno, and R. D. Jenkins (1992). Test and Evaluation of Neural Network Applications for Seismic Signal Discrimination, *Final Report* No. PL-TR-92-2218(II), Phillips Laboratory, ADA260030.

Riviere-Barbier F., A. Suteau-Henson, V. Z. Ryaboy, and J. A. Carter (1992). Analysis of Three-Component Data From IRIS/IDA Stations in the USSR, *Bull. Seism. Soc. Am.* **82**, 192-220.

Sereno, T. J. and G. B. Patnaik (1993). Initial Wave-Type Identification with Neural Networks and its Contribution to Automated Processing in IMS Version 3.0, *Special Technical Report* SAIC-93/1219, 37 pp.

Stead, R. J., R. J. Willemann, and J. R. Bowman (1993). Operation of a Testbed International Data Center for the Group of Scientific Experts Third Technical Test (GSETT-3), *Trans. Am. Geophys. Union*, p. 446 (abstract).

Suteau-Henson, A. (1991). Three-Component Analysis of Regional Phases at NORESS and ARCESS: Polarization and Phase Identification, *Bull. Seism. Soc. Am.* 81, 2419-2440.

Suteau-Henson, A., V. Z. Ryaboy, H. Israelsson, and J. A. Carter (1993). Station Evaluation and Accurate Event Locations for Global Monitoring, *Proceedings of the 15th Annual Seismic Research Symposium*, 8-10 September 1993, Vail, Colorado, 377-383, PL-TR-93-2160, ADA271458.

A Note on an Event in the
Xinjiang Province, China on April 14, 1993

Hans Israelsson

Introduction

On April 14 1993 IMS detected and located a small event (mb=4.3) with an error ellipse that covered the Lop Nur Nuclear Weapons Test Base in the Xinjiang Province of/ China. Because of the uncertainty of the location and the proximity of the Lop Nur test base to active seismic regions the nature of the source cannot readily be established on the location alone. Furthermore, the waveforms at the IMS arrays were more complex than those of previously observed nuclear explosions at Lop Nur (Bratt, 1993).

In this note we have attempted to reduce the uncertainty of the IMS location and compile data to facilitate identification of the source. In doing so we were drawing upon data recorded at additional stations that were requested from National Data Centers in several countries and retrieved from the IRIS/DMC.

Data

The map in Figure 4 shows the 95% confidence ellipse of the epicenter estimated from arrival times, azimuths, and slowness values of primary and secondary phases at four of the IMS arrays, APA0, ARA0, FIA0, and NRA0 (Table 2) as available in the IMS data base at the Center for Seismic Studies. The area of the ellipse is about $900,000 \text{ km}^2$.

The map also shows the four IMS arrays and other stations which recorded the event. These include the arrays ASAR and WRA in Australia and YKA in Canada, all at teleseismic distances, and the station WMQ in the Xinjiang Province of China, at a local distance from the preliminary IMS epicenter estimate.

Waveforms

Figure 5 shows the short period beams recorded at the IMS arrays. The beam for NRA0 is unfiltered whereas the beams of the other arrays were filtered between 1.5-4.0 Hz. The arrival times of the first and secondary phases as reported in the IMS data base, are marked in the record sections. The secondary phases, detected on the beams at all four arrays, albeit with varying SNR, are delayed about 11 s relative to the first arrival time. The f-k spectra of the primary and secondary phases were in general agreement suggesting that the two phases originated from the same source region.

SNR and dominant frequency of the primary and secondary phases vary significantly among the arrays. The beam at NRA0 had the largest SNR and the initial P signal at

IMS LOCATION AND 95 PER CENT CONFIDENCE ELLIPSE

PROJECTION: LAMBERT.   CENTER: 41.60   85.81   0.0
WINDOW ANGLES   60.0000   60.0000   60.0000   60.0000
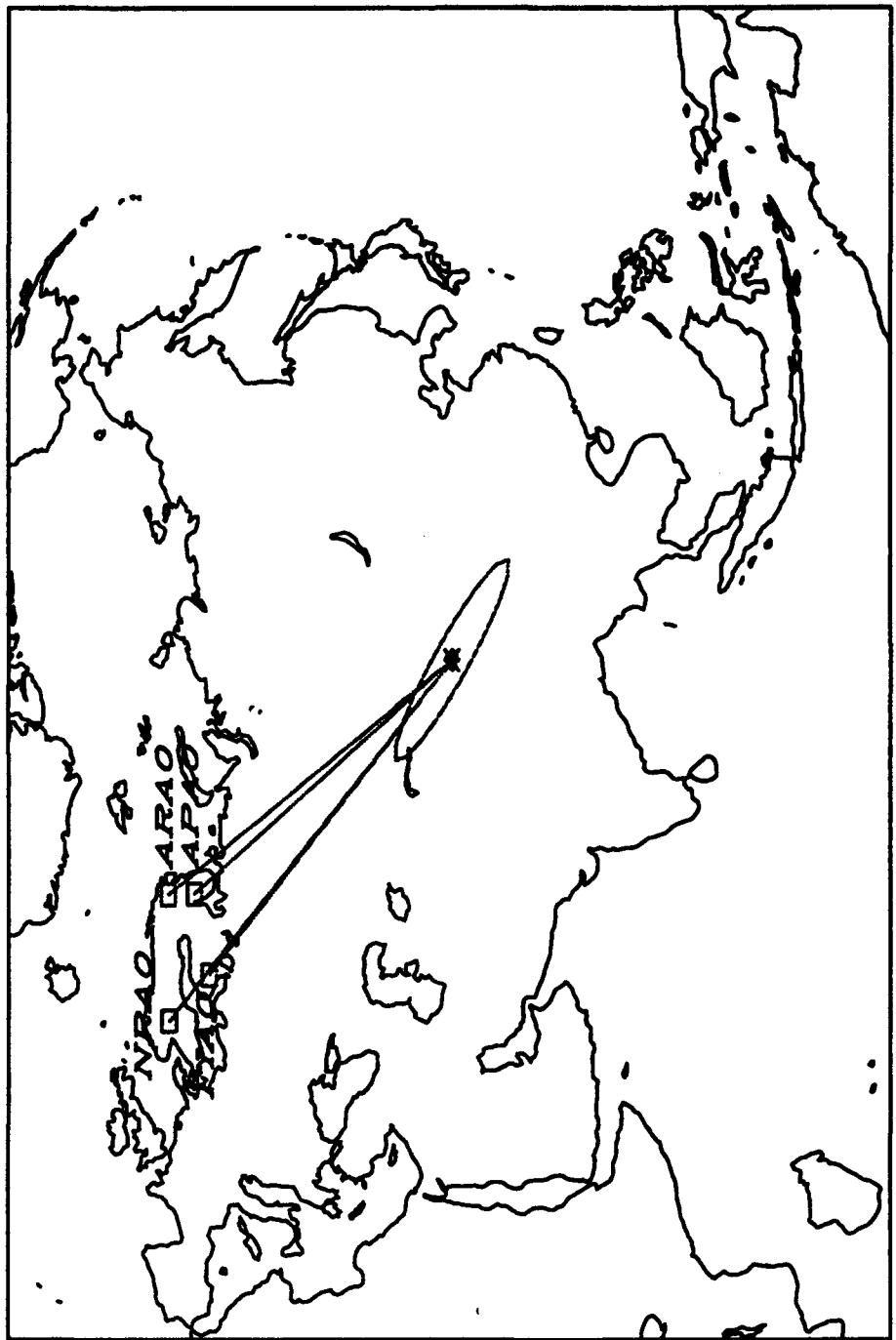
Figure 4:   The 95% confidence ellipse of the epicenter of the event on April 14, 1993 and the relative location
            of the four IMS arrays, APA0, ARA0, FIA0, and NRA0.

BEAMS AT IMS ARRAYS FOR 93/04/14 event
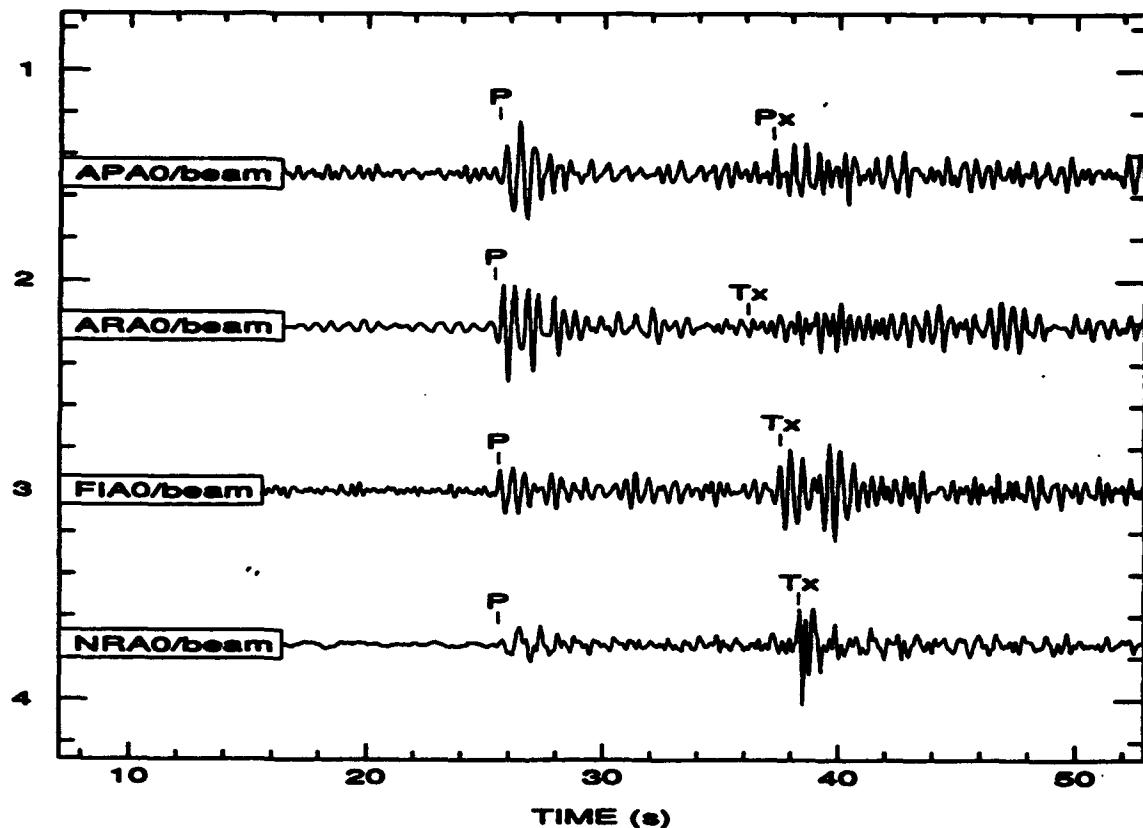
Figure 5:   Short period phase beams of the event on April 14, 1993, at the four IMS arrays, APA0, ARA0, FIA0, and NRA0. The beam at NRA0 is unfiltered whereas the beams at other arrays were band pass filtered between 1.5-4.0 Hz.

Table 2: Reported arrival data

Station	Phase	Time	SD	Azimuth	SD	Slown.	SD
APA0	P	8:38:23.7	2.3	93.2	16.8	–	–
APA0	Tx	8:38:35.3	3.8	100.7	6.4	–	–
FIA0	P	8:38:43.4	3.7	84.1	22.6	6.86	5.72
ARA0	P	8:38:49.3	1.0	87.5	14.2	8.70	5.06
NRA0	P	8:39:39.4	1.0	77.1	13.8	6.22	3.53
NRA0	Tx	8:39:52.1	1.0	76.7	13.6	–	–
YKA	P	8:42:38.3	1.0	–	–		
WMQ	P	8:31:30.0	2.0	–	–		
WMQ	S	8:31:44.7	2.0	–	–		
WRA	P	8:42:52.5	1.0	–	–		
WRA	pP	8:43:01.2	1.0	–	–		
ASAR	P	8:43:08.0	1.0	–	–		
ASAR	pP	8:43:16.5	1.0	–	–		

NRA0 had a strikingly lower dominant frequency than those of the other arrays.

Waveform segments of all array elements and beams and f-k spectra were received via FAX for the Australian arrays ASAR and WRA (Muirhead and Penders, private communication, 1993), which are reproduced in Figure 6. Again clear secondary phases are developed, however, now delayed with only about 8 s after the initial P. As for the IMS arrays the f-k spectra of the primary and secondary phases were in general agreement.

Three component recordings at the Chinese station WMQ retrieved from the IRIS DMC are shown in Figure 7 . The large amplitude S wave dominates the recordings. The initial P wave had a rectilinearity close to 1.0 with back azimuth (about 190°) and inclination angle (20°) well defined. The S phase is, on the vertical and north component, preceded with about 1 s by a phase with high rectilinearity and also well defined back azimuth and angle of inclination similar to that of the initial phase.

Other Data

A first arrival time at the array YKA in Canada was provided along with location and magnitude (North, private communication, 1993). The IMS array GEA0 did not detect the event automatically and signals that could be positively associated with the event
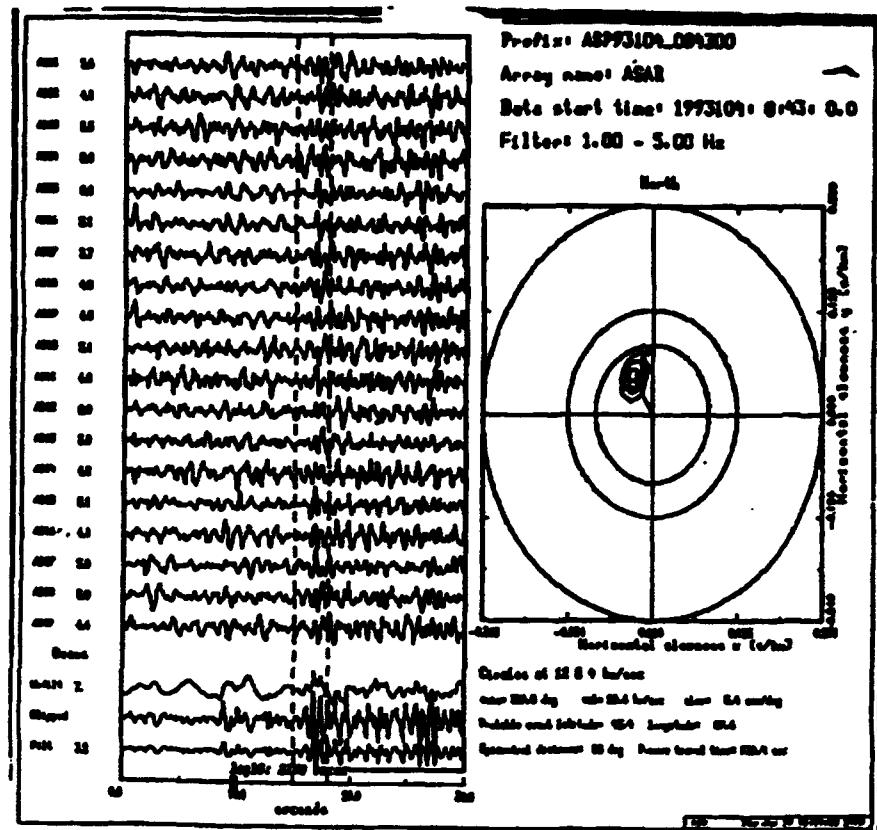
Figure 6: .Single element traces and beams filtered and unfiltered at the Austra-
lian array ASAR of the event on April 14, 1993. The f-k spectrum for
the time window indicated on the filtered beam is shown to the right
in the figure.

RECORDINGS AT WMQ OF 93/04/14 EVENT
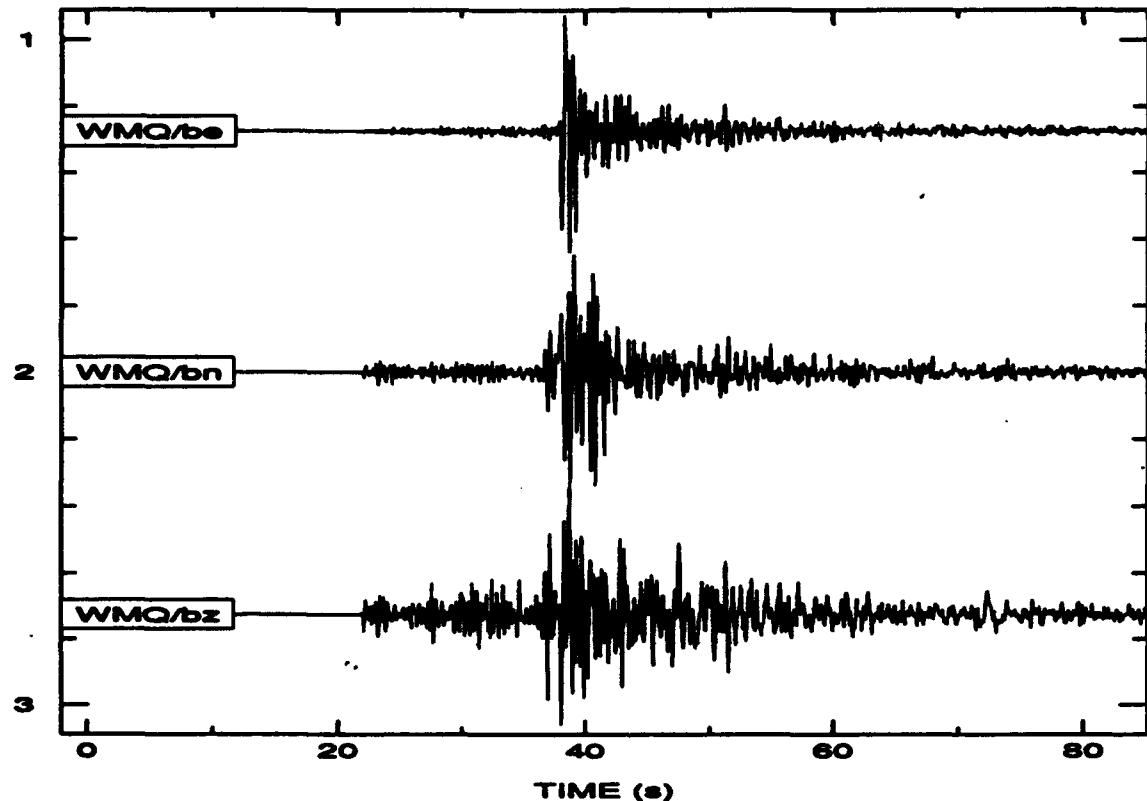
Figure 7: Three component broad band recordings at the Chinese station WMQ of the event on April 14, 1993.

could neither be found in a subsequent analysis (Henger, private communication, 1993). At the IRIS DMC there were no data for a time window of expected arrival times for P or S phases at any Chinese stations other than WMQ. A request was also made for data at the station NIL in Pakistan, which recorded the Lop Nur explosion of 92/09/25 with a very large signal-to-noise, but so far no response has been received.

Location

All locations were made with the LocSAT program that is employed by the IMS. In addition to the epicenter the program estimates a confidence ellipse that depends partly on the *a priori* or assumed standard deviations of the errors of measured arrival times, back azimuths and slowness values. The standard deviations in the CSS data base were used for the measurements at the IMS arrays. The arrival times at the other stations were assigned values listed in Table 2. As the a priori standard errors of back azimuths and slowness/incidence angle for ASAR and WRA and for WMQ could not be readily estimated, only the arrival times at these stations were used in the event locations.

The 95% confidence ellipse in Figure 4 of the initial IMS solution is based only on data at four IMS arrays including arrival times, slownesses and back azimuths for primary and secondary phases. No convergence was obtained if the IMS data were limited to first arrival times. Figure 5 shows how the confidence ellipse is reduced - the length of the major axis goes from 1200 to 35 km - as data at the other stations are added in the order (1) YKA, (2) WMQ, and (3) ASAR/WRA. The standard deviation of the arrival time residuals for the solution based on all available station data was 0.62 s.

Phases P and S- instead of Pg and Sg - were used for WMQ in the location as the IMS travel time tables for Sg did not extend to depth below 5 km. Solutions with Pg and S yielded very similar results. Figure 6 compares the velocity model used by LocSAT for local and regional stations with that obtained by Barker (1992) for SSE from WMQ.

The area of the 95% error ellipse for the location based on all station data is about 1300 km^2, and the standard errors in latitude and longitude were 7 and 13 km respectively. These standard errors are comparable to those reported by NEIS for its epicenter determinations of earthquakes in the area with magnitude, mb, less than 5.

Data With Bearing on the Nature of the Source

In order to facilitate ascertaining the nature of the source of the 93/04/14 event, we have compiled data according to a simple "screening" principle commonly used for event identification: (1) epicenter, (2) focal depth, and (3) characteristics of recorded waveforms.

CONFIDENCE ELLIPSES WITH ADDITIONAL DATA

PROJECTION: LAMBERT. CENTER: 41.44 90.15 0.0
WINDOW ANGLES 8.0010 8.0010 8.0010 8.0010 8.0010
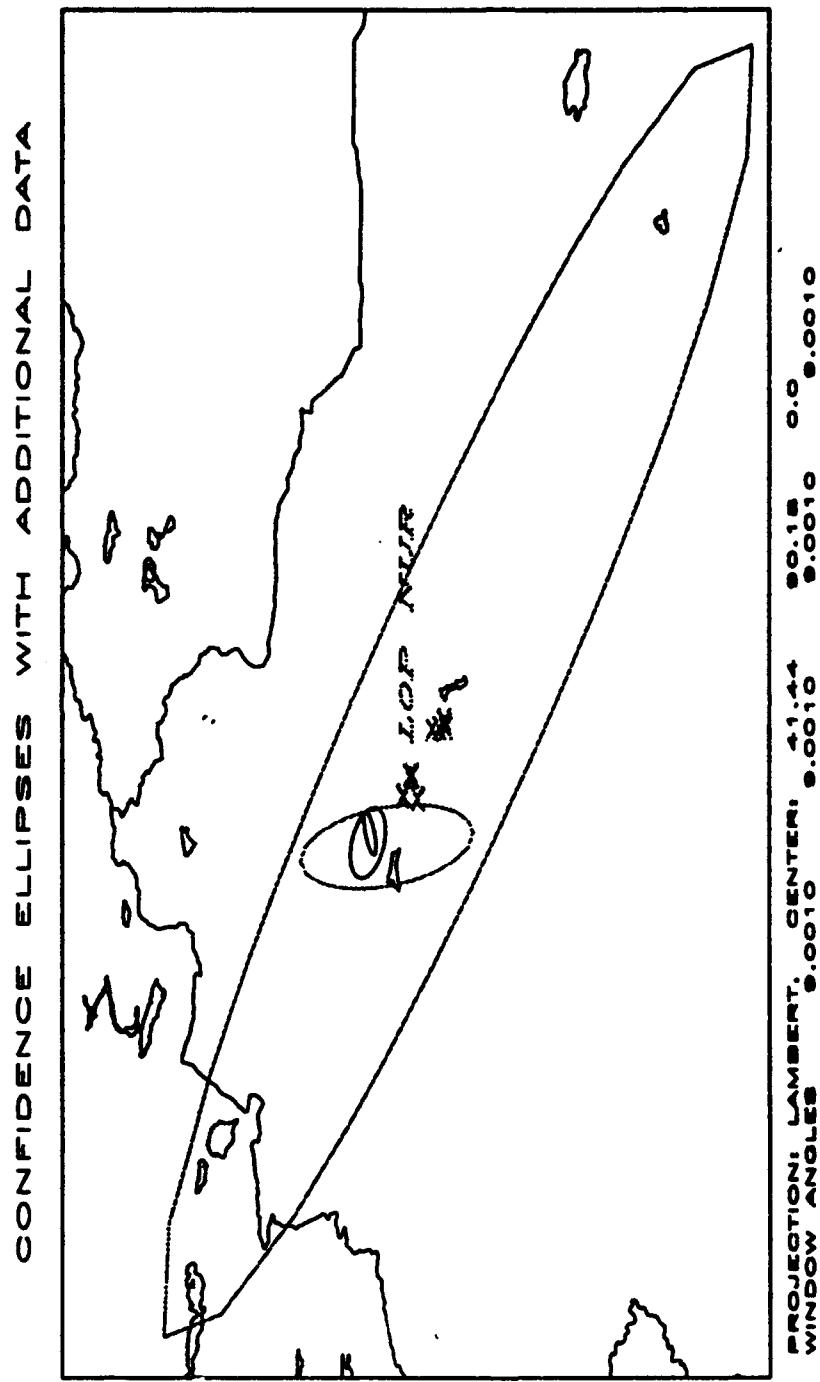
Figure 8: The figure illustrates the reduction in the 95% confidence ellipses for the epicenter of the event on April 14, 1993 as data are added to in order (1) YKA, (2) WMQ, (3) ASAR/WRA to the data

22
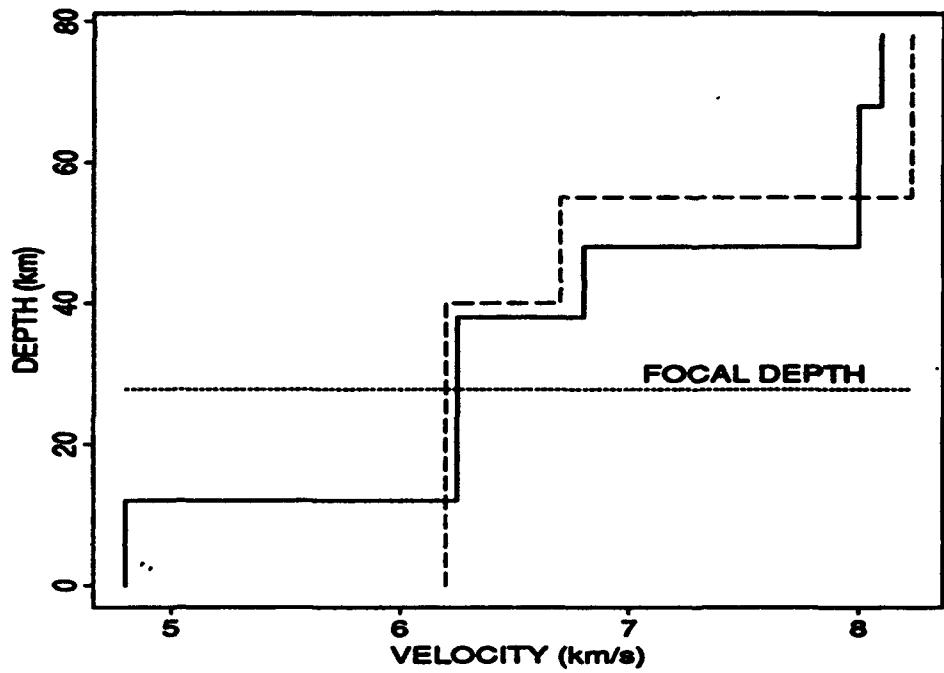
Figure 9: Comparisons of velocity models used by the location program LocSAT and estimated by Barker (1992) for a profile SSE of the station WMQ.

Epicenter

We compare the estimated epicenter and associated uncertainty with the locations of the Lop Nur nuclear weapons test base and neighboring seismic zones.

JED of Lop Nur explosions

From the map in Figure 8 it is clear that the confidence ellipse of location for the 93/04/14 is well outside the area spanned by the epicenters of previous nuclear explosions at the Lop Nur base, which covers an area of more than $100,000$ km^2. The explosion epicenters in Figure 8 were obtained with the JED method (Marshall and Jones, private communication, 1993).The map in Figure 10 zooms in on the explosion epicenters showing that the atmospheric and underground tests are separated with almost 100 km. The underground tests group in three areas separated by about 40 km. The explosions of the most eastern area (6 events) are compared in Figure 10 with the locations of two explosions (denoted Yongtai in the Figure 10), both supposed to have occurred prior to 1987 as described by Matzko (1992) citing a Chinese publication. The JED of the events in Figure 10 were constrained to the epicenter of event 87/06/05 marked in Figure 10. From this it appears that the events dated 84/10/03 and 83/10/06 in Figure 10 could well correspond to the ones specified by the Chinese, as they are offset only a few km. Therefore, even if the uncertainties of the JED solutions are not available, the solutions appear to accurate at least to within a few km.

Seismicity and Faults in Eastern Tien Shan

The Lop Nur test base in near the Tien Shan mountain range, which is a seismically active. Important thrust faulting occurs in the north eastern Tien Shan (Tapponier and Molnar, 1979). Mechanisms for large earthquakes near Urumchi - where the station WMQ is located - show that faulting consistent with a P axis roughly perpendicular to the recent E-W fold trends. The maps in Figure 11 and 12 show the geographical distribution of the seismicity since 1970 as reported by USGS for an area $+-3^o$ and $+-6^o$ in latitude and longitude from the center of the Lop Nur test base. Major active faults are also overlain in Figure 11 (after Tapponier and Molnar, 1979). The magnitude distribution of the events in Figure 13 shows that, in average, there were since 1970 a few events/year larger than mb=4.5. Large historical earthquakes have also been reported for this part of the Tien Shan mountains.

For comparison the confidence ellipse of the 93/04/14 event is also marked together with the earthquakes located by NEIS in Figure 11 and is covers a major fault. Most of the NEIS locations do, however, not line up along the major faults marked in Figure 11. As the standard errors of the NEIS epicenter determinations are comparable to those obtained for the 93/04/14 here the symbol sizes in Figure 11, which are proportional to event magnitude, should be much larger to reflect location uncertainty. It therefore appears that the epicenter estimate of the 93/04/14 is entirely consistent with the prevailing seismic activity in the Eastern Tien Shan.

24

JED OF LOP NUR EXPLOSIONS
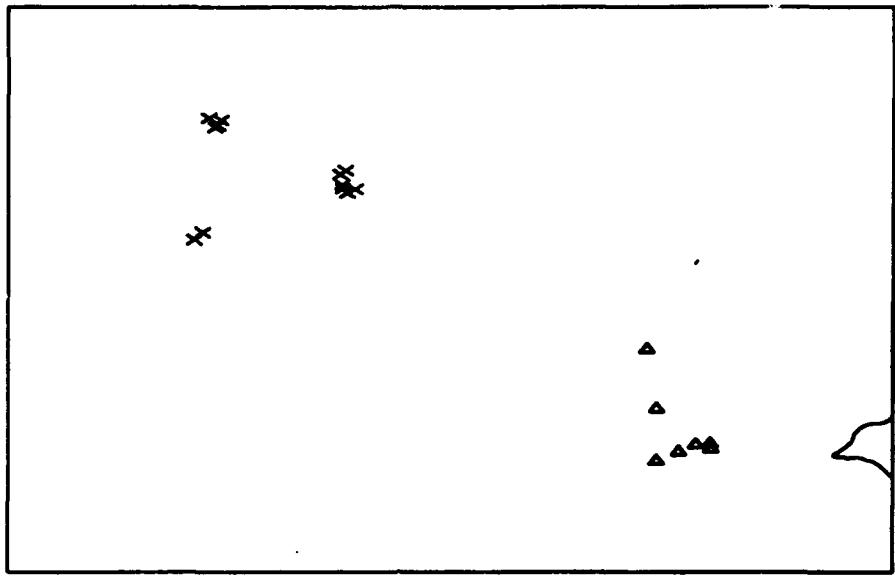
PROJECTION: LAMBERT.   CENTER: 41.23   89.02   0.0
WINDOW ANGLES   0.9010   0.9010   0.9010   0.9010

CONSTRAINING OF JED LOP NUR EXPLOSIONS
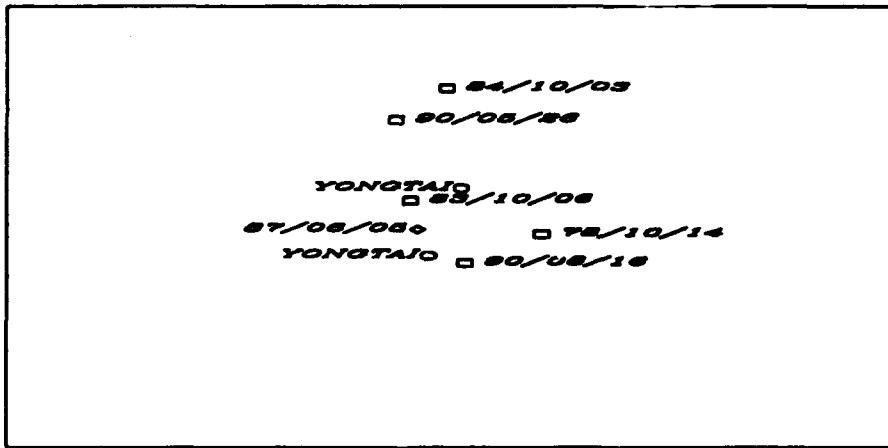
PROJECTION: LAMBERT.   CENTER: 41.88   89.73   0.0
WINDOW ANGLES   0.9800   0.9800   0.9800   0.9800

Figure 10:   (a) distribution of explosion epicenters at the Lop Nor test base, under-
ground and atmospheric tests are indicated with crosses and triangles
respectively; (b) relative location of events used to constrain the JED of the
explosions.

EARTHQUAKES AND FAULTS

PROJECTION: LAMBERT,   CENTER: 42.25   87.00   0.0
WINDOW ANGLES   2.7010   2.7010   2.7010   2.7010

Figure 11:   The epicentral distribution of the seismicity since 1970 as reported by
             USGS in the Lop Nor and neighboring areas. Major active faults are
             defined by Tapponier and Molnar (1979) are also indicated together with
             the 95% confidence ellipse of the event on April 14, 1993.
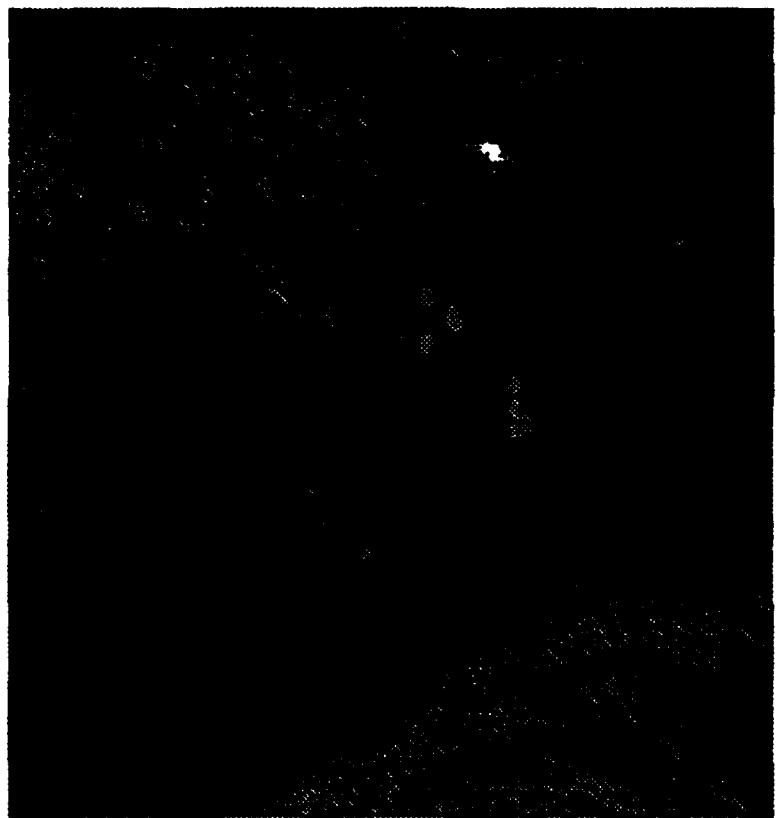
Figure 12: The epicentral distribution of the seismicity since 1970 as reported by USGS in the Lop Nor and neighboring areas plotted on a topographical map (Fielding, personal communication, 1993) and

DISTRIBUTION OF mb FOR EARTHQUAKES AROUND LOP NUF
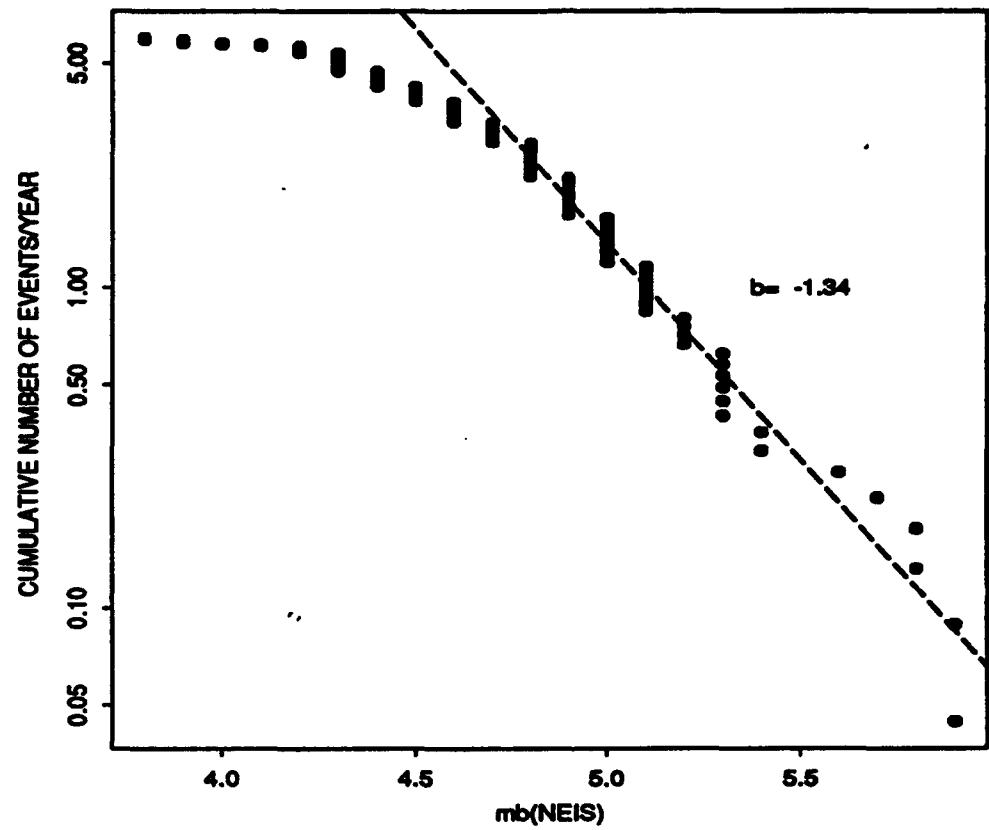
Figure 13: The magnitude, mb(USGS), distribution of earthquakes reported by USGS since 1970 in the Lop Nor and neighboring areas.

The map in Figure 12 provided by Fielding (private communication, 1993) shows that the location of the 93/04/14 is in quite a mountainous part of the Tien Shan.

Interestingly, some of the previous earthquake epicenters fall inside or very close to the Lop Nur test base (see Table 3).

Table 3: Earthquakes near Lop Nur Test Base

Date	Time	Lat(N)	Lon(E)	Depth	mb
76/03/20	04:34:00	41.7640	88.6700	8	5.00
87/12/22	00:16:39	41.3600	89.6380	21	5.90
88/11/15	16:56:46	42.0180	89.2950	33	5.00
90/01/21	07:53:32	41.5340	88.7280	33	4.60

Focal Depth

It is well known that an accurate determination of focal depth by itself can positively identify a seismic event. The secondary phases at the ASAR and WRA and the IMS arrays fit expected arrival times of pP and sP respectively which constrain the focal depth to between 25-30 km, which is compatible with the P and S arrival times at WMQ and first arrival times at all.stations. Furthermore the similarity of the f-k spectra for primary and secondary phases at the arrays lends support to this interpretation of the secondary phases at the arrays as depth phases. The estimated depth, 27 +- 2 km, is close to the average depth of earthquakes in eastern Tien Shan (see Figure 14). Omitting depth phases the estimated depth became 21 +-20 km and the standard deviations of the residuals is similar to that of the residuals for the depth constrained by the depth phases.

Characteristics of recorded waveforms

In order to compare the waveforms recorded for the 93/04/14 with previous events the data base at CSS and the IRIS/DMC were searched for events at or close to Lop Nur recorded by the IMS arrays and WMQ. Figure 13 shows the epicenter of the events which are summarized in Table 4 relative to the location of the 93/04/14 event.

Data at NRA0

Figure 15 compares waveforms at NRA0 (single sensor) for the 93/04/14 event with those of a presumed underground nuclear explosion (92/09/25) and three other earthquakes. The explosion record is on the whole simpler and has a higher frequency content that do the earthquake records and that of the 93/04/14 event, although these records also have clear high frequency components over riding the dominant low frequency amplitudes. The apparently reduced low frequency components of the explosion record agrees

29

DISTRIBUTION OF DEPTH FOR EARTHQUAKES AROUND LOP NUR
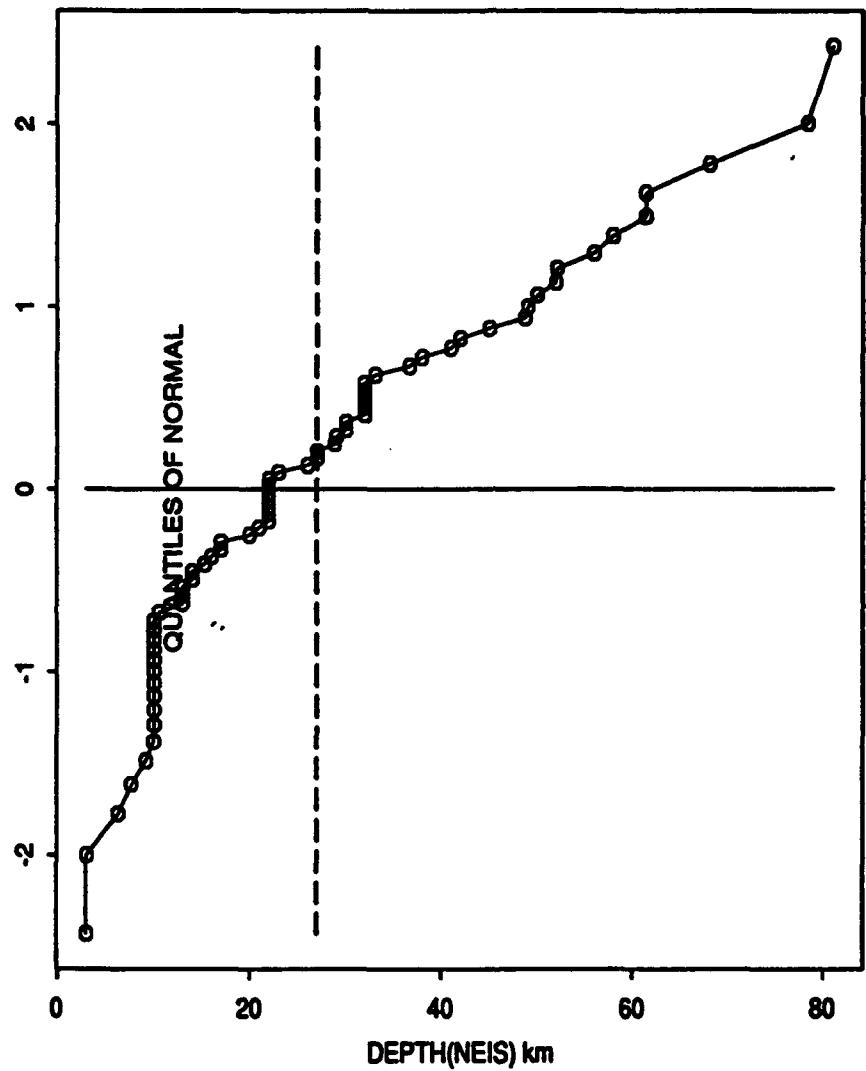
Figure 14:   The distribution of focal depths reported by USGS for earthquakes in
eastern Tien Shan.

91/09/17○

91/06/06○

92/11/27○

92/09/25
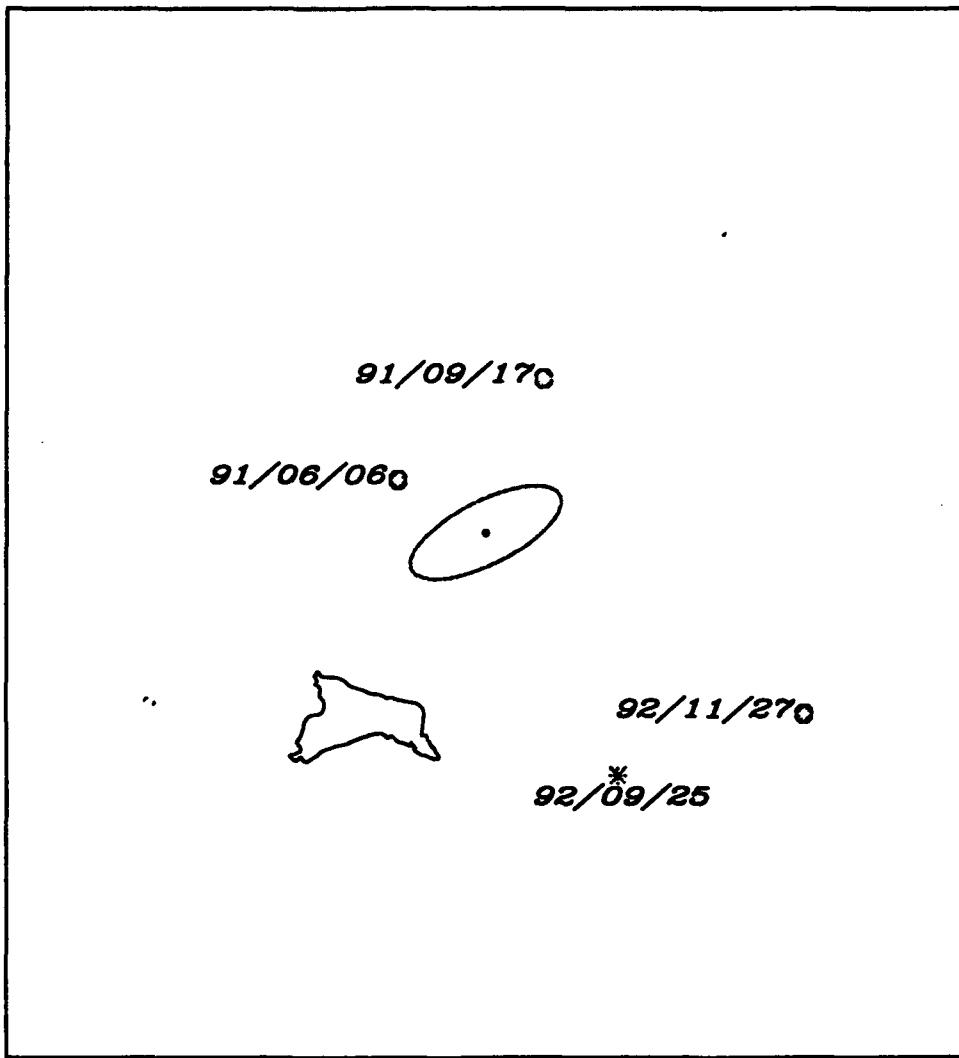
PROJECTION: LAMBERT,   CENTER: 42.61   87.67   0.0
WINDOW ANGLES   1.8010   1.8010   1.8010   1.8010

Figure 15:   Epicenters of some events at and near the Lop Nor test base recorded at
the IMS array NRA0.

Table 4: Earthquakes with data for waveform comparisons

Date	Time	Lat(N)	Lon(E)	Depth	mb
91/06/06	08:02:08	42.705	87.221	32	5.10
91/17/91	18:53:22	43.141	87.968	22	4.80
92/06/08	09:20:55	43.598	88.277	30	4.20
92/11/27	16:09:09	41.978	89.283	14	5.30

with the results of Taylor and Marshall (1991) and Tsvang et al. (1993). The lack of low frequency components of the explosion record and its relative simplicity are in quantitative agreement with the results of Arora and Basu (1984) who compared spectral and complexity parameters from recordings at the array GBA in India from earthquakes in Xinjiang and Lop Nur explosions.

The difference in frequency content is largest between the explosion record and the one for the earthquake closest to the explosion (within about 50 km). The waveform of the 93/04/14 event resembles the most that of the closest earthquake (91/06/06).

Data at WMQ

Recordings at WMQ could only be found for earthquakes in IRIS/DMC. The waveforms for two earthquakes are compared with those of the 93/04/14 event in Figure 16. The two earthquakes are at somewhat closer distances, but the associated waveforms appear quite similar but with regard to frequency content and relative P and S amplitudes. Indeed the S/P amplitude ratio for the 93/04/14 on the vertical component is somewhat larger than for the two earthquakes and has a high value typical of earthquakes in other regions.

Concluding Remarks

The analyzed here for the 93/04/14 event all point to an earthquake source, with regard to location, focal depth as well as recorded waveform characteristics.

The collected data also illustrate the value of high sensitive arrays for detection of small events. The availability of data at WMQ at a local distance from the epicenter illustrate the use of beta-stations, even if the nature of the source in this case perhaps could be established with sufficient confidence from only teleseismic data.

The value of identification of depth phases for constraining focal depth is well known and demonstrated in this case. The capability of arrays to estimate direction of approach of primary as well as secondary phases enhances the confidence in the identification of secondary phases as depth phases.

COMPARISON OF SHORT PERIOD WAVE FORMS
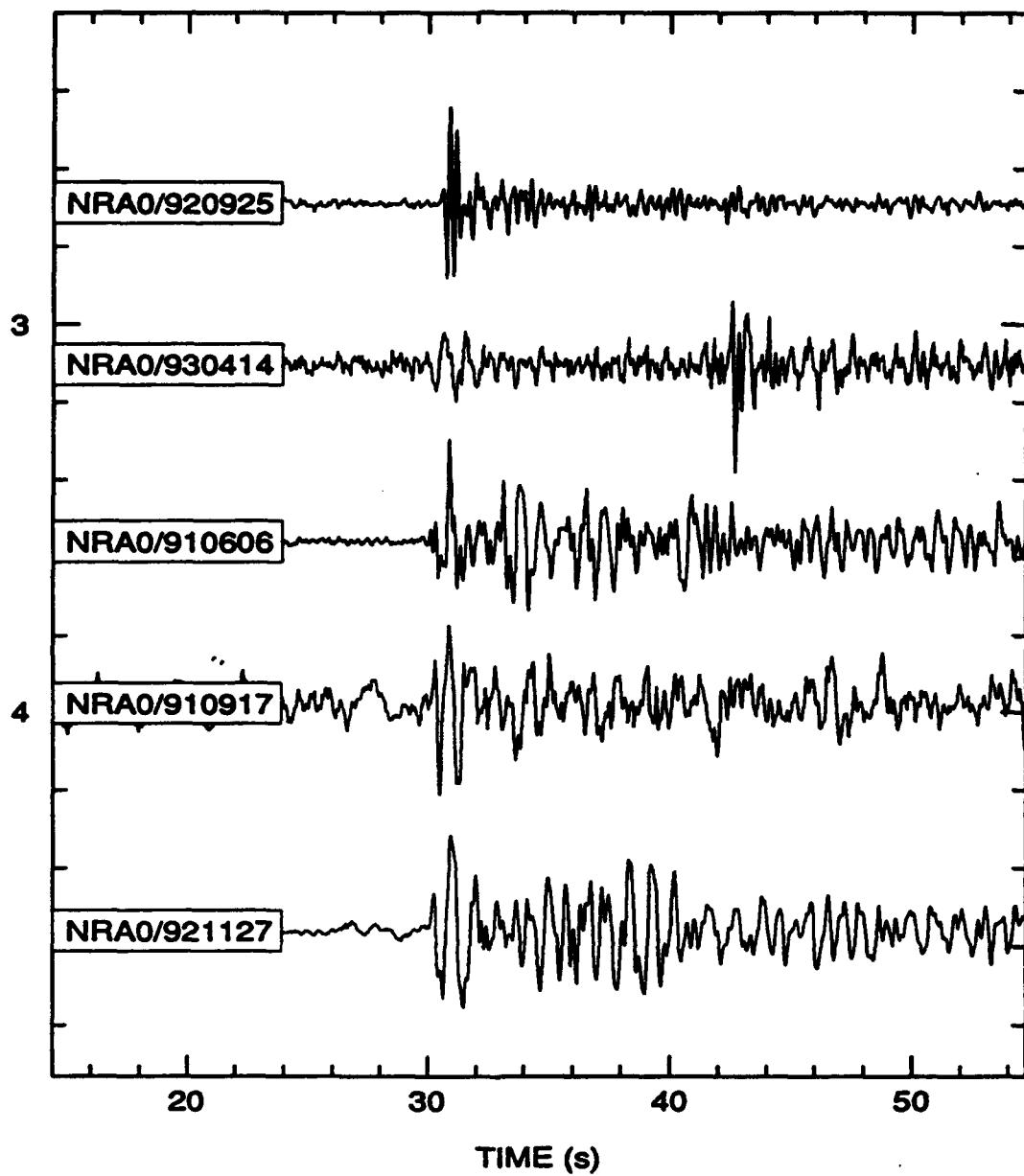
Figure 16:   Comparison of waveforms at NRA0 of events at and near the Lop Nor test base recorded at the IMS array NRA0.

The earthquakes with epicenter near the Lop Nur test base emphasizes the value of discrimination case studies for this area with closely spaced explosions and earthquakes.

Acknowledgements

References

Arora, S.K. and Basu, T.K. (1984) A source discrimination study of a Chines seismic event of May 4, 1983, Tectonophys, 109:241-251.

Barker, J.S. (1992) Analysis of regional body wave phases from earthquakes in Western China. 8-14.

Matzko, R., (1992) Geology of the Chinese Nuclear Test Site Near Lop Nor, Xinjiang, Province, China. 227-303

Tapponier, P. and P. Molnar (1979). Active faulting and Cenozoic tectonics of the Tien Shan, Mogolia, and Baykal Regions, J. Geopys. Res., 84: 3425-3459.

Taylor, S. R. and P. D. Marshall (1991). Spectral discrimination between Soviet explosions and earthquakes using short-period array data, Geophys. J.Int., 265-273.

Tsvang, S. L., Pinsky, V. I. and E. S. Husebye (1993). Enhanced seismic source discrimination using NORESS recordings from Eurasian events, Geophys. J. Int., 112:1-14.

Improvement of Regional Seismic Event Locations for Global Monitoring

Carl Romney, Vladislav Ryaboy

Summary

This paper investigates improvements in regional travel-time curves, and the identification of regional phases, that can be derived from long-range seismic refraction profiles, together with known mine blasts. Deep Seismic Sounding (DSS) observations within the Baltic shield were used to derive a new mean regional travel-time model for Pn-waves that extends to distances of 1,400 km. However, pronounced variations of Pn-wave propagation parameters were observed within this region, apparently caused by lateral structural inhomogeneities of the earth's crust and upper mantle. For example, Pn arrival times in southern Norway and Sweden at distances from 200 to 500 km are approximately 2-3 sec earlier than in southern Finland. Consequently, maps of Pn local travel-time corrections with respect to the new mean regional Pn curve were compiled for the NORESS, ARCESS, and FINESA arrays. Comparison of the Intelligent Monitoring System (IMS) locations, using the standard IMS reference travel-time curves, with those determined using the new mean regional travel-time curves together with the local corrections, showed that relocated events could differ with the IMS locations by 20 km, and the difference in origin time was as large as ±1.5 sec. Simplifying assumptions in the IMS about the travel-times and velocity of Lg-waves at near-regional distances have led to distance-dependent location biases of 20 to 30 km for mine blasts at known locations. Using DSS data to help define the pattern of the observed waves in the northern Baltic region, we found that the assumed Lg waves were actually SmS (shear-wave reflection from the Moho), and applying the appropriate travel-time curve eliminates the distance component of this bias. Our analysis showed that large travel-time variations, of the order of 10 sec for Pn-waves, are observed in different regions of the world. We came to the conclusion that none of the existing standard global travel-time curves can consistently produce regional event location accuracies adequate to meet global nuclear test ban monitoring objectives. However, a composite Pn travel-time curve that we define for Precambrian shields appears to be transportable to other similar structural provinces of the world, which comprise much of the continental area. We propose that this curve be applied in such provinces for monitoring purposes. Tectonically active regions will probably require individual, region-by-region calibration.

Introduction

The effectiveness of a seismic network in a comprehensive nuclear test ban monitoring role may be critically dependent on the accuracy with which it is able to locate seismic events. Geophysical and other techniques designed to pinpoint the cavity from a concealed underground explosion, or to obtain proof of its nuclear origin, have been found to be ineffective when applied to searching regions of the size of normal seismic epicentral uncertainty areas (Romney, 1990). For seismic locations using just a few stations, as will be the case for numerous low magnitude events near the network's detection threshold, highly accurate regional travel-time tables, phase timing, and azimuth estimation, as well as the correct identification of phases, are all crucial in approaching the desired accuracies. The objective of this paper is to show that improved location capability can result from the application of propagation parameters of major regional phases derived mainly from deep seismic sounding (DSS) profiles within the Baltic shield and neighboring areas. We will use data from the Intelligent Monitoring System (IMS) [Bache et al., 1990] and its associated regional seismic stations in Scandinavia to model a monitoring network and to demonstrate that improvements will result from incorporating region-specific propagation parameters.

Event locations in general have two sources of error, random and systematic. One source of random errors is measurement error, which is usually a function of signal-to-noise ratio(SNR). Systematic errors, however, are caused by misidentification of phases, inaccurate travel-time tables, and biased azimuth estimates [Bratt and Bache, 1988; Mykkeltveit et al., 1990]. The most direct application of DSS observations and mine blasts with well determined locations as a tool for improving event locations is to reduce the systematic errors due to inaccurate travel-time tables, as well as to the misidentification of regional phases. Both of these applications will be investigated in this paper.

Travel-time tables used for locating local and regional seismic events are generally based on one-dimensional velocity models. For the IMS, this model consists of two crustal and two upper mantle plane homogeneous layers [Bache et al., 1990; Bratt et al., 1990]. The crustal thickness for this model is 40 km, and the Moho depth and the layer velocities are an average fit to the region under consideration. There are, however, large deviations from this model within the Baltic shield. According to detailed DSS observations, the Moho depth varies from approximately 30 km in southern Norway and southern Sweden to about 55 km and greater in southern Finland and some other areas [Luosto, 1991; Sharov, 1991; Ryaboy, 1990; Kinck et al., 1990; BABEL, 1993a, 1993b]. The crustal thickening is mainly due to a layer with a P-wave velocity of 7.0-7.4 km/sec in the lower crust [Korhonen et al., 1990; Kinck et al., 1990]. Travel-time tables used for locating events usually do not take into consideration such regionally variable velocity structures. The result is location bias in areas where the structure departs from the regional mean.

Misidentification of phases can have an even larger effect. Variations of regional phase travel-times and amplitudes make phase identification a difficult task, especially where information on apparent surface velocity is limited or subject to uncertainty as in the case of small arrays, or not available at all as in the case of single stations. Because DSS data are observed from controlled sources and sampled at numerous fairly regular distance intervals, and on reversed and overlapping profiles, the entire wave pattern of initial and secondary arrivals becomes visible and regional phases can be identified more reliably.

In what follows, data from DSS profiles in the Baltic shield are applied to these two problems: namely, defining regionally and locally corrected travel time curves, and improving phase identification. While this work is primarily focused on Scandinavia and the study of IMS data, the methodology can also be applied to data from other regional seismic networks. In later sections of this paper we describe some ideas on extending this methodology to global monitoring.

DSS Observations

Scandinavia and northwestern Russia have been covered with a dense network of DSS profile observations crossing this region in different directions (Figure 17). The results of these studies have been published in numerous papers, monographs, and dissertations [e.g. Proceedings..., 1971, 1990; EUGENO-S..., 1988; Guggisberg, 1986; Stangl, 1990; Study of the deep structure..., 1986; Ryaboy, 1989; Structure..., 1991; Imaging and..., 1991; Luosto et al., 1984, 1989, 1990; Korhonen et al., 1990]. The lengths of the DSS profiles vary from 200 to 2000 km, and they provide observations of different kinds of P- and S- waves travelling in the earth's crust and upper mantle. Field observations were usually carried out along reversed and overlapping lines for dip control and continuity. Seismic signals were typically recorded in the frequency band from 1-2 Hz up to 20-25 Hz by vertical and, recently, horizontal seismometers.

We collected and analyzed the available DSS P-wave record sections and published travel-time observations, as well as data from recordings of chemical explosions with well known locations and origin times for the Baltic shield [Dahlman, 1967; Porkka et al., 1972; Sellevoll and Pomeroy, 1968; Bath, 1981; Cassell et al., 1983]. A number of shots detonated during the 1979 FENNOLORA DSS project from nine major shot points were recorded by the NORSAR array at regional distances [Mereu et al., 1983]. Record sections were constructed for all of the shot points using filtered beams at each of the seven NORSAR sub-arrays. The higher coherency within the subarrays improved the SNR for these beams relative to beams constructed as stacks of all NORSAR sensors [Ryaboy, 1990].

NORESS recordings of shots detonated along the POLAR DSS profile in northern Norway and Finland south of ARCESS [Luosto et al., 1989] were also analyzed. They had poor SNR, and beams constructed for different explosions did not show marked improvement in SNR. The SNR was improved to the point where the Pn-wave could be identified only after stacking beams for several explosions detonated at the same shot point.

Pn waveforms observed in this region usually have a complicated structure at distances greater than 300 km. This is observed most clearly when conducting detailed observations along reversed and overlapping lines. The emergence of Pn as the first arrival is marked by an increase in apparent velocity from 6.0-7.0 km/sec (for the Pg and Pb waves) to 7.5-8.0 km/sec or higher. Travel-time curves of Pn first arrivals are not linear, and there is a tendency toward a rise in the apparent velocities with increasing distance to 8.5-9.0 km/sec at ranges of 1,000 to 1,500 km. Strong arrivals with high apparent surface velocities are often detected as later phases in the P wave group. The interval over which they can be correlated fluctuates from tens to hundreds of km. Large later arrivals, as a rule, are characterized by lower frequencies and at distances less than the Pg/Pn crossover point, by higher apparent surface velocities than the low-amplitude waves recorded as first arrivals.
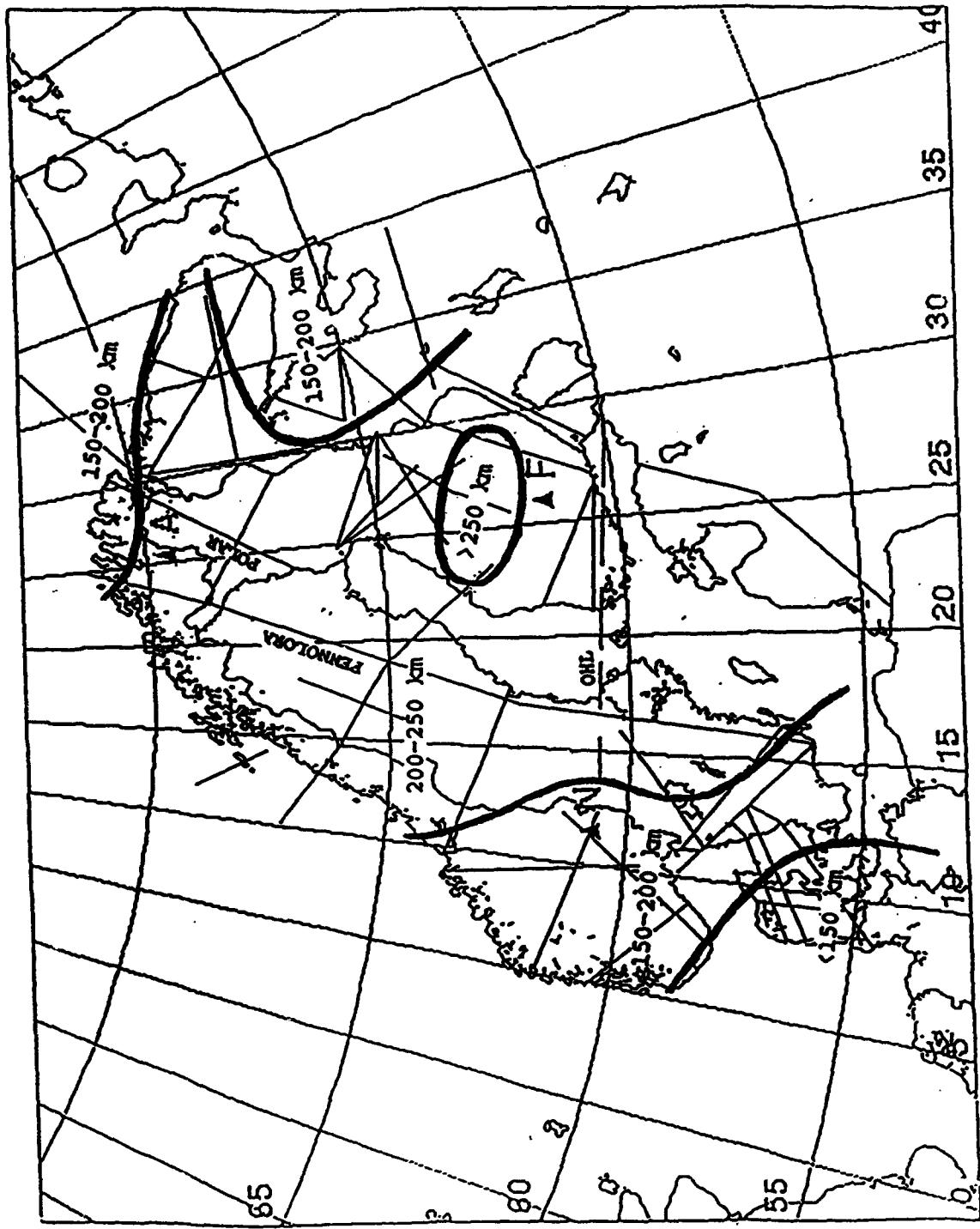
Figure 17: A map of DSS profiles (thin lines) and NORES (N), FINESA (F), and ARCESS (A) regional array locations. Thick lines and numbers bound regions of different Pg/Pn cross-over distance. FENNOLORA and POLAR are long-range DSS profiles. OHL is the Oslo-Helsinki-Leningrad profile.

38

In the record sections constructed for the FENNOLORA and OHL profiles [Guggisberg, 1986; Ryaboy, 1990; Hauser and Stangl, 1990], a shift of 1.5 - 2.5 sec was observed in the travel-time curve between 800-900 km, with the first arrival decaying rapidly and a later phase appearing as the first arrival. Beyond 900 km, the apparent surface velocity of the first arrivals sharply increased to 8.6-8.8 km/sec accompanied by a decrease in frequency (Figure 18). This feature of the *Pn* record sections is typical for the Baltic shield and is most likely caused by a low velocity layer in the upper mantle at depths greater than 100 km [Hauser and Stangl, 1990; Ryaboy, 1990]. Attenuation of *Pn* first arrivals and smaller offsets were also observed at distances less than 800 km for several DSS profiles within Scandinavia [Lund, 1979; Proceedings..., 1990]. Local small-scale inhomogeneities and thin low-velocity layers in the upper mantle are the suspected cause of these variations.

Pn propagation parameters such as travel-time, cross-over distance with *Pg*, amplitudes, frequencies, and polarization characteristics are variable within this region. For example, we compare two DSS profiles: a North Sea - southern Norway profile [Cassell *et al.*, 1983] and the SVEKA profile [Luosto *et al.*, 1984]. The latter was observed in southern areas of Finland and the former in southern Norway from land recordings of offshore explosions. The waveforms beyond 450 km for the northern end of the North Sea - southern Norway profile were recorded at the NORSAR array.

There are important differences between seismic wave propagation parameters for these two profiles (Figure 19). *Pn* travel-times in southern Norway are, for the same distances, more than 3 sec early in comparison with those in southern Finland. The *Pg* / *Pn* cross-over point is located at a distance of 150 km in southern Norway, and 270 km in southern Finland. The first arrivals on the record section for the SVEKA profile from 200 to 270 km are lower crustal refracted waves with apparent velocities of 7.35 km/sec. Arrivals with similar apparent velocities were not recorded in southern Norway. The map in Figure 17 includes an overlay of *Pg* / *Pn* cross-over distances constructed from DSS profile observations. This distance varies within the Baltic shield from 130 to 270 km.

Defining the Mean Regional Scandinavian (MRS) *Pn* Travel-Time Curve

The available *Pn*-wave record sections and travel-time curves constructed for DSS profiles described above were collected to correlate and measure travel-times of *Pn* first arrivals. Observations for the FENNOLORA DSS profile extended to a distance of 2000 km, but first arrivals could be reliably picked only up to distances of 1300-1400 km because of poor SNR.

Travel-time measurements were made from the *Pn* record sections (measured at 10 km spacing) and published *Pn* travel-times were also used. These data were applied to produce the composite *Pn* travel-time plot shown in Figure 20. This figure is based on analysis of approximately 10,000 km of DSS profiles and includes 1420 measurements. The observations have a scatter ranging up to about three seconds for a fixed distance. This scatter is much larger than the observational error and thus, is likely caused by factors such as lateral structural variations of the earth's crust and upper mantle. Also evident in the data is a discontinuity near 850 km, indicative of a low-velocity zone.
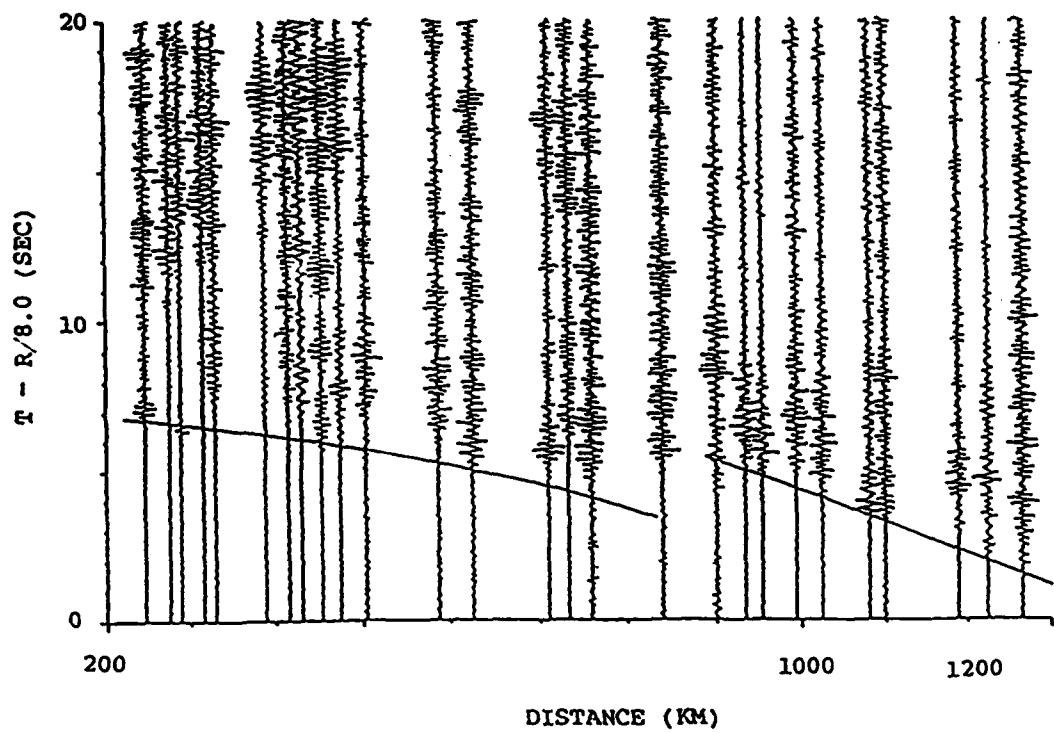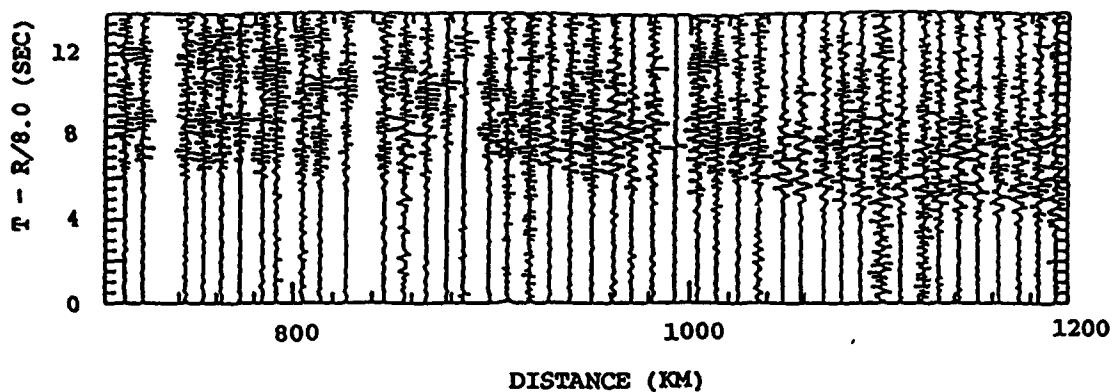
Figure 18: *Pn*-wave record sections for northern (top) and southern (bottom) areas of the Baltic shield. The northern record section was constructed for shot point I of the FENNOLORA DSS profile (adapted from Hauser and Stangl, 1990). The southern record section is from the Oslo-Helsinki-Leningrad (OHL) profile overlain by theoretical travel-time curves of waves refracted in two upper mantle layers separated by a low velocity zone (adapted from Ryaboy, 1990). Note the delayed travel-time branch beyond 850-900 km, followed by an increased apparent velocity.

40
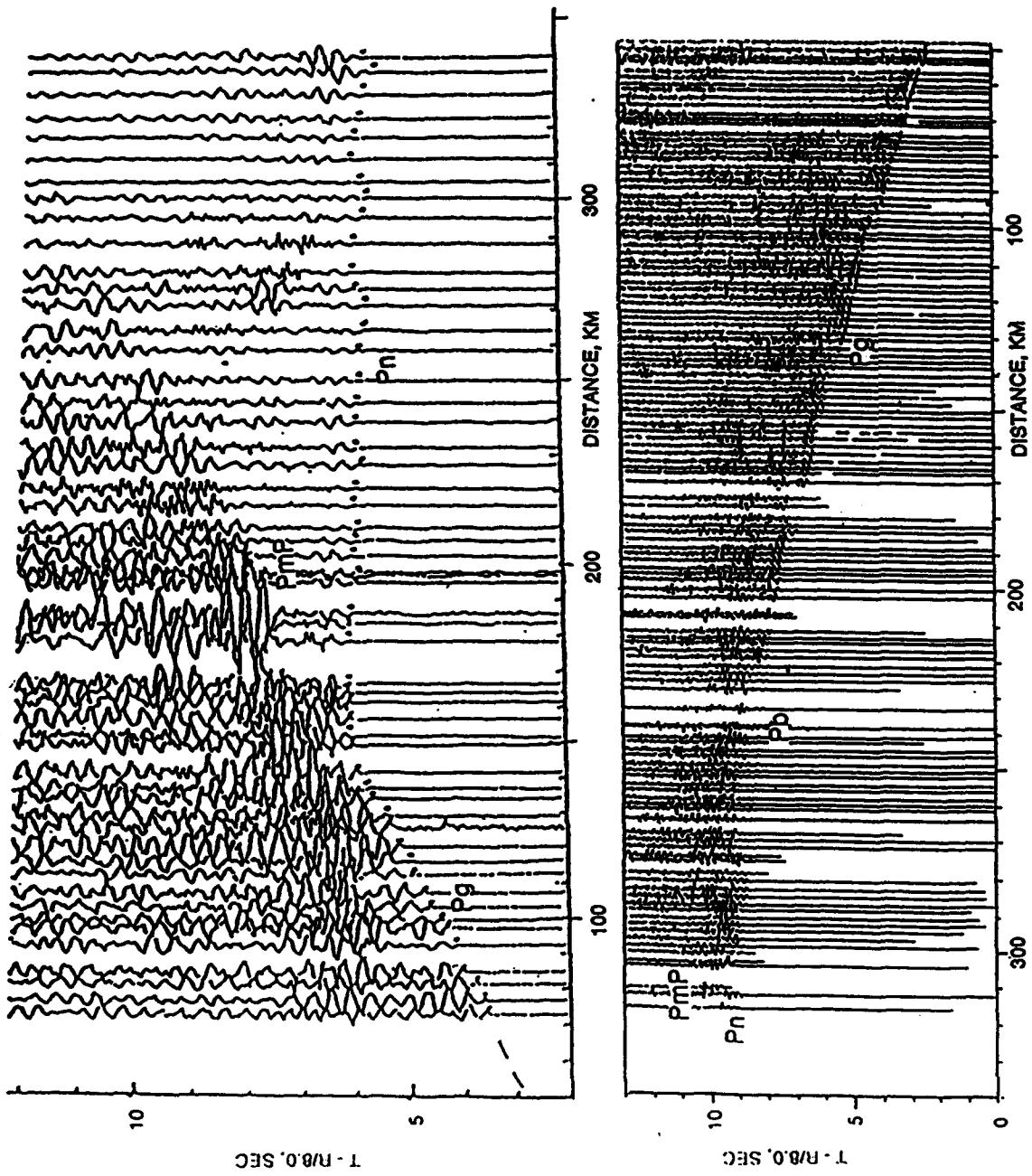
Figure 19: Comparison of P-wave record sections from the North Sea-southern Norway profile (top) with the SVEKA profile in southern Finland (bottom). DSS profiles are adapted from Cassell *et al.*, (1983); and Luosto *et al.*, (1984), respectively. Note the significant differences in the reduced travel-times of *Pn* (about 5.5 - 6.0 sec in southern Finland), and about 8.5 - 9.0 sec in southern Norway), and in the distance to the *Pg/Pn* cross-over points (about 150 km in southern Norway, and 270 km in southern Finland).

41
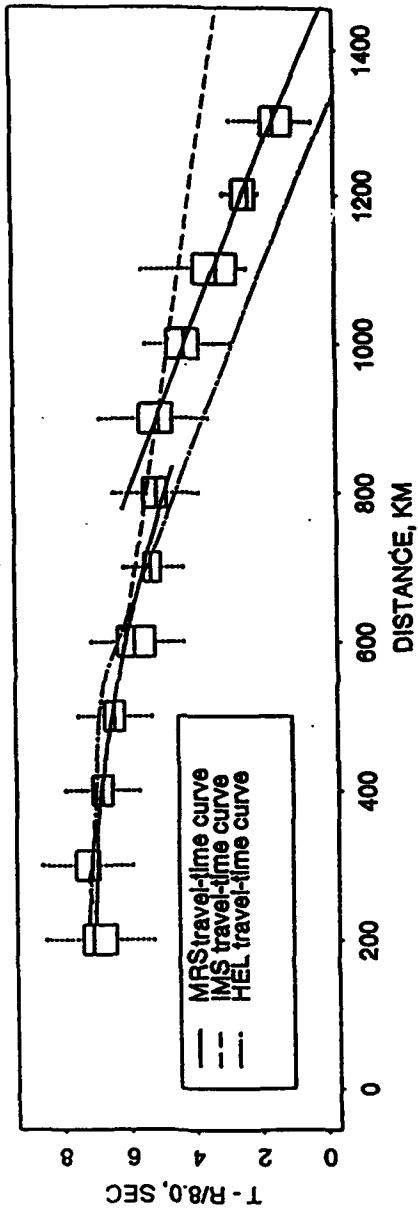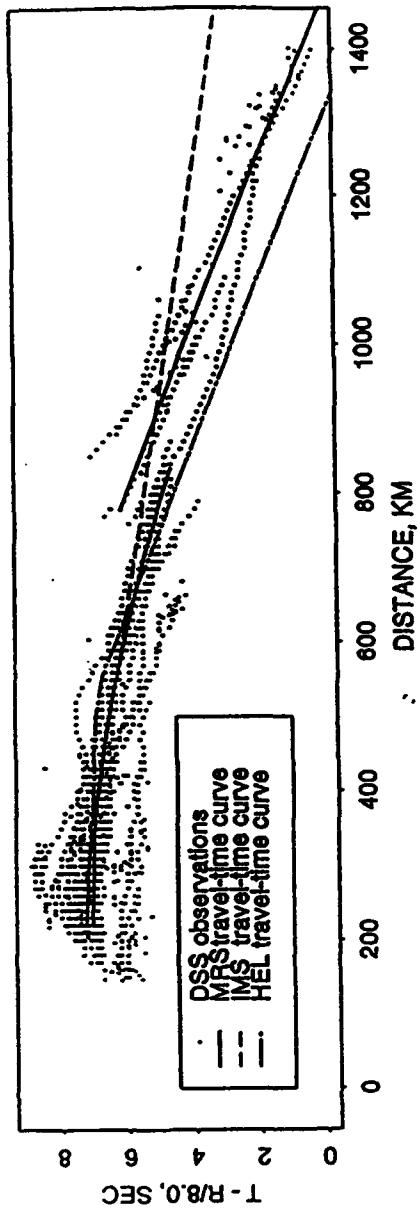
Figure 20: Top: comparison of *Pn* travel-time observations for the Baltic Shield measured from explosions with controlled sources (dots), with *Pn* travel-time curves used for event locations in the IMS and Helsinki (HEL) seismological bulletins. Note that neither the IMS nor the HEL curves are a good fit to the observed DSS data beyond about 600 km. Bottom: box plots of *Pn* travel-times (dots) shown in Figure 20 (top). Boxes were calculated for 100 km distance windows. The horizontal line in the interior of each box is located at the median of the data. The top and bottom of each box represent the second and third quartiles of the data. The dotted vertical lines extend through the first and fourth quartiles to the extreme values of the data. The solid line labeled MRS is the proposed new mean regional Scandinavian reference *Pn* travel-time curve.

42

Three travel-time curves are superimposed on the observed DSS travel-time data shown in the upper section of Figure 20. Two of these, IMS and HEL, are the curves used to locate events for the IMS and Helsinki bulletins, respectively. Both of these Pn travel-time curves are fairly good fits to the DSS data for distances less than 500-600 km. However, beyond about 600 km, DSS observations are generally early with respect to the IMS Pn reference travel-time curve for the Baltic shield. On the other hand, DSS observations at these longer ranges are generally late with respect to the Pn travel-time curve currently in use to locate events for the Helsinki bulletin (HEL). The third travel-time curve on Figure 20, labeled MRS, represents our current best estimate of a generalized mean regional Scandinavian Pn travel time curve for the entire region [Ryaboy, 1993]. Local corrections to this curve will be discussed subsequently.

Our preferred model to fit the observed DSS Pn travel-times is based on a one-dimensional spherical earth model with two crustal layers and a low velocity zone in the upper mantle (Figure 21). The MRS travel time curve shown on Figure 4 is calculated from this model. Velocity models underlying the IMS and HEL travel-time curves are also shown on Figure 21. Our preferred model is, of course, not unique, and is only one representative of a family of velocity models consistent with the observed Pn travel-times. However, it does have the merit of providing a better fit to the DSS Pn observations than do the other two models, as shown by its excellent fit to the box plots on the lower section of Figure 20, representing the DSS observations grouped within 100 km distance windows.

Sub-Regional and Local Travel-Time Corrections

We interpret the observational deviations from the MRS curve (Figure 20), which have a standard deviation of ±0.65 sec, to be mainly the result of sub-regional structural and velocity inhomogeneities. It was earlier noted that the Pg/Pn crossover distance varied systematically over this region. This observation is, of course, a reflection of systematic travel time variations. In southern Norway and southern Sweden the Pn-wave is recorded 1.0-1.5 sec early, and in southern Finland 1.0-1.5 sec late, relative to our preferred Pn travel-time curve. The earliest Pn travel-times were observed within a narrow zone of the Oslo graben (50-100 km wide) south of the NORSAR / NORESS arrays. In the southern part of the FENNOLORA profile, at distances of 800-1000 km, the Pn-wave is recorded 1.5-2.0 sec earlier than in the northern part of the profile. This difference in Pn travel-times cannot be explained by variations of crustal structure along the profile, and probably indicates a zone of increased velocity in the lower lithosphere beneath southern Sweden. This zone was detected as a result of a joint interpretation of seismic and gravity observations for the Oslo-Helsinki-Leningrad profile [Ryaboy, 1990], and is supported by observations of teleseismic data [Husebye et al., 1986]. The fact that these variations appear to be systematic over subregions of significant size suggests that it is feasible to take them into account.

The method to be investigated here for estimating local travel-time corrections for improving automatic event locations takes advantage of the extensive work throughout the entire region of interest for determining the depth of the Moho. The residuals of the observed Pn travel-times with respect to the MRS curve (TT_{res}) are highly correlated with variations of the Moho depth (Figure 22) (coefficient of linear correlation of 0.86 and standard deviation of ±0.39 sec):
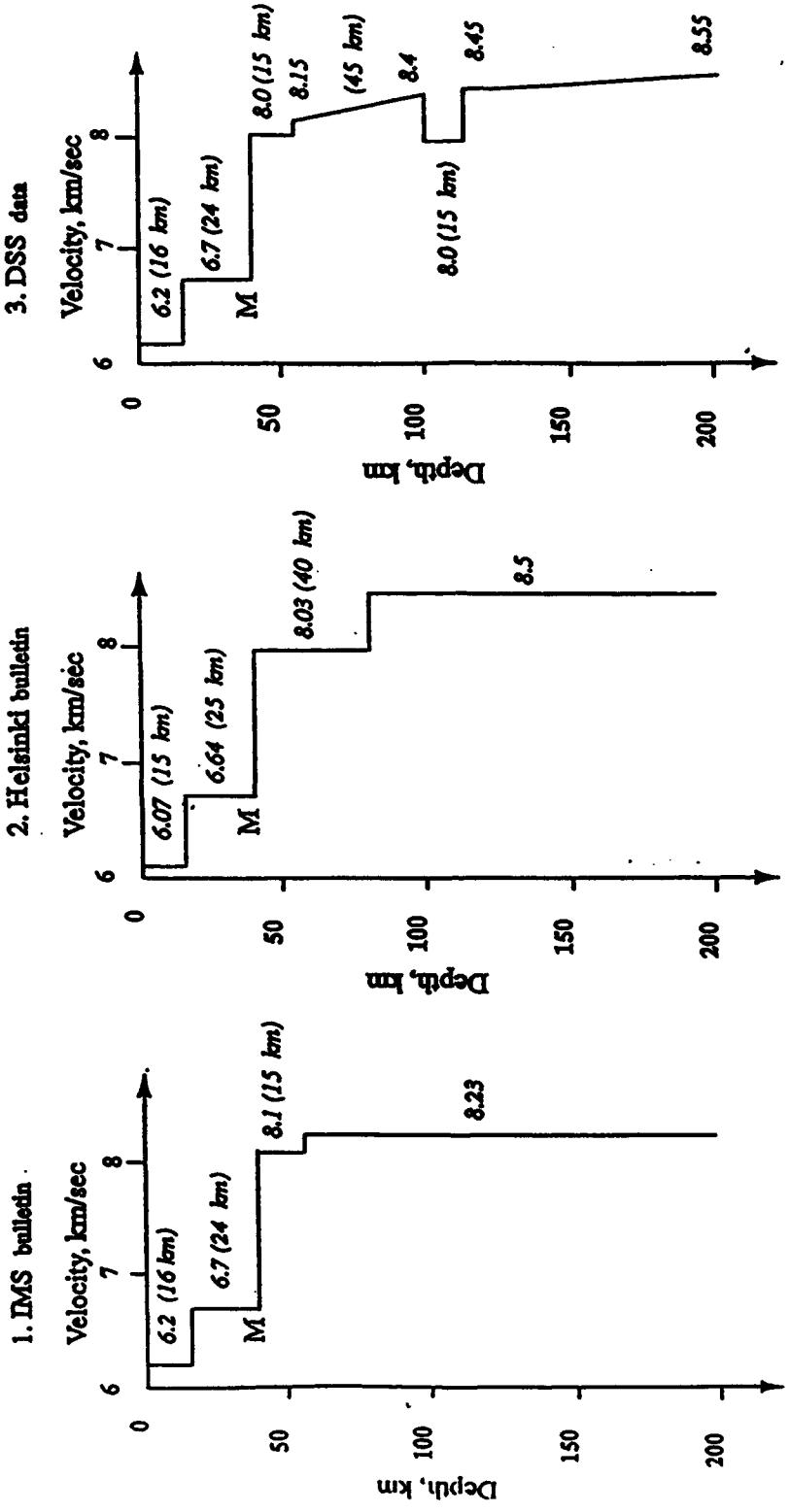
Figure 21: Reference velocity models of the earth crust and upper mantle for the Baltic shield. Numbers are *P*-wave velocities in km/sec, with layer thickness (km) in parentheses. The model on the right, based on DSS data, results in the MRS travel-time curve.

Figure 22: *Pn* travel-time residuals (with respect to the MRS curve) vs. the Moho depth for the Baltic shield. The residuals are highly correlated with variations of the Moho depth. This empirical relation and a Moho depth map were used to calculate ray-path dependent local corrections of *Pn* travel-times for regional event locations within the Baltic shield and neighboring areas.

45

$$TT_{res} = -4.802 + 0.058 * (M_{sp} + M_{rec}),\qquad (1)$$

where M_{sp} and M_{rec} are the Moho depths in km beneath shot point and receiver on the DSS profiles. This is an expected result, of course, since these identical DSS travel-times entered into the estimates of Moho depth. Values of TT_{res} were measured from the smoothed TT_{res} vs. distance curves constructed for different shot points on DSS profiles.

The empirical relation (1) and the Moho depth map were used to calculate, on a regularly spaced grid, the ray-path dependent local corrections mainly caused by lateral variations of the Moho depth. A Moho depth map for the Baltic shield and neighboring regions has been constructed based on the new and most reliable published data [BABEL, 1993a, 1993b; Kinck *et al.*, 1990; Korhonen et al., 1990; Luosto, 1991; Sharov, 1991; Structure and dynamics..., 1991; Study of the deep..., 1986]. The crustal thickness varies from approximately 30 km in southern Norway to 50-55 km and more in southern Finland and Sweden. The Moho map was digitized and included in a geophysical database at Cornell University [Fielding *et al.*, 1993]. This was then used to calculate the corrections to the mean regional travel-time curve throughout the region and for each station. As an example, Figure 23 shows the map of local corrections for the FINESA station. The maps for NORESS and ARCESS are similar, with differences caused by the crustal thickness variations beneath these stations. *Pn* local corrections for Scandinavia range within approximately ±1.5 sec.

However, an improvement in the *Pn* tables alone is not enough to give dramatic results for distances less than 800-1000 km within the Baltic shield. Based on our experience with automatic systems for regional event location, we have found that event mislocation, in some distance ranges, is as much a function of assumptions about regional phase identification as it is of regional errors in travel-time tables. In the following section of this paper, the problem of phase identifications for regional event locations is investigated.

Improved Phase Identification

A detailed study of ARCESS epicenters in the northern Baltic shield from mine blasts having known locations demonstrated bias in distance and in azimuth [Suteau-Henson, 1991; Suteau-Henson *et al.*, 1992]. We consider in this paper only the bias in distance. To study this phenomenon, we carefully analyzed selected ARCESS recordings of mine blasts from four known locations: Varanger (V), Saattopora (S), Kiruna (K), and Elijaervi (E) (Figure 24). Distances to the approximate centers of these mines from ARCESS are 156 km, 200 km, 287 km, and 421 km, respectively.
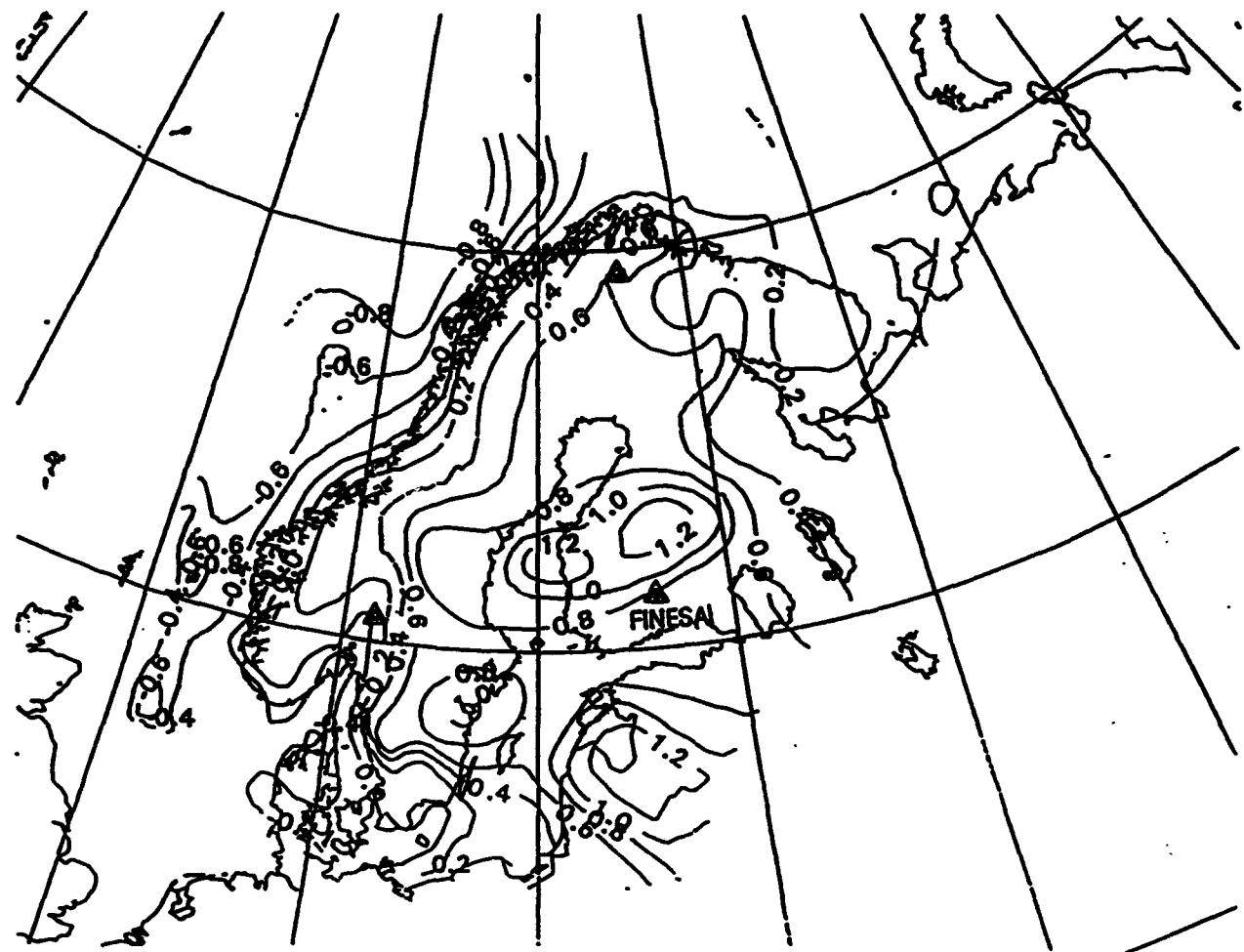
Figure 23:   Map of *Pn* local travel-time corrections for the FINESA array. Isolines represent the travel-time corrections in seconds. Triangles denote the NORESS (southern Norway), ARCESS (northern Norway), and FINESA (southern Finland) seismic stations.
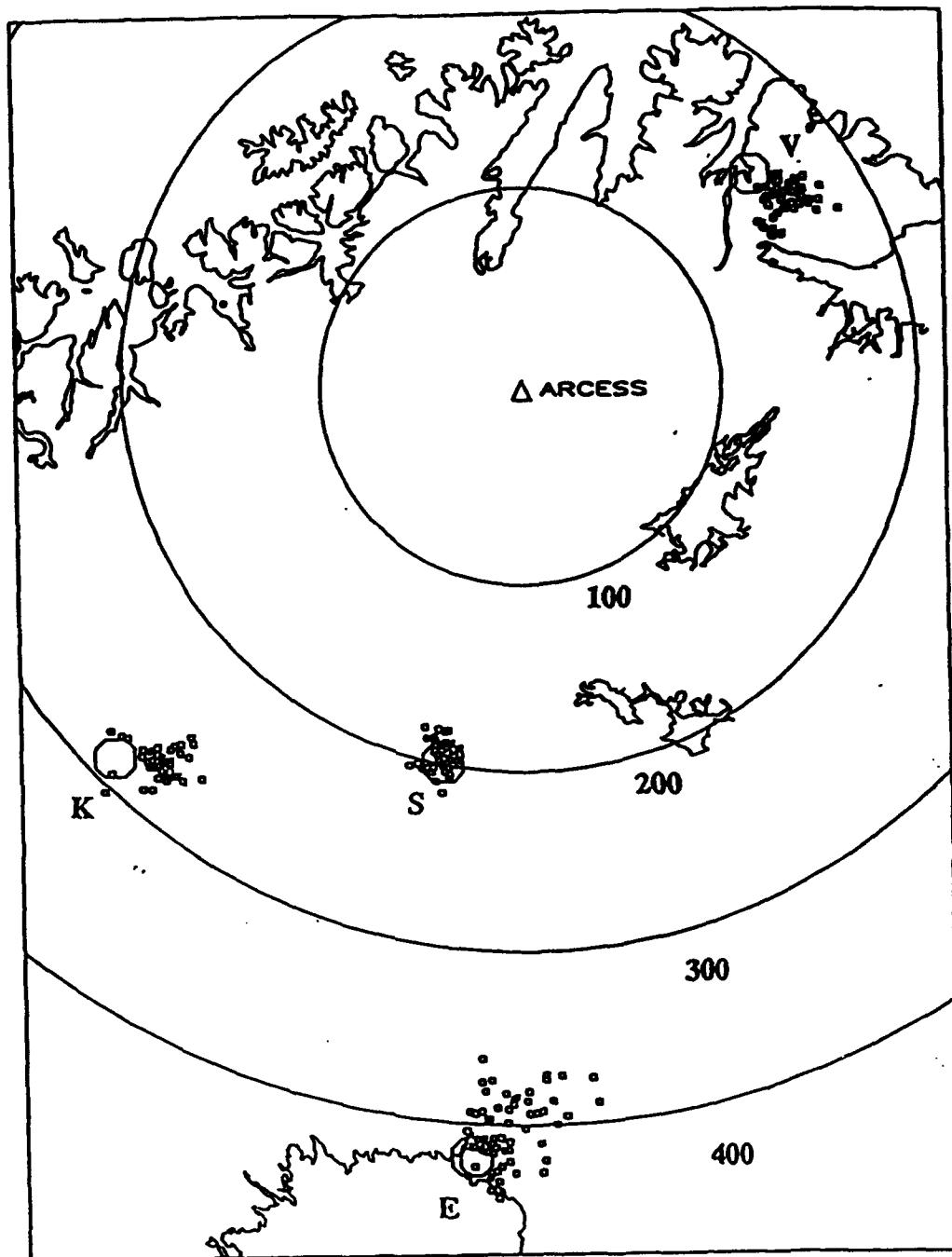
Figure 24: Location map of the ARCESS array (triangle) and seismic events (small squares) from mine blasts recorded within the northern Baltic shield and listed in the IMS bulletin. Large circles show distance from ARCESS at 100 km intervals. The Varanger, Saattopora, Kiruna, and Elijaervi mines, studied in this work, are designated by open circles and capital letters V, S, K, and E, respectively. Saattopora mine blast locations at 200 km do not have a bias in distance. Kiruna and Elijaervi mine blast locations at distances greater than 200 km are biased toward ARCESS, while Varanger locations at a lesser distance are biased away from ARCESS.

48

Comparing the mine locations to IMS epicenters, a distance-dependent trend in the average bias was noted, as shown in the following Table 5:

Table 5:

Mine	Mine Distance from ARCESS, in km	Average Epicentral Distance, in km	Bias, in km
Varanger	156	171	+·15
Saattopora	200	200	0
Kiruna	287	272	- 15
Elijaervi	421	391	- 30

The larger distance biases are much greater than would be expected from the variations caused by local or sub-regional perturbations in the travel-time curves, especially since DSS data in the regions of the mines show that Pn-wave travel-time variations are only approximately 0.5 second, comparable to the measurement error (Figure 23). Thus, the bias is likely the result of mis-timing or misidentification of phases. We turn to DSS observations in Scandinavia to help resolve this problem.

Detailed observations based on recordings of P- and S-waves were carried out in this area along the FENNOLORA [Guggisberg, 1986; Hauser and Stangl, 1990; Stangl, 1990] and POLAR [Luosto et al., 1989] long-range DSS profiles (Figure 17). As an example, Figure 25 shows the record sections of P- and S-waves for the POLAR DSS profile. Pg- and Sg-waves, refracted in the upper crustal layer, were observed as first arrivals within the P- and S-wave groups, respectively, up to a distance of 120-140 km. Pb- and Sb-waves, refracted in the lower crust, were usually observed as first arrivals up to that distance and continuing to about 200 km, where Pn and Sn emerge as first arrivals. High amplitude PmP and SmS reflected waves from the Moho were observed in the later arrivals of the P- and S-wave groups, respectively, at distances from approximately 100 to 350-400 km. Within this range the amplitudes of these reflected waves are typically much larger than the refracted first arrivals.

The observed travel-times of Pg, Pb, Pn, Sg, Sb, and Sn-waves recorded as first arrivals along the POLAR DSS profile, as well as the travel-times of the most intensive waves (PmP and SmS) recorded as late arrivals, are shown on Figure 26 and Figure 27. Also shown on these figures are the IMS reference travel-time curves for the first arrivals, along with curves for PmP and SmS-waves derived from the DSS observations. The observed P-wave arrival times from the POLAR profile fit, in general, the IMS reference travel-time curves for Pg, Pb and Pn-waves. However, Pg-waves were not recorded along the POLAR profile at distances beyond the cross-over point (Figure 25). Observed arrival times of Sg and Sb also fit the IMS travel-time curve for Lg. Sg was not recorded on the POLAR profile at distances greater than about 200 km nor was Lg. Sn-waves recorded along the POLAR profile fit the reference IMS curve between the cross-
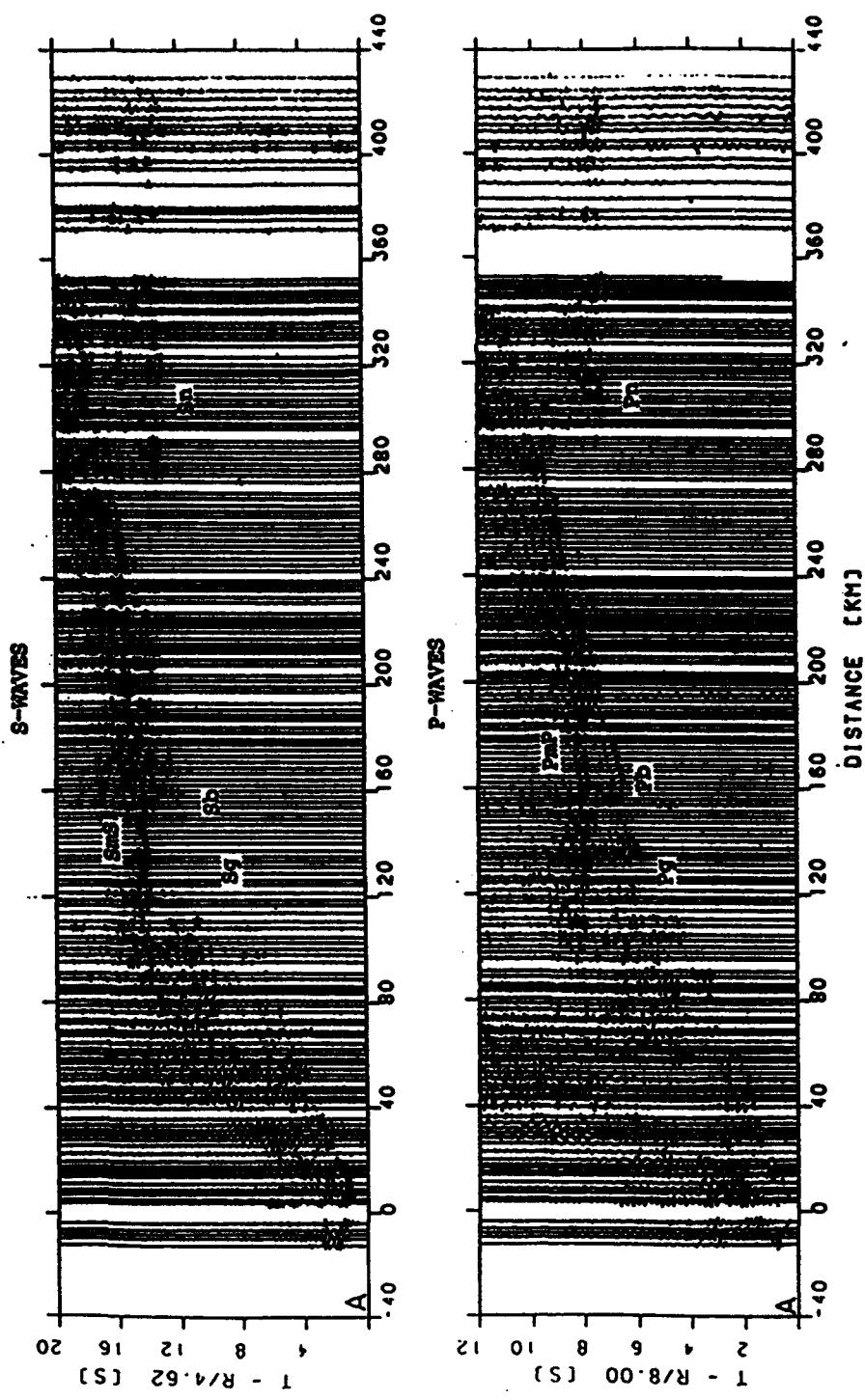
Figure 25: Trace-normalized record sections of S- (*top*) and P-waves (*bottom*) recorded on the POLAR DSS profile from shot point A (adapted from Luosto *et al.*, 1989). Band-pass filters of 2-6 Hz and 2-15 Hz were applied to the records of S- and P-waves, respectively. It may be seen that the most energetic arrivals between about 80 km and 280 km are PmP and SmS.

P-WAVE TRAVEL-TIMES FOR POLAR DSS PROFILE
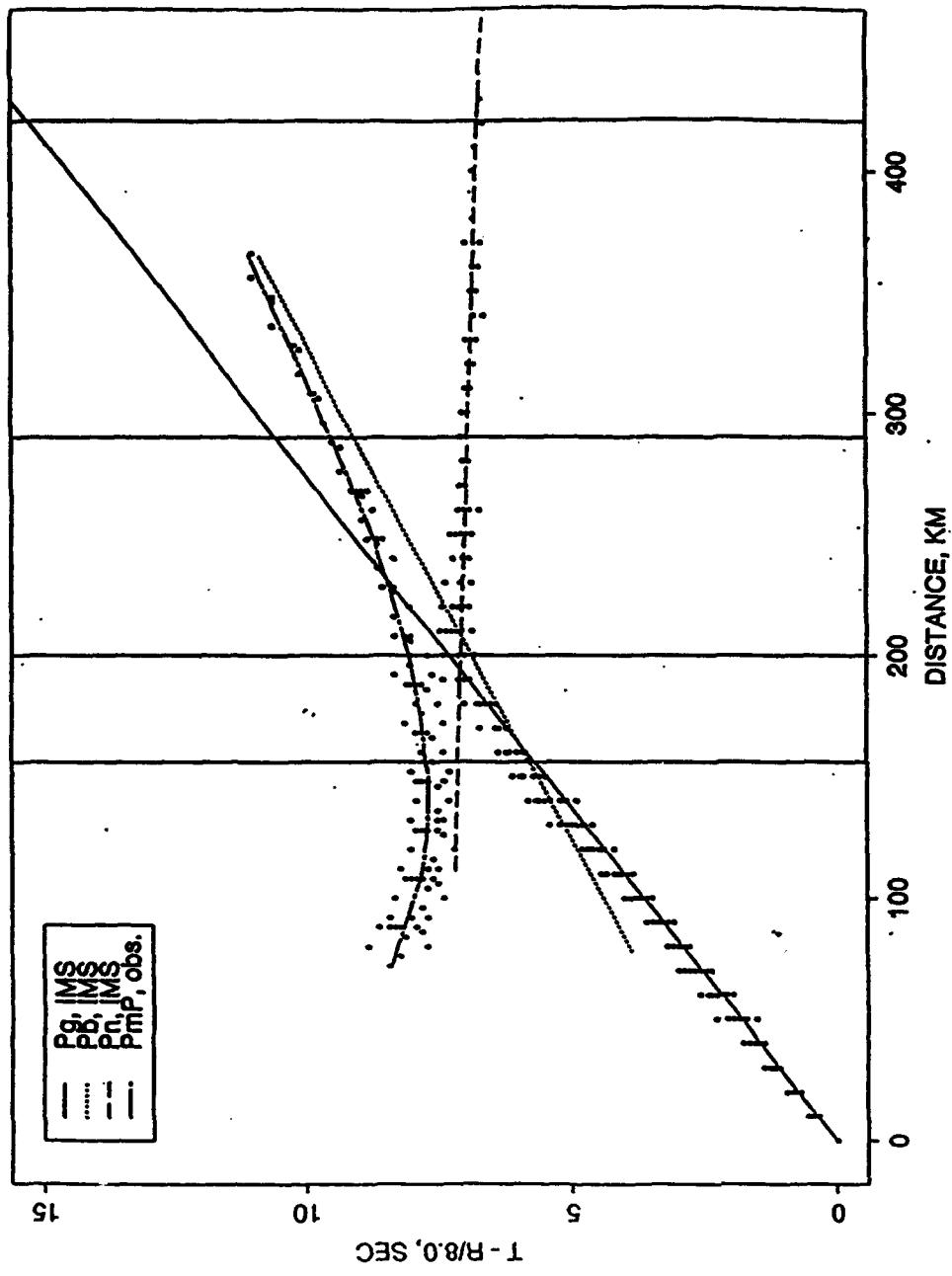
Figure 26: Comparison of *Pg*, *Pb*, and *Pn* reference travel-time curves used by the IMS (*Pg*, IMS; *Pb*, IMS; and *Pn*, IMS, respectively) with P-wave travel-time observations for major regional phases (dots), recorded on the POLAR DSS profile. The *PmP* travel-time curve (*PmP*, obs.) was constructed by smoothing the DSS observations. Vertical solid lines are distances from the ARCESS array to Varanger (156 km), Kiruna (287 km), and Eli-jaervi (421 km).

S-WAVE TRAVEL-TIMES FOR POLAR DSS PROFILE
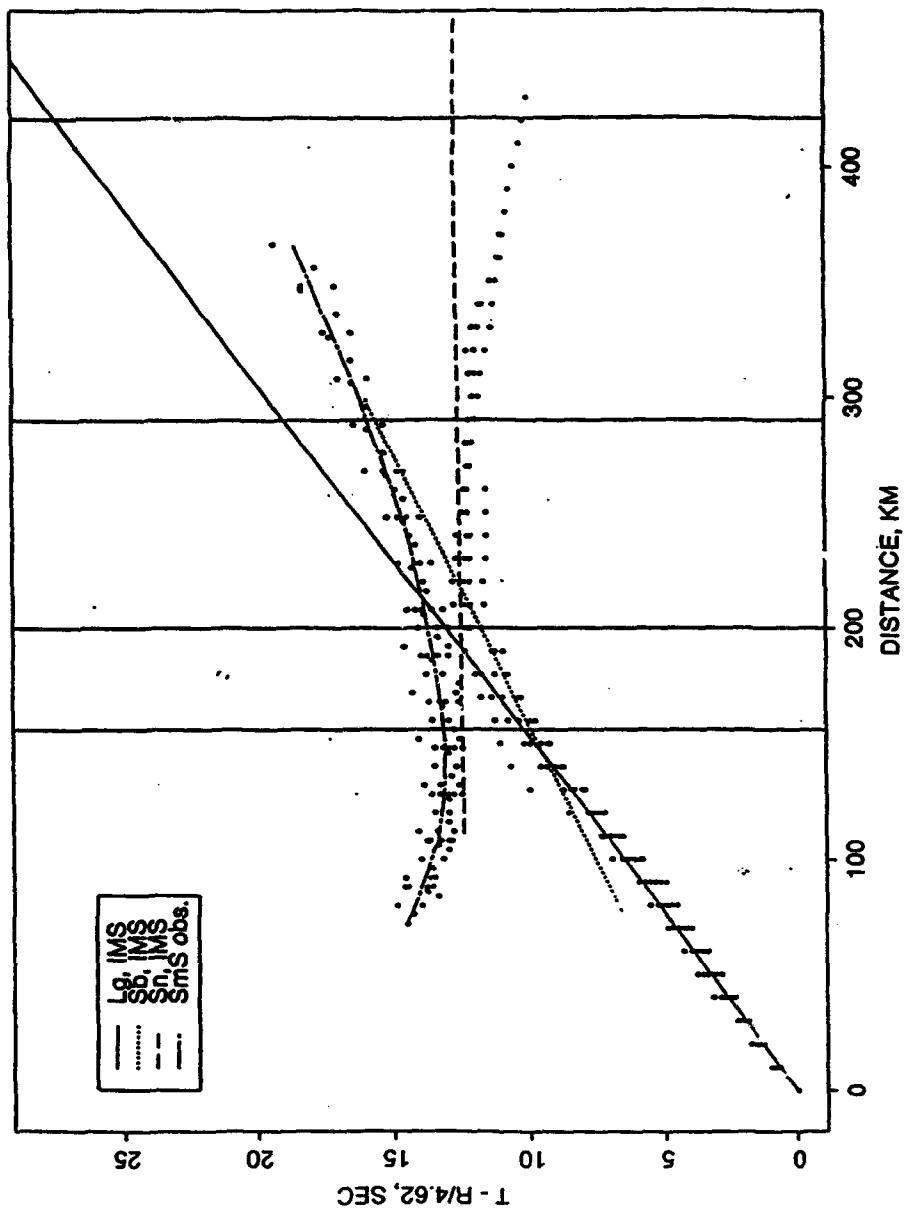
Figure 27: Comparison of Lg, Sb, and Sn reference travel-time curves used by the IMS (Lg, IMS; Sb, IMS; and Sn, IMS, respectively) with S-wave travel-time observations for major regional phases (dots), recorded on the POLAR DSS profile. The SmS travel-time curve (SmS obs.) was constructed by smoothing DSS observations. Vertical solid lines are distances from the ARCESS array to the Varanger (156 km), Saattopora (200 km), Kiruna (287 km), and Eljaervi (421 km) mines.

52

over point and a distance of about 300 km. Beyond 300 km, *Sn* was observed to arrive systematically earlier.

We note, that *PmP* and *SmS*-waves were not included in the initial list of major regional phases for the IMS, but these waves can be easily incorporated and used for event locations. Indeed, the IMS was specifically designed to incorporate new knowledge of this kind as it emerges from research. Examples of using *PmP*-wave for regional event locations were recently published [Quin and Thurber, 1992].

Figure 28 and Figure 29 show waveforms recorded at ARCESS of selected mine blasts from the Varanger and Kiruna mines. Phase identifications determined by the IMS using an automated procedure and after review by an analyst are marked above each waveform. Vertical lines running through all traces are labeled at the top with the phase identification based on DSS data, using travel times form Figures 26 and 27.

For events at both mines, we note that the beginning of the intensive waves within the *S*-wave group were identified in the IMS mainly as *Lg*. Despite the similarity in the waveforms, there is a considerable amount of scatter in the *Lg* phase picks, which is the main cause of the distance scatter in the event locations. Based on our interpretation using DSS data, the wave labeled as *Lg* by the IMS is actually *SmS*. Difference between the *SmS* and *Lg* travel-time curves are distance dependent and may be seen to explain the observed distance bias for event locations in Table 5. For example, the *Lg* travel-time curve from the IMS bulletin is approximately 3 seconds earlier than *SmS* at the distance of the Varanger mine blasts. Interpreting *SmS* as *Lg*, therefore, results in a biased location *away* from ARCESS. At the distance of Scattopora, about 200 km, the *Lg* curve passes through the *SmS* observations and thus there is no resulting bias from interpreting *SmS* as *Lg*. At the greater distances of the Kiruna and Elijaervi mines, the *Lg* curve is 3 seconds and (perhaps) 6 seconds, respectively, later than *SmS*, resulting in biases *toward* the station if *SmS* is interpreted to be *Lg*.

Our *SmS* interpretation of the wave labeled as *Lg* by the IMS is consistent with studies of major regional phases recorded by the NORESS, ARCESS, and FINESA arrays within the Baltic shield [Vogfjord et al., 1991; Vogfjord and Langston, 1990, 1992] and results of modelling *Lg*-wave propagation [Kennett, 1992a, 1992b]. *Lg* is believed to be a superposition of *S*-waves post-critically incident on the Moho and multiply reflected in the crust [Bouchon, 1982; Campillo and Paul, 1992; Kim, 1987]. The *Lg* group velocity is near 3.5 km/sec and the phase has predominant frequencies of 1-2 Hz and lower [Press and Ewing, 1952; Kennett et al., 1985; Ruzaikin et al., 1977]. *SmS* consists of pre-critical, critical, and post-critical reflected shear waves from the Moho. Analysis of DSS data suggests that *SmS* has a phase velocity larger than that reported for *Lg* [for a review of *Lg* phase and group velocity measurements, see e.g. Blandford, 1981].

Figure 30 shows the apparent velocity for the phase identified as *Lg* by the IMS as a function of distance from the ARCESS array. Also shown in Figure 30 is the *SmS* apparent velocity curve inferred from the POLAR DSS profile. The *SmS* curve may be seen to be a good fit to the IMS data within the distance range from 100 to 400 km, approximately. At distances between 400 and 1,000 km, typical *Lg* apparent velocities (slightly above 3.5 km/sec) are observed. At distances less than 100 km, however, the apparent velocity inferred from the IMS observations is between 4.0-5.0 km/sec. These values are too large for *Lg* and too small for *SmS*, but are typical for reflected waves from mid-crustal boundaries in the Baltic shield [Luosto et al., 1989; Hauser
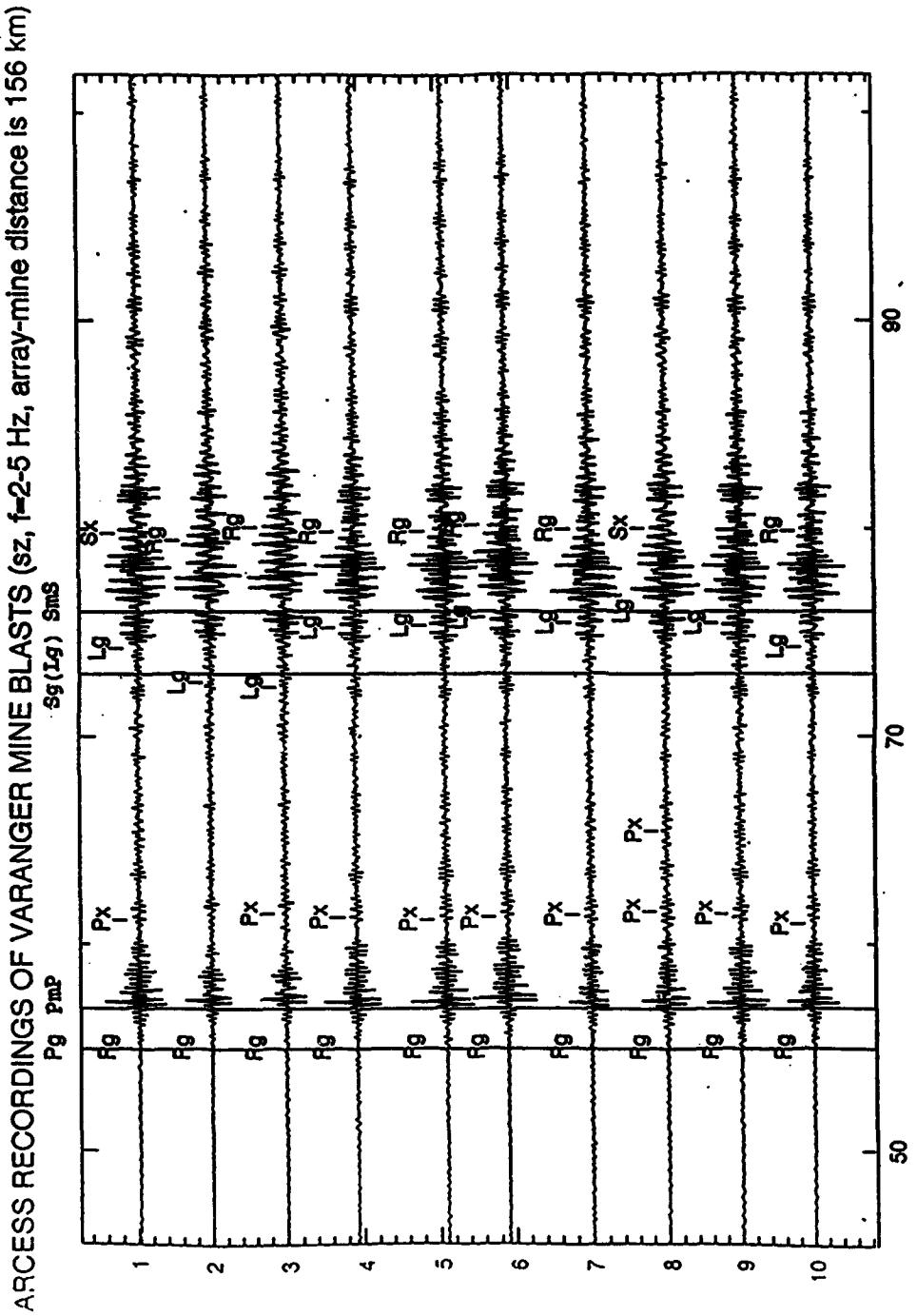
Figure 28: ARCESS recordings (using a bandpass filter of 2 to 5 Hz) of selected Varanger mine blasts (central vertical short-period channels). Phase identification, indicated above each trace are times of arrivals of the expected major P- and S-phases (Pg, PmP, Sg, and SmS) inferred from the POLAR profile observations for the distance of 156 km between ARCESS and the Varanger mine (see the Figures 14 and 15). Note that the most prominent P arrivals, PmP was not used in the IMS analysis. Sg and Lg travel-time curves are identical at this distance. The most prominent arrival in the S group was generally interpreted by the IMS as Lg.

54

ARCESS RECORDINGS OF SELECTED KIRUNA MINE BLASTS. R=290 km
(central vertical short period channels, f=2-8 Hz)

solid lines - DSS data   dashed line - IMS data
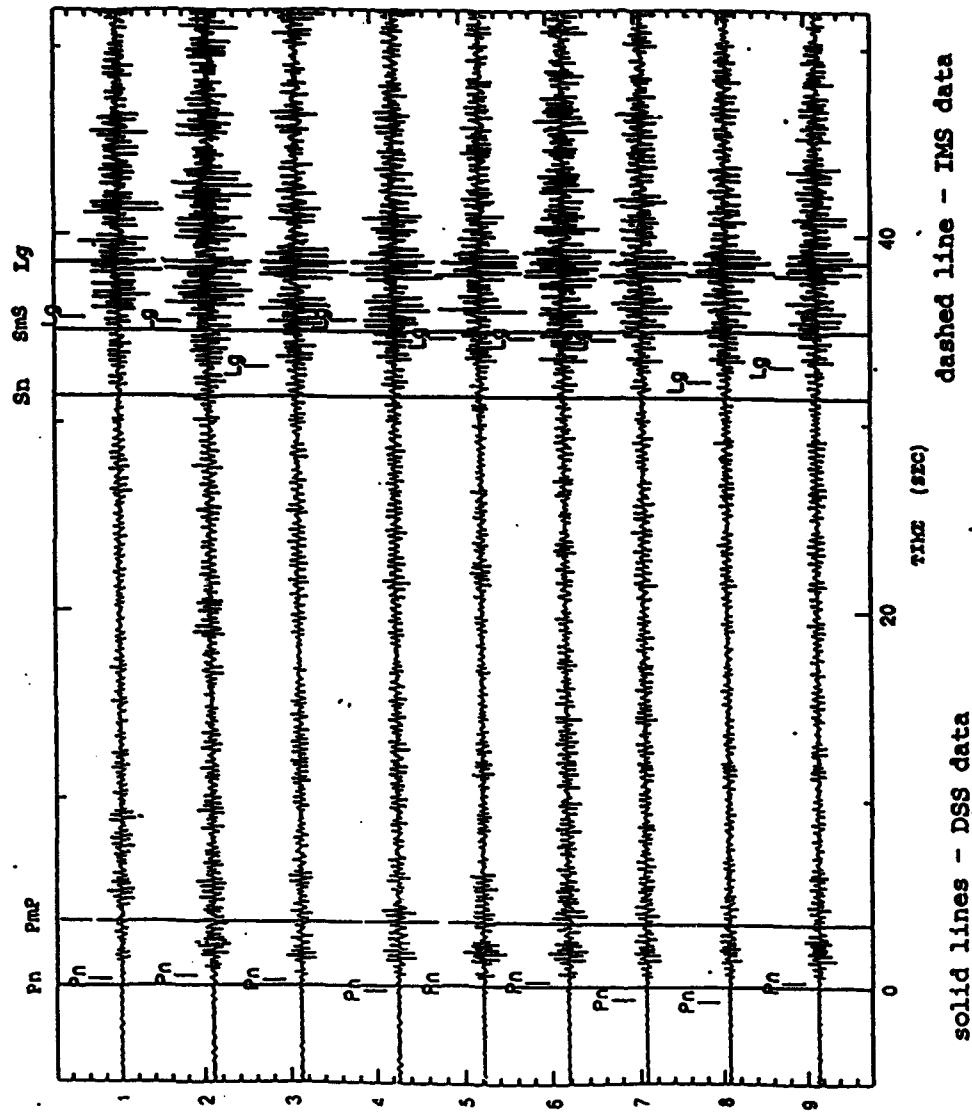
Figure 29: ARCESS recordings (using a bandpass filter of 2 to 8 Hz) of selected Kiruna mine blasts (central vertical short-period channels). Phase identifications indicated above each trace are based on the IMS bulletin. Vertical solid lines are times of arrivals of major *P*- and *S*-phases (*Pn*, *PmP*, *Sn*, and *SmS*) inferred from the POLAR profile observations for the distance of 287 km between ARCESS and the Kiruna mine. The vertical dashed line is the *Lg*-wave arrival time according to the IMS reference travel-time tables. *PmP* is not detectable, but the start of the intensive waves in the *S* group appears to be *SmS*.
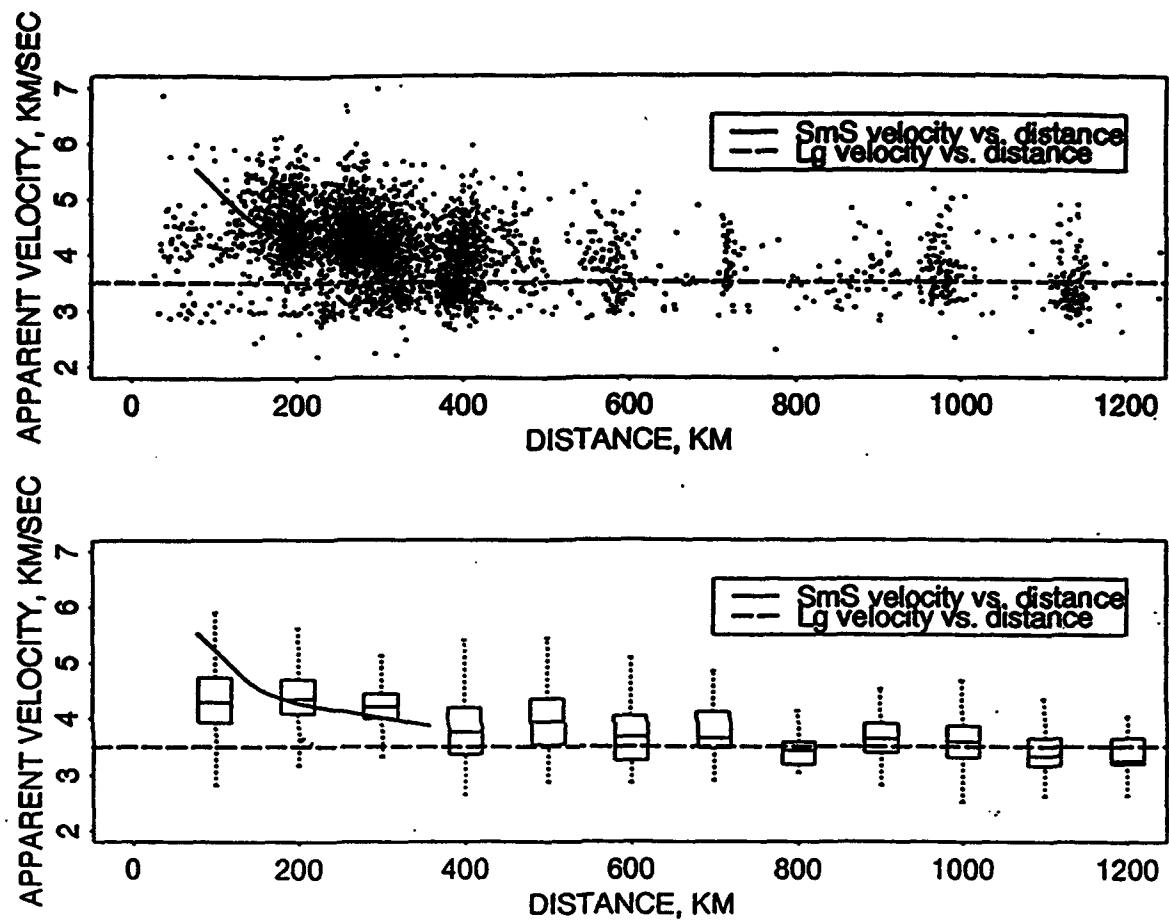
Figure 30: Top: *Lg* apparent velocity vs. distance from the ARCESS array according to *f-k* analysis done by the IMS (dots). Bottom: box plots vs. distance for the same IMS data (dots) shown above. Boxes were calculated for 100 km distance windows. The horizontal line in the interior of the each box is located at the median of the data. The height of each box is the difference between the third quartile of the data and the first quartile. The dotted vertical lines extend to the extreme values of the data. Top and bottom: the solid line is the *SmS* apparent velocity vs. distance curve inferred from the POLAR DSS profile observations; the dashed horizontal line indicates 3.5 km/sec, the *Lg*-wave group velocity.

and Stangl, 1990]. These arrivals can be seen on the DSS profile in Figure 25 (top) at distances less than 100 km.

Figure 31 shows that the predominant frequencies of the phase identified as Lg by the IMS decreases with distance from 8-10 Hz at 100 km to 2-4 Hz at 400 km. Beyond 400 km, the mean frequencies approach 2 Hz or less, which is more typical for Lg energy. Since the recorded events with only a few exceptions have similar magnitudes, and one can see a sharp frequency decrease for distances greater than 400 km, variations in the dominant frequency are probably not due to systematic differences in the source size or attenuation. High frequencies, such as those observed at distances less than 400 km, are atypical for Lg-waves and support a SmS interpretation.

We conclude that the first high amplitude phases recorded .within the S-wave group between 100-400 km in the northern Baltic shield and having apparent velocities of approximately 5.0 km/sec to 4.0 km/sec are SmS-waves, and the high amplitude phases recorded at distances greater than 400-500 km are Lg-waves having apparent velocities of approximately 3.5 km/sec. We have shown that mis-identification of SmS as Lg creates a distance dependent bias in event locations at distances from approximately 100 km up to 400-500 km. The pronounced bias was not observed at about 200 km because this is the cross-over distance for the Lg and SmS travel-time curves.

There are also other sources of phase mis-identifications. For example, we have noted that PmP on ARCESS recordings of the Elijaervi mine blasts have been mis-identified as Pg. It was also recently shown that GERESS recordings of Pg have been mis-identified as Pn [Grant et al., 1993]. Long-range profile observations might be extremely helpful in such cases for improvement of phase identifications.

Relocations of the Kiruna mine blasts

To test the influence of different factors on regional event locations, we relocated two groups of Kiruna mine blasts: the first located by data from ARCESS alone (25 events), and the second by data from two or three arrays, including ARCESS (29 events). For these tests we used the LocSAT code (S. Bratt and W. Nagy, 1991), the same algorithm that was used for the IMS event locations. However, we substituted the new MRS travel-time curve for the standard IMS Pn curve, and we included SmS travel times from Figure 27. The phase at ARCESS labeled Lg by the IMS was renamed SmS, but all other phase designations and the arrival times were unchanged from the IMS picks. Results are given in Table 6, which shows that the distance bias is essentially eliminated for locations based on ARCESS alone, and somewhat reduced for locations employing data from two or three stations. Our expectation is that application of the same care in interpretation of data from the other stations that we have applied to ARCESS data would result in further improvements to the two or three stations locations.
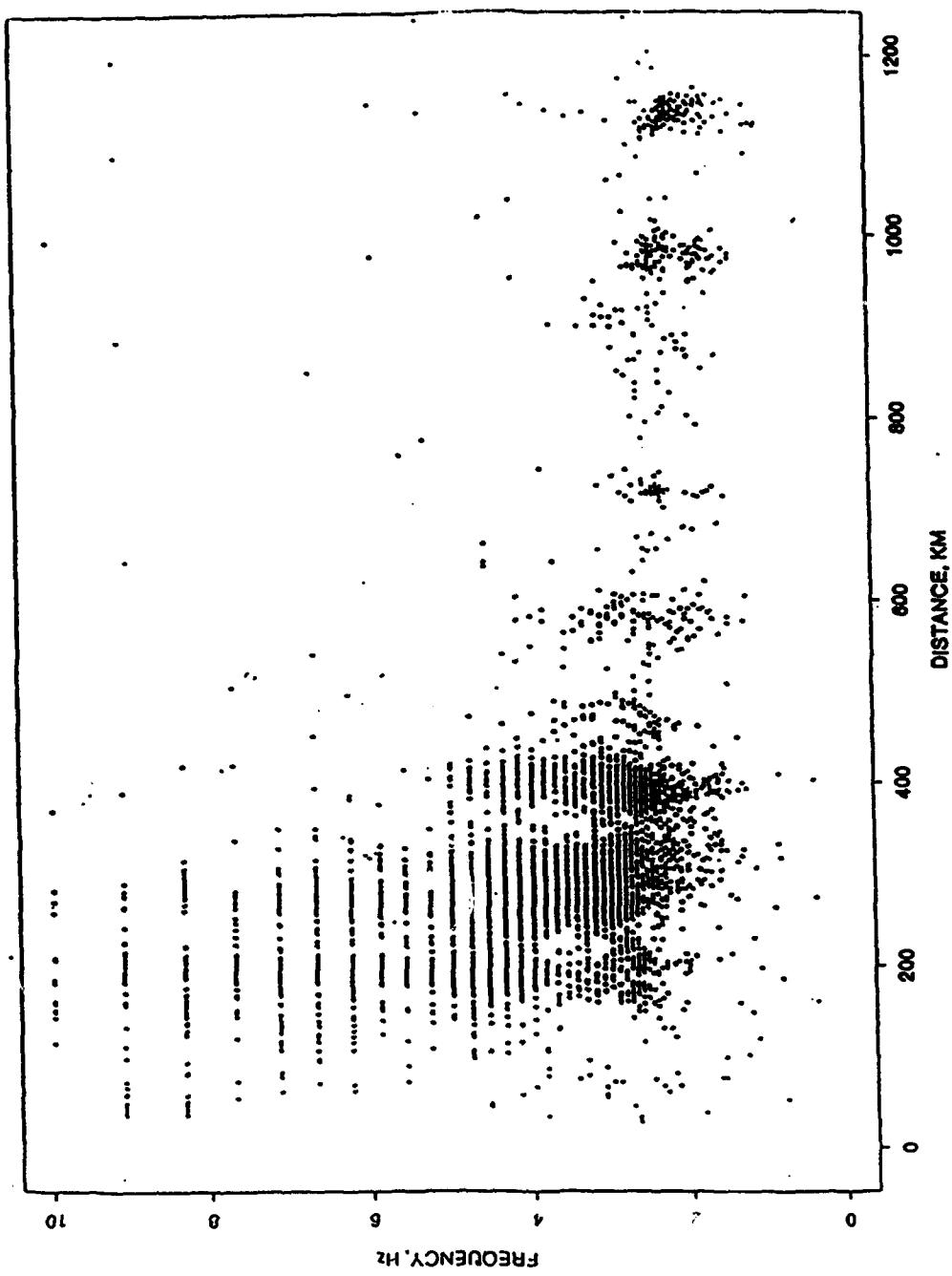
Figure 31: Frequency vs. distance from ARCESS of the phase identified as *Lg* by the IMS.

Table 6: DISTANCE FROM ARCESS TO KIRUNA MINE SHOT LOCATIONS

	mean, in km	median, in km	s.d., in ±km
ARCESS locations			
IMS bull.	270.84	271.83	12.11
new travel-time tables and *SmS*	285.92	287.25	15.29
2 or 3 array locations			
IMS bull.	273.65	276.76	6.04
new travel-time tables and *SmS*	278.95	278.30	6.63

Note: true distance from ARCESS to the Kiruna mine is 287.3 km.

We should explain here that we have used the distance of the epicenters from ARCESS as our measure of improvement, rather than the distance to the mine, because there is also known to be an azimuthal bias attributable to small-scale structural variations in the crust and upper mantle, which produces mislocations comparable to the distance bias (Suteau-Henson et al, 1992) (note also Figure 24) and which tends to obscure the improvements in distance alone that are under investigation here. However, auxiliary tests that we conducted, using azimuthal corrections provided by Suteau-Henson, showed that the combined effect of including azimuthal corrections, improved travel time curves and improved phase identification to ARCESS data reduced the mean location error from about 31 km to about 10 km. Figure 32 shows these revised locations; it may be seen that both the azimuthal and distance bias, which were clearly evident on Figure 24, have been largely removed. As previously noted, there was considerable scatter in the arrival times of *Lg* (*SmS*) as picked by the IMS, which accounts for some of the remaining location scatter. Figure 33 indicates the relative effects of the different changes made in the tests just described. It shows that the most significant change, by far, results from reinterpretation of *Lg* as *SmS*; by itself, this eliminates most of the distance bias from the ARCESS data. The new *Pn* travel time data further reduces the bias, and an independent pick of the arrival times of the strong shear waves -- with the knowledge that it was *SmS* rather than *Lg* -- gave an additional improvement.
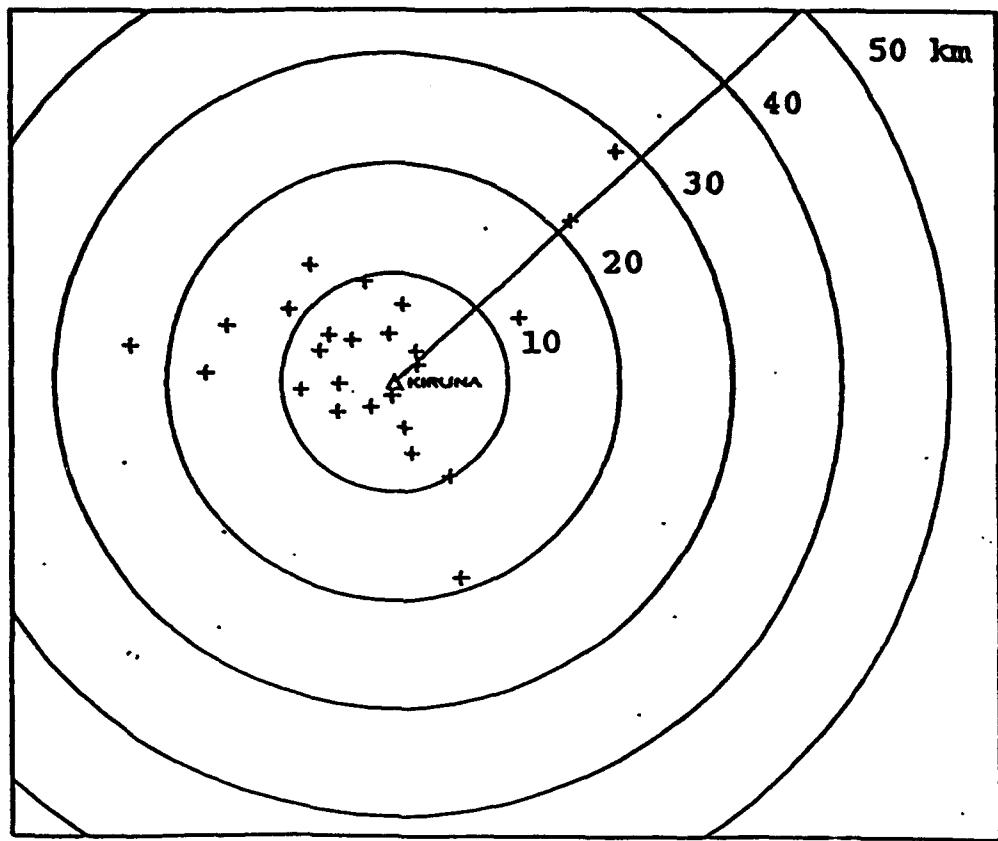
Figure 32: Map of Kiruna mine blasts after relocation. Crosses are events listed in the IMS bulletin and relocated using the new travel-time tables for the Baltic shield (for the *Pn-*, *Sn-* and *SmS*-waves) and corrected for azimuthal bias. Large circles are distances from the Kiruna mine, and a solid line shows the direction from the Kiruna mine to ARCESS.

ARCESS LOCATIONS
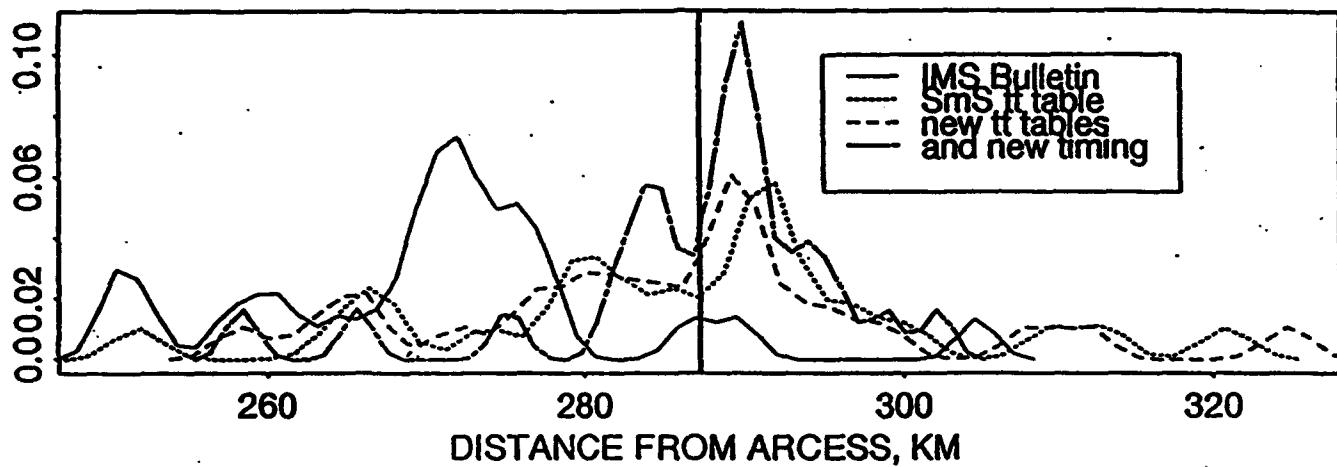
Figure 33: Density plots of distances from ARCESS for Kiruna mine blast locations and relocations. Interpreting the strong shear waves as *Lg* results in the bias evident in the "IMS Bulletin" plots; re-interpreting these waves as *SmS* corrects most of this bias, and application of the new *Pn* curves and more consistent measurements of the arrival times further reduces the bias.

61

Comparison of regional *Pn* travel-time curves for different geological provinces

Global monitoring for nuclear proliferation is expected to be based on an automated system that includes a network of high-quality seismological stations, many equipped with arrays, established at sites having substantially different crustal and upper mantle structures. To assess the influence of regional structural variations on travel times we compared the new MRS *Pn* travel-time curve with similar curves constructed for other regions. Figure 34 shows a comparison of the standard global *Pn* travel-time curves from the Jeffreys-Bullen, Herrin *et al.*, and IASPEI-91 Seismological Tables [Kennett, Engdahl, 1991] with several regional *Pn* travel-time curves inferred from explosion seismology observations. Travel-time curves for the western USA, North American platform, and Canadian shield were constructed by smoothing observations from nuclear explosions [Romney *et al.*, 1962] and chemical explosions in Lake Superior and Hudson Bay [Barr, 1967; Hobson, 1967; Mereu and Hunter, 1969; Green and Hales, 1968; Masse, 1973]. The *Pn* travel-time curves for the Baltic shield, East European and Siberian platforms, and for tectonically active regions of Tien Shan and the Baikal rift zone were inferred from DSS profile observations and from nuclear and large chemical explosion recordings by seismological networks [Vinnik, Ryaboy, 1981; Ryaboy, 1989; Egorkin *et al.*, 1987].

The curves on Figure 34 reveal major differences between travel-times of *Pn*-waves propagating in tectonically active regions and travel-times where propagation was within Precambrian platforms. It may be noted that the *Pn* travel-time curve for a tectonically active region of the western USA is characterized by substantially greater travel-times (up to about 10 sec within the distance range from 500 to 2000 km) than observed within Precambrian geological provinces. *Pn* travel-times for intercontinental tectonically active regions (the Tien Shan and Baikal rift zone) are approximately 5 sec faster than for the western USA but are still slower than *Pn* travel-time curves for the Precambrian platforms and shields.

These *Pn* travel-time variations provide evidence for regions of large scale lateral velocity inhomogeneities in the earth's crust and upper mantle with linear dimensions of approximately 1000-2000 km. The regional travel-time curves, of course, fit different geologic provinces only on the average. To use these curves for event locations, they will need to be adjusted to specific areas and seismic stations. This adjustment means that path-dependent corrections similar to those in Figure 23 will be needed, based on available geological and geophysical data, to account for such smaller scale features as deep sedimentary basins and changes in the Moho depth.

We note that the standard global reference *Pn* curves -- the IASPEI 1991 Seismological Tables, the Jeffreys-Bullen Tables and the Herrin Tables -- do not provide a good fit to any of the observed regional curves especially at distances greater than 500-600 km. We infer that none of these standard global reference curves will produce epicentral location accuracies for regional events that are good enough for global monitoring aims.

Unfortunately, accurate regional travel-time curves specific to many of the regions important for global monitoring do not exist. A key question that we address here is: what would be the initial assumptions about travel-times for such regions? Would we simply apply standard reference curves like the IASPEI 1991? Or can we do better? Fortunately, there is much informa-

COMPARISON OF Pn TRAVEL-TIME CURVES
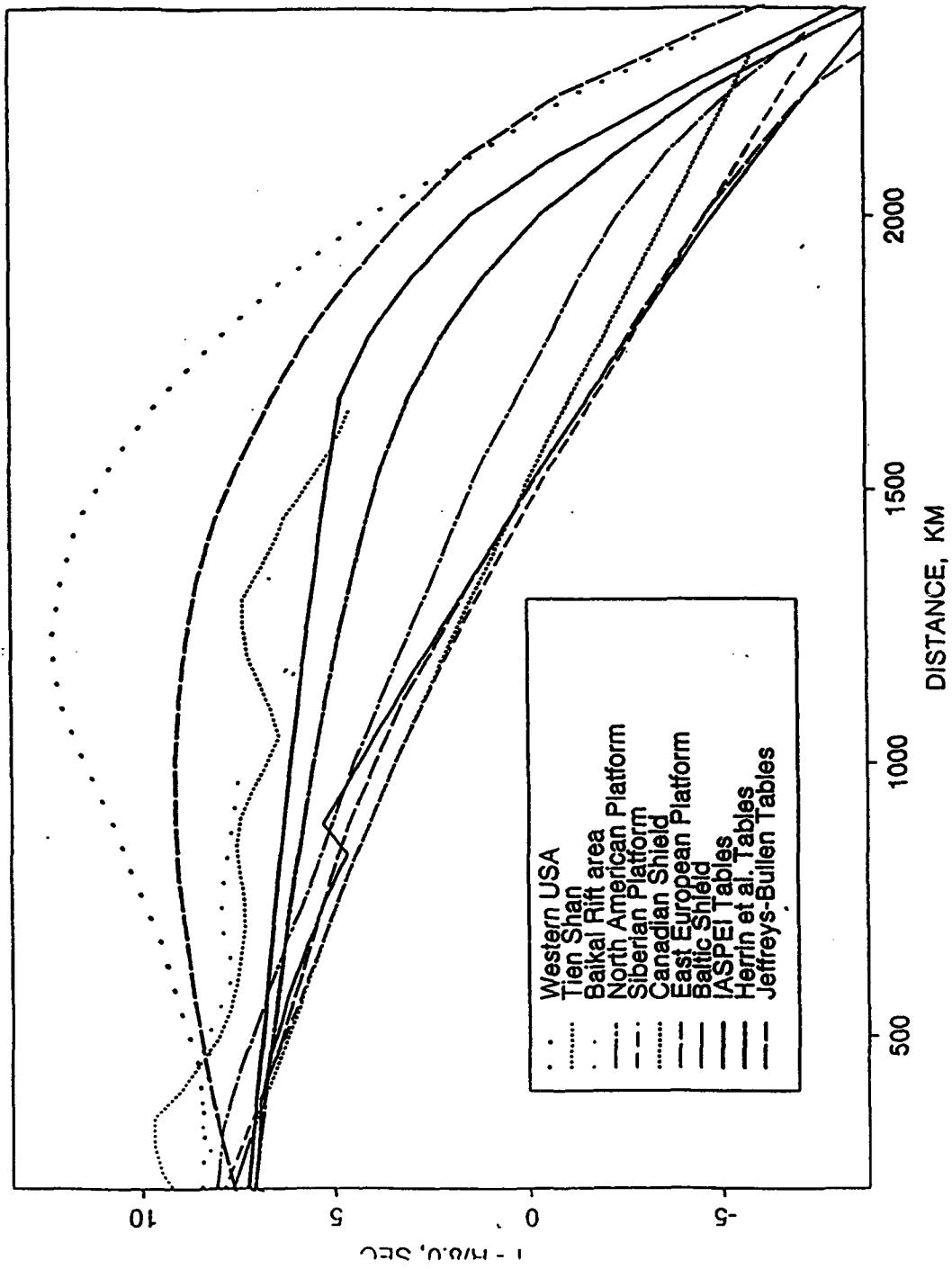
Figure 34: Comparison of regional Pn travel-time curves for different geological provinces with the reference Pn travel-time curves from the Jeffreys and Bullen, Herrin et al., and IASPEI 1991 Seismological Tables. Ancient platforms and shields have the fastest Pn travel-times, and tectonically active regions are substantially slower (up to 10 sec).

63

tion to indicate that we can do better, at least under some circumstances.

Transportability of a *Pn* Travel-Time Curve for Precambrian Shields

The surprisingly good agreement among the *Pn* curves for Precambrian provinces suggests that travel-times observed within these regions might be transportable, within reasonable error, to other similar geological provinces. To test this idea, we first constructed a proposed global *Pn* reference travel-time curve for Precambrian platforms by smoothing and averaging the appropriate *Pn* travel-time curves of Figure 34. We then compared this proposed global *Pn* travel-time curve with observed data from the Australian shield.

Figure 35 (bottom) shows this composite reference *Pn* curve for ancient platforms, as well as boundaries indicating two standard deviations from it (s.d. = ± 0.72 sec). The concept to be tested is that almost all *Pn* travel-times for Precambrian geological provinces should lie within this interval. This conjecture is encouraged by current theories of global tectonics and continental drift proposing that the ancient shield and platform areas of the earth have a common age and origin as a single unit in Pangea.

Observational data came from long-range DSS profiles, and from recordings by seismological networks of large chemical and nuclear explosions, carried out within Australia. Results of these studies, including record sections and travel-time measurements, have been published in numerous papers (Bolt *et al.*, 1958; Doyle and Everingham, 1964; Denham *et al.*, 1972; Finlayson *et al.*, 1974; Muirhead and Cleary, 1977). These data (Figure 35, top, dots) were used to produce a composite *Pn* travel-time curve for the Australian Shield based on explosion seismology observations (Figure 35 top, broken line). The standard deviation of travel-time measurements from this regional *Pn* curve for the Australian shield is ±0.79 sec. A second *Pn* travel-time curve for the Australian shield, based on analysis of earthquakes whose locations and origin time were well determined [Bowman and Kennett, 1993], is also shown on Figure 35 (top, dash-dot line). The *Pn* curve inferred from analysis of earthquake recordings is approximately 1-3 sec earlier than the explosion seismology observations, but generally supports the explosion curve.

When the Australian regional curve is superimposed on our proposed global Pn reference curve for Precambrian shields (Figure 35, bottom), it may be seen to lie within the ±2 s.d. boundaries over its entire range (The *Pn* travel-time curve based on Australian earthquake recordings is also located within the ±2 s.d. interval up to 2000 km distance). As a result of this test, we suggest that our composite global *Pn* travel-time curve can be taken as the initial approximation for other Precambrian provinces where well-established regional curves do not exist. We note that, according to numerous geological studies, the Precambrian geological provinces constitute over half of the continents and include a number of regions where proliferation may be a concern.

Conclusions

For the Baltic shield and neighboring regions, analysis of DSS profile observations and recordings of mine blasts have enabled us to derive a new *Pn* travel-time model, a new method of determining regional and local path-dependent travel-time corrections, and improved phase identification for regional events, which taken together promise to improve the accuracy of seismic

Pn TRAVEL-TIMES FOR AUSTRALIAN SHIELD
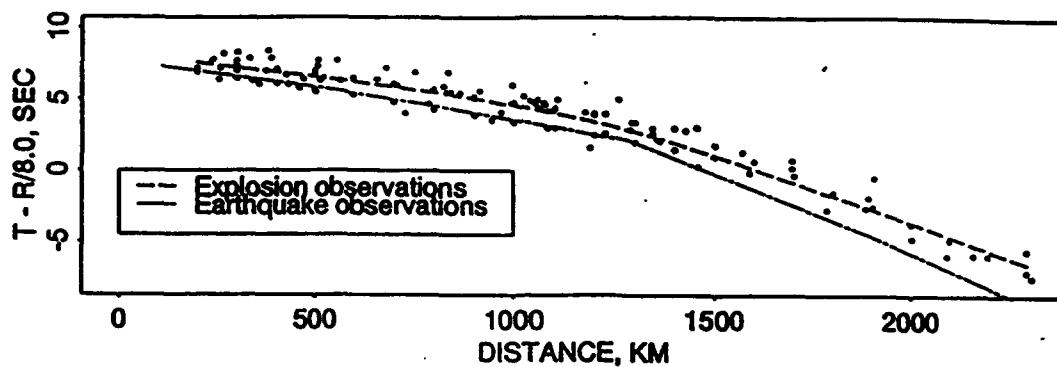
Pn TRAVEL-TIME CURVE FOR ANCIENT PLATFORMS
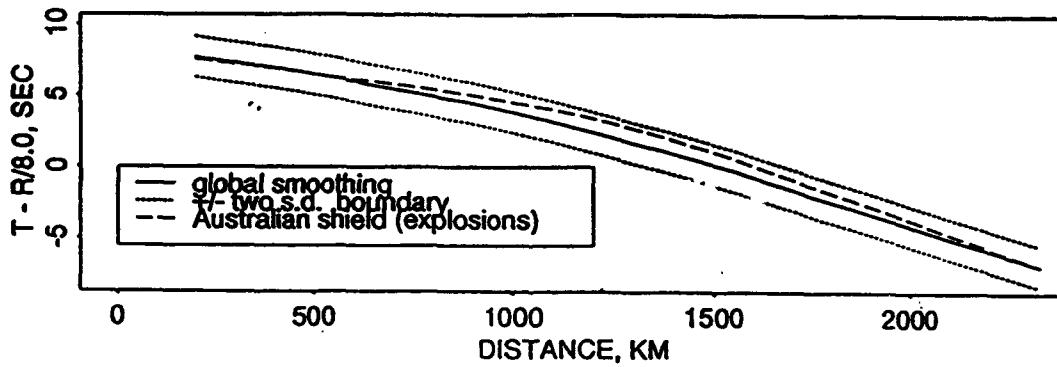
Figure 35: Regional *Pn* travel-time curves for the Australian shield inferred from explosion and earthquake observations (*top*) and proposed globally averaged composite *Pn* travel-time curve for ancient platforms (*bottom*). Dots on the top figure are observations from explosions, and were used to define the curve shown as a dashed line. A separate curve based on earthquake data is also shown for comparison. The Australian explosion curve fits within the ±2 s.d. boundaries on each side of the proposed *Pn* travel-time curve for Precambrian shields, as shown on the bottom figure.

locations in Scandinavia. Results of tests completed on IMS data from Kiruna mine blasts locations incorporating this new information into interpretation of ARCESS data showed improvements in the accuracy of their locations, although significant azimuthal bias remained, and there was still considerable scatter resulting from variations in the semi-automatic phase time picks. Results can probably be improved if we use several arrays for event locations, better define the *Sg* and *Sn* travel-time curves and include *PmP* as well as *SmS* in the location procedures.

Analysis of explosion seismology observations from different large geological provinces of the world showed that large regional travel-time variations of the order of 10 sec for *Pn*-waves (and probably 15-18 sec for *Sn*-waves) can be expected. *Pn* travel-time curves for the Precambrian platforms, which constitute a very large part of continents, are characterized by the smallest *Pn* travel-times. Tectonically active regions are characterized by substantially greater travel-times. With these large and region-dependent travel-time variations, it appears that it will be difficult to produce an accurate regional epicentral location without constructing accurate regional travel-time curves and path-dependent corrections for each seismic station.

Travel-time curves for *Pn* in Precambrian shields and platforms were found to be remarkably consistent with one another, permitting us to define a composite reference *Pn* curve for ancient platforms, with standard deviation of ±0.72 seconds. To test the transportability of this curve to other platforms, we compiled data from the Australian shield and found that it agreed with our reference curve within two standard deviations, encouraging us to believe that this reference curve may be applied generally to similar Precambrian provinces.

For other regions of the continents, including tectonically active regions, arrival times of *Pn* are generally later; variations from region to region, however, are very large. At the time of writing this paper, we have found no method of transporting travel-time curves from one such province to another. In the absence of transportability principles, it appears that individual region-by-region calibrations will be required to obtain good location accuracies.

Acknowledgments

References

BABEL Working Group, Integrated seismic studies of the Baltic shield using data in the Gulf of Bothnia region, *Geophysical Journal International* vol. 112, No. 3, 305-324, 1993a.

BABEL Working Group, Deep seismic reflection/refraction interpretation of crustal structure along BABEL profiles A and B in the southern Baltic Sea, *Geophysical Journal International* vol. 112, No. 3, 325-343, 1993b.

Bache, T.C., S.R. Bratt, J. Wang, R.M. Fung, C. Kobryn, and J.M. Given, The Intelligent Monitoring System, *Bull. Seism. Soc. Am.* 80, 1833-1851, 1990.

Barr K.G., Upper mantle structure in Canada from seismic observations using chemical explosions, *Canadian Journal of Earth Sciences* 4, 5, 961-975, 1967.

Bath, M., Average crustal travel-times in Sweden re-examined, *Pure Appl. Geophys.* 119, 1116-1124, 1981.

Blandford, R.R., Seismic discrimination problems at regional distances, in *Identification of seismic sources - Earthquake or Underground Explosion*, D. Reider Publishing Company, Holland, 695-740, 1981.

Bolt, B.A., H.A. Doyle, and D.J. Sutton, Seismic observations from the 1956 atomic explosions in Australia, *Geophys. J. R. astr. Soc.*, v. 1, 135-145, 1958.

Bouchon, M., The complete synthesis of seismic crustal phases at regional distances, *J. Geophys. Res.*, 87, 1735-1741, 1982.

Bratt, S.R. and T.C. Bache, Locating events with a sparse network of regional arrays, *Bull. Seism. Soc. Am.* 78, 780-798, 1988.

Bratt, S.R., H.J. Swanger, R.J. Stead, F. Ryall, and T.C. Bache, Initial results from the Intelligent Monitoring System, *Bull. Seism. Soc. Am.* 80, 1852-1873, 1990.

Bowman, J.R. and B.L.N. Kennett, The velocity structure of the Australian shield from seismic travel-times, *Bull. Seism. Soc. Am.* 83, 1, 25-37, 1993.

Campillo M. and A. Paul, Influence of the lower crustal structure on the early coda of regional seismograms, *J. Geophys. Res.*, 97, 3405-3416, 1992.

Cassell, B.R., S. Mykkeltveit, R. Kanestrom, and E.S. Husebye, A North sea-southern Norway seismic crustal profile, *Geophys. J. R. astr. Soc.* 72, 733-753, 1983.

Dahlman, O., On Scandinavian crustal travel-times, *The Research Institute of National Defense*, Stockholm, 9, 1967.

Denham D., D.W. Simpson, P.J. Gregson, and D.J. Sutton, Travel times and amplitudes from explosions in northern Australia, *Geophys. J. R. astr. Soc.*, v. 28, 225-235, 1972.

Doyle, H.A. and I.B. Everingham, Seismic velocities and crustal structure in southern Australia, *Journ. Geol. Soc. Aust.*, v. 11, 141-150, 1964.

Egorkin, A.V., S.K. Zuganov, N.A., Pavlenkova, and N.M., Chernyshev, Results of lithospheric studies from long-range profiles in Siberia, *Tectonophysic*, 140, 29-47, 1987.

EUGENO-S Working Group, Crustal structure and tectonic evolution of the transition between the Baltic shield and the North German Caledonides, *Tectonophysics* 150, 253-348, 1988.

Fielding, E., M. Barazangi, and B. Isacks, A network-accessible geological and geophysical data base for Eurasia, North Africa, and the Middle East, *Proceedings of 15th Annual PL/ARPA Seismic Research Symposium*, 8-10 September 1993, Vail, Colorado, 93-99, 1993, PL-TR-93-2160, ADA271458.

Finlayson, D.M., J.P. Cull, and B.J. Drummond, Upper mantle structure from the Trans-Australia seismic survey (TASS) and other seismic refraction data, *Journ. Geol. Soc. Aust.*, v. 21, 4, 447-458, 1974.

Grant L., F. Ryall, and J. Coyne, CSS ground-truth database: update and case study, *Proceedings of 15th Annual PL/ARPA Seismic Research Symposium*, 114-120, 1993, PL-TR-93-2160, ADA271458.

Green, R.W.E. and A.L. Hales, The travel-times of P-waves to 30 in the central United States and upper mantle structure, *Bull. Seism. Soc. Am.* 58, 1, 267-289, 1968.

Guggisberg, B., Eine zweidimensionale refraktionsseismische interpretation der Geschwind-igkeits - Tiefen - Struktur des oberen Erdmantels unter dem Fennoskandischen schild (Projekt FENNOLORA), *Diss. ETH Nr. 7945*, Zurich, 199, 1986.

Hauser F. and R. Stangl, The structure of the crust and lithosphere in Fennoscandia derived from a joint interpretation of P- and S-wave data of the FENNOLORA refraction seismic profile, in *Proceedings of the sixth workshop on the European geotraverse project*, 71-92, 1990.

Hobson, G.D., Hudson Bay crustal seismic experiment: time and distance data, *Canadian Journal of Earth Sciences* 4, 5, 879-899, 1967.

Husebye, E.S., J. Hovland, A. Christoffersson, K. Astrom, R. Slunga, and C.E. Lund, Tomograph-ical mapping of the lithosphere and asthenosphere beneath southern Scandinavia and adjacent areas, *Tectonophysics* 128, 229-250, 1986.

Imaging and understanding the lithosphere of Scandinavia and Iceland, *Tectonophysics* 189, 344, 1991.

Kennett, B.L.N., S. Gregersen, S. Mykkeltveit, and R. R. Newmark, Mapping of crustal heteroge-neity in the North sea basin via the propagation of *Lg*-waves, *Geophys. J. R. astr. Soc.* 83, 299-306, 1985.

Kennett, B.L.N. and E.R. Engdahl. Travel-times for global earthquake location and phase identi-fication, *Geophys J. Int.* 105, 429-465, 1991.

Kennett, B.L.N. The distance dependance of regional discriminants. *Papers Presented at 14th Annual PL/DARPA Seismic Research Symposium,* 233-238, 1992a, PL-TR-92-2210, ADA256711.

Kennett, B.L.N. Phase identification and location for regional and teleseismic events. *Papers Pre-sented at 14th Annual PL/DARPA Seismic Research Symposium*, 239-244, 1992b, PL-TR-92-2210, ADA256711.

Kim, W.-Y., Modelling short-period crustal phases at regional distances for the seismic source parameter inversion, *Phys. Earth Planet. Inter.*, 47, 159-178, 1987.

Kinck, J.J., E.S. Husebye, and F.R. Larson, The Moho depth distribution in Fennoscandia and the regional tectonic evolution from Archean to Permian times, *Manuscript, Dept. of Geology*, Oslo University, 1-57, 1990.

Korhonen, H., I.P. Kosminskaya, I. Azbel, N. Sharov, V. Zagorodny, and U. Luosto, Comparison of crustal structure along DSS profiles in SE Fennoscandia, *Geophys. J. Int.* 103, 1, 157-162, 1990.

Lund, C.E., The fine structure of the lower lithosphere underneath the Blue Road profile in northern Scandinavia, *Tectonophysics* 56, 111-122, 1979.

Luosto, U., E. Lanne, H. Korhonen, A. Guterh, M. Grad, R. Materzok, and E. Perchuc, Deep structure of the Earth's crust on the SVEKA profile in central Finland, *Annales Geophysicae* 2, 5, 559-570, 1984.

Luosto, U., E.R. Flueh, C.-E. Lund and working group, The crustal structure along the POLAR profile from seismic refraction investigations, *Tectonophysics* 162, 51-85, 1989.

Luosto, U., T. Tiira, H. Korhonen, I. Azbel, V. Burmin, A. Buyanov, I. Kosminskaya, V. Ionkis, and N. Sharov, Crust and upper mantle structure along the DSS Baltic profile in SE Finland, *Geophys. J. Int.* 52, 119-130, 1990.

Luosto, U., Moho map of the Fennoscandia shield based on seismic refraction data, in *Structure and dynamics of the Fennoscandian lithosphere*, Helsinki, 43-50, 1991.

Masse R.P., Compressional velocity distribution beneath central and eastern North America, *Bull. Seism. Soc. Am.*, 63, 3, 911-935, 1973.

Mereu, R.F. and J.A. Hunter, Crustal and upper mantle structure under the Canadian shield from project Early Rise data, *Bull. Seism. Soc. Am.*, 59, 1, 147-165, 1969.

Mereu, R.F., S. Mykkeltveit, and E.S. Husebye, Fennolora recordings at NORSAR, *J. Geophys.* 52, 119-130, 1983.

Muirhead, K.J., J.R. Cleary, and D.M. Finlayson, A long-range seismic profile in South-eastern Australia, *Geophys. J. R. astr. Soc.*, 48, 509-519, 1977.

Mykkeltveit, S., F. Ringdal, T. Kvaerna, and R.W. Alewine, Application of regional arrays in seismic verification research, *Bull. Seism. Soc. Am.* 80, 1777-1800, 1990.

Porkka, M.T., H. Korhonen, and K. Saviaro, Study of P-wave velocity below Moho, *Pure and Applied Geophysics* 97, 51-56, 1972.

Press, F. and M. Ewing, Two slow surface waves across North America, *Bull. Seism. Soc. Am.* 42, 219-228, 1952.

Proceedings of the colloquium on deep seismic sounding in northern Europe, *The Swedish natural science research council, Stockholm*, 98, 1971.

Proceedings of the sixth workshop on the European geotraverse project, *The Commission of the European communities*, 457, 1990.

Quin, H.R., and C.H. Thurber, Seismic velocity structure and event relocation in Kazakhstan from secondary P phases, *Bull. Seism. Soc. Am.*, 82, 2494-2510, 1992.

Romney, C.F., B.G. Brooks, R.H. Mansfield, D.S. Carder, J.N. Jordan, and D.W. Gordon, Traveltimes and amplitudes of principal body phases recorded from GNOME, *Bull. Seism. Soc. Am.* 52, 1057-1074, 1962.

Romney, C.F., On-Site Inspection for Nuclear Test Verification, *Arms Control Verification and The New Role of On-Site Inspection*, Lewis Dunn and Amy Gordon, Eds., Lexington Books, 1990.

Ruzaikin, A.I., I.L. Nersesov, V.I. Khalturin, and P. Molnar, Propagation of Lg and lateral variations in crustal structure in Asia, *J. Geophys. Res.*, v. 82, No. 2, 307-316, 1977.

Ryaboy, V., Upper mantle structure studies by explosion seismology in the USSR, *DELPHIC*, 154, 1989.

Ryaboy, V., Upper mantle structure along a profile from Oslo (NORESS) to Helsinki to Leningrad, *Bull. Seism. Soc. Am.* 80, 2194-2213, 1990.

Ryaboy, V., R.J. Stead, and L.T.Grant, Relocation of regional seismic events recorded by IMS within the Baltic Shield using path-dependent travel-time curves calibrated by DSS data, *Seism. Res. Letters* 63, No. 1, 44, 1992.

Ryaboy, V., New regional travel-time tables for Scandinavia, *EOS*, April 20, 1993.

Sellevoll, M.A., and P. Pomeroy, A travel-time study for Fennoscandia, *Arbok for Universitetet i Bergen, Mat.-Naturv. Serie* 9, 1-29, 1968.

Sharov, N.V., Lithosphere of the Baltic shield according to seismic data, in *Structure and dynamics of the Fennoscandian lithosphere*, Helsinki, 87-96, 1991.

Stangl, R., Die struktur der lithosphere in Schweden, abgeleitet aus einer gemeinsameninterpretation der P- und S- wellen registrierungen auf dem FENNOLORA profil. *Phd. Thesis*, University of Karlsruhe, 154, 1990.

Structure and dynamics of the Fennoscandian lithosphere, *Institute of seismology of Helsinki university*, 120, 1991.

Study of the deep structure beneath the eastern part of the Baltic shield and adjacent water areas by seismic methods, *Kola branch Geological institute of the Soviet Academy of Sciences*, Apatity, 116, 1986.

Suteau-Henson, A., Three-component analysis of regional phases at NORESS and ARCESS: polarization and phase identification, *Bull. Seism. Soc. Am.* 81, 2419-2440, 1991.

Suteau-Henson, A., V.Z. Ryaboy, F. Riviere-Barbier, H. Israelsson, and J.A. Carter, Analysis of IMS locations of mine blasts and RMS *Lg* magnitudes in Scandinavia, *Proceedings of 14th Annual PL/DARPA Seismic Research Symp*, 401-407, 1992, PL-TR-92-2210, ADA256711.

Vinnik, L.P. and V.Z. Ryaboy, Deep structure of the East European platform according to seismic data, *Physics of the Earth and Planetary Interiors*, 25, 27-37, 1981.

Vogfjord, K.S. and C.A. Langston, Analysis of regional events recorded at NORESS, *Bull Seism. Soc. Am.* 80, 2016-2031, 1990.

Vogfjord, K.S., Ben Yan and C.A. Langston, Composition of short-period regional phases inferred from Fennoscandian array data, in *Papers presented at 13th Annual PL/DARPA Seismic Research Symposium*, 474-479, 1991, PL-TR-91-2208, ADA241325.

Vogfjord, K.S. and C.A. Langston, Short-period regional phases from Fennoscandian arrays, *Papers presented at 14th Annual PL/DARPA Seismic Research Symposium*, 450-456, 1992 PL-TR-92-2210, ADA256711.

CSS Ground-Truth Database:
Update to Version 1 Handbook

L. Grant, J. Coyne, F. Ryall

Ground-Truth Database Overview

This report is an update to the CSS Ground Truth Database as described by Grant et al. (1993). The objective of the Ground-Truth Database (GTDB) is to provide events of known type to facilitate research on the seismic discrimination problem. The GTDB is a collection of regional waveforms and carefully-reviewed phase parameters generated by seimic events of known type (i.e. earthquake, quarry blast, etc.) where the event type is confirmed by some means in addition to seismic observations. The event type is stored in the etype field of the origin table and is defined as follows.[*]

etype	DESCRIPTION
qb	Quarry or mine blast confirmed by quarry
qb+	Quarry or mine blast with designed shot information- ripple fired
qb++	Quarry or mine blast with observed shot information- ripple fired
qbx	Quarry or mine blast - single shot
qmt	Quarry or mining-induced events: tremors and rockbursts
ex	Explosion of known origin; e.g. calibration, construction, etc.
nu	Nuclear explosion
nc	Nuclear cavity collapse
eq	Earthquake
eq+	Earthquakes in a swarm or aftershock sequence
eq++	Felt earthquake
o	Other source of known origin
u	Undetermined or conflicting information

---

[*] Note: This is a minor revision of Table 5 of "CSS Ground Truth Database" Version 1 Handbook (Grant et al., 1993) (The ex definition has been clarified.)

In addition to the above changes to the range of the etype field, another modification to CSS 3.0 tables is that the origin Table is used to store event information collected from experts in the local areas. This has resulted in a "hybrid" origin Table that contains, in each field, the best information available. To indicate this mixed origin entry, the author field of the origin table is set to "HYBRID".

Currently, the GTDB includes 288 known events located in Central Europe and Scandinavia and recorded on stations in the IMS2 and GSETT-2 networks. The events are organized into 10 distinct datasets, based on geographical location and/or source of information.

The GTDB is available through the ORACLE database account called "gtdb" and is accessible through SQL*Plus on hugo or through CenterView. Version 1 and Version 2 have been combined into the gtdb account. The old discrim1 account will be removed on July 1, 1994.

Version 1 (Datasets 1-3), previously discrim1 account;

Version 2 (Datasets 4-10).

The GTDB has benefited greatly from the input and feedback of the users. This project was cancelled in January of 1994 and no new datasets are currently being added. However, please continue to notify us of problems encountered in using the data.

References

Grant, L., J. Coyne, F. Ryall (1993). CSS Ground-Truth Database: Version 1 Handbook. SAIC Scientific Report No. C93-05, August 1993.

Version 1 Documentation

The documentation for Version 1 was distributed in late August 1993. If you did not recieve a copy and you would like one please notify Lori Grant (grant@seismo.css.gov or 703-276-7900).

title: CSS Ground Truth Database: Version 1 Handbook
number: Technical Report C93-05
date: August 1993
summary: The handbook details the purpose of the GTDB, the method
               of building it, the GTDB Schema, and specifics about each of
               the three datasets comprising Version 1. It also contains
               a plot of sample waveforms from each of the 82 events.

Version 1 Updates

Two of the datasets in Version 1 have been updated since publication of the Version 1 Handbook. The two changes briefly noted here arealso documented in the log file in

~grant/discrim1_updates/discrim.log   on the machine SOL.

Dataset #1: Vogtland

The etype of the Vogtland quarry blasts has been changed from qb to qb+ to indicate that there is some additional information available. In this case, the total charge size in kg is stored in the minex table. The minex and origin tables are linked through evid.

Dataset #3: Lubin

New locations have replaced the locations published in the Version 1 Handbook. All location calculations have been performed by the mines on the basis of arrival times and/or other data they might use (for instance the location of damage, if any). The Institute of Geophysics converted the location data from mine coordinates to geographical coordinates. The error in previously published locations occurred during the conversion. The Institute of Geophysics has calculated the origin times and magnitudes.

Version 2

Overview

Version 2 of the GTDB comprises 7 datasets for a total of 206 known events. 10 events of unkown origin are also included because of thier temporal proximity to the known events. With the exception of the Dataset 4, all resulted by obtaining a list of events from a published paper or from the author of a published paper who used the events in a study. With the exception of Dataset 6 the events within a given dataset are actually a cluster of events from one area. Dataset 6 is a subset of the database of known events being complied at the Ruhr University, Bochum in which events are azimuthally distributed around GERESS and generally have only one representative event in each area. Datasets 8-10 (121 events) result from NORSAR technical reports and are from the Apatity mining area in the Khibinny Massif.

Waveform data are from the IMS2 network and are supplemented by some GSETT-2 stations for datsets 4 and 6. Additionaly, data from the Apatity 3-C station was supplied by NORSAR staff for the quarry blasts in dataset #9.

Starting with the IMS2 bulletin, parameter data for each event has been carefully re-reviewed by Flori Ryall.

Version 2 Datasets

Dataset #4	Silesia ....
number of events:	31
event type:	mining-induced tremors (qmt)
evid range:	373-1008
reference paper:	none; personal communication from Institute of Geophysics, Polish Academy of Sciences in the form of a list of all events > ml 2.0 occuring in Upper Silesia between 1 Jan 1991 and 30 June 1991.

Dataset #5	Swiss Swarms ....
number of events:	27
event type:	earthquake swarms in Switzerland and Liechtenstein (eq+)
evid range:	1100-1142
reference paper:	refid: 239
	author: Kradolfer, U.
	title: RECENT SEISMICITY IN SWITZERLAND AS LOCATED BY THE SWISS NETWORK AND THE GERESS ARRAY
	year: 1992
	pub: presented at GERESS Symposium, Waldkirchen, Germany.

Dataset #6   .   Gestermann ....
description: subset of events from Ruhr University's database
number of events: 14
event type: earthquakes, quarry blasts and mining-induced tremors
                              eq(4), eq++(6), qb(1), qb+(1), qmt(2)
evid range: 1151-1169
reference paper: refid: 233
                              author: Gestermann, N., H.-P. Harjes, M. Jost,
                              J. Schweitzer, and J. Wuester
                              title: GERESS: MONITORING NATURAL AND ARTIFICIAL
                              SEISMICITY IN CENTRAL EUROPE '
                              year: 1992
                              pub: poster presented at 14th PL/ARPA Symposium, Tuscon, AZ.

Dataset #7   Ruhr Basin ....
number of events: 13
event type: mining-induced tremors (qmt)
evid: 1170-1184
reference paper: refid: 237
                              author: Joswig, M. and H. Schulte-Theis
                              title: MASTER-EVENT CORRELTATIONS OF WEAK LOCAL
                              EARTHQUAKES BY DYNAMIC WAVEFORM MATCHING
                              year: 1993
                              pub: Geophys. Journ. Int., vol 113

Dataset #8   Apatity Tremors ....
number of events: 10
event type: mining-induced tremors (qmt)
evid range: 2000-2014
reference paper: refid: 240
                              author: Kremenetskaya, E. O. and V. M. Trjapitsin, 1992.
                              title: INDUCED SEISMICITY IN THE KHIBINY
                              MASSIF (KOLA PENINSULA)
                              year: 1992
                              pub: in NORSAR Scientific Report 1-92/93

Dataset #9   Apatity Blasts- 3C ....
description: documented quarry blasts recorded after apatity 3C station
                              upgraded but before apatity array installed
number of events: 53
event type: quarry blasts with charge size (qb+)
evid range: 2015-2067
reference paper: refid: 241

author: Mykkeltveit, S.
title: MINING EXPLOSIONS IN THE KHIBINY MASSIF
(KOLA PENINSULA OF RUSSIA) RECORDED AT THE
APATITY THREE-COMPONENT STATION
pub: Norsar Scientific Report No. 14

Dataset #10   Apatity Blasts- Array ....
description: documented quarry blasts recorded after apatity array installed
number of events: 58
event type: quarry blasts with charge size (qb+), one tremor, (qmt)
evid range: 2070-2127
reference paper: refid: 244
                     author: Kvaerna, T.
                     title: INTELLIGENT POST-PROCESSING OF SEIMIC
                     EVENTS--PART 2
                     pub: NORSAR Scientific Report 2-92/93

Explosion Experiment in Tyrnyauz
August, 1993

M. Ya. Balbachan and M.B. Gokhberg

Experiment Objectives

Detecting and recording the mechanical-electric-magnetic phenomena (MEMP) that occurs within rocks as a result of destruction by an explosion are the main objectives of this experiment. At present, information on MEMP caused by explosions is very contradictory. There is no existing reliable data on the petrophysical conditions of origin, source and physical nature of MEMP. It was necessary to carry out this experiment for MEMP detection at different distances from a shot point in the attempt to obtain such data.

Pressure gradients and fractures occur in the rock volume simultaneously with an explosion generating seismic and probably electro-magnetic effects such as piezomagnetic, electrokinetic and so on. We used a set of new methods developed to study MEMP, to detect signals and to get information on the physical nature of the signals. Electro- and magnetotelluric measurements, near-surface electric measurements and seismic-acoustic observations were made simultaneously in real time over a frequency range of 1 to 1000 Hz.

The following conditions were fulfilled for massive quarry blasts of chemical explosions having yields of several tons to several tens of tons:

1 - source dimensions and energy release approximate crustal earthquakes with magnitudes of about 2.6 to 2.9;

2 - existence of shear component essential for destructive stress;

3 - simultaneous generation of fractures and rock crushing within the focus of the explosions;

4 - splitting of electric charges between rocks and gas-dust products of the explosion.

Electro-mechanical emission, electric relaxation due to fracture generation and friction, seismoelectric and piezomagnetic phenomena, displacement of a conducting body in the geomagnetic field, variations of conductivity, dielectric permeability and other rock properties are all possible sources of MEMP discussed in scientific literature. Separating electric charges between the rocks and the gas-dust cloud generates an additional interfering electromagnetic field. This kind of field, generated by surface explosions, was identified in this experiment by using specific data processing and was not observed as a result of underground explosions.

Short Review of Published Data on Electro-Magnetic Phenomena Generated by Explosions in Rocks

This is a short review of the electro-magnetic phenomena generated by explosions. Many authors have observed gas-dust venting generated by explosions, accompanied by electro-magnetic fields. According to V.N. Shuleikin, a gas-dust cloud usually has a positive electric charge and the rock has a negative one. This conclusion has been confirmed by results obtained in laboratories by other authors. Electric potentials, E, of approximately 10^5 V/m were observed within vented clouds generated by explosions. This confirms the possibility of recording E in air at distances varying from 250 to 500 m and measuring origin time with error 10^{-3} -10^{-4} sec. If we assume that the ratio of dielectric permeability in air (Ea) and in soil (Eg) is equal to the conductivity ratio for frequencies of several Hz, in other words is equal to 10^{-10}, we can ignore the influence of the electric field generated by the dust on measurements of potential differences in the soil. We used this conclusion for developing the experimental technique.

Electromagnetic pulses (EMP), which are not caused by discharges in the air, have been recorded by some authors earlier than the arrival of the seismic waves. V.N. Demin et al. (Sobolev, Demin et al., 1980)recorded EMP generated by underground explosions at polymetallic ore deposits within the frequency range of 0 to 10^7 Hz and greater. N.G. Khatiashvili and other researchers reported on EMP observations between 10^2 -10^5 Hz caused by the destruction of non-metalliferous rocks (Khatiashvili, 1989).

M.B. Gokhberg et al. published the results of MEMP observations during and after seismic wave propagation (Gokhberg et al., 1987). Sometimes it can be explained by sensor vibrations relative to stationary natural fields. Electric waves caused by seismic-electric phenomena will be generated simultaneously with seismic waves. According to Ya.M. Frenkel et al., a linear relationship should be observed between amplitudes of the electric and seismic waves. Electro-magnetic waves generated by Rayleigh waves (Gorbachev et al., 1987) or having non-harmonic waveforms and low frequency 1-10 Hz have also been observed. Results of observations of anomalies of quasistatic magnetic fields observed during 1-10 days after explosions were published (Oganesyan, 1986; Belekon, 1992; Balbachan, 1988). These anomalies can be generated by a residual piezomagnetic effect. Local variations of electroconductivity or collector properties of rocks can cause anomalies of the electric field after explosions (Adushkin et al., 1989).

This review shows that the results of the observations of electromagnetic effects of explosions are contradictory and unreliable. New experiments aimed at collecting data on explosion parameters, on electromagnetic signals generated by the explosions and recorded at different distances, and on characteristics of rocks are essential to resolve these discrepancies.

The Experiment Conditions

The following scientists participated in the experiment: M.Ya. Balbachan, senior scientist, was in charge of the observation technique, management and operation of seismic and electrometric sensors; S.M. Krylov, leading scientist, was in charge of the operation of magnetometers; and I.B. Matveev, senior scientist, was in charge of the recording equipment.

The experiment took place from 19 to 31 August 1993 at a high-altitude open pit of the Tyrnyauz tungsten-molybdenum integrated plant near the Tyrnauz settlement. Managers and employees of the integrated plant kindly helped us to fulfil the experiment. Between 22 and 29 August two explosions were detonated. One of them was an underground explosion and the second was a surface explosion. The underground explosion was detonated in a mine immediately beneath the quarry at 9:00 a.m. Moscow time and the surface explosion was detonated in the upper part of the quarry in overburden rocks at 10:00 a.m. Moscow time. Recording stations were located near a mountain top at heights of 2655-2665 m above sea level. At the observation area there was fog following rain and a light southerly wind during the first explosion. The weather was dry and fine during the second explosion.

This experiment was completed within a rock massif consisting of marble, limestone and garnet-pyroxenite with molybdenite, and biotite, pyroxene, and plagioclase with quartz hornfels. Small druses of galena crystals were observed on marble surfaces within the area of measurements. Rough estimates of the electric conductivity in the near-surface layer within the observation area, based on short-base measurements, yielded 10^{-2} Sm and 10^{-4} Sm for humid and dry weather, respectively. The content of ferromagnetics in the rock is very small, and iron oxides are present in the form of limonite (Chief geologist pers. com.). The rock massif should be paramagnetic in general. Rock density is 2.87 g/cm^3 on average.

Both explosions were detonated on Sunday when normal work at the underground and surface pits was not performed. All power sources in the mine and pit were switched off during the explosion recordings. The closest point where electric power was not switched off was the pit office building located at a distance of approximately one km. A cable ore-conveyor was disconnected during the explosions. The top station of the cable conveyor is located near the pit office building. There were no unambiguous signs of technical noise in the specific recordings made to study noise.

An underground explosion was detonated on August 22 at three point; simultaneously within levels between 2150 m and 2410 m above sea level. The smallest distance of the shot point from a recording station was approximately 450 m. The general yield of the explosion was greater than 10 tons. Because of technical reasons, this explosion was not recorded.

A surface explosion was also detonated on August 22 at one point for stripping. Explosive charges of 350 kg of grammonite were detonated in drilled holes in two hori-

zons at 2665 m and 2655 m above sea level, and at depths of approximately 10 m. Drilled holes were located in 11 rows. The distance between the rows and the drill holes within the rows was 3 m. Drilled holes in each row were detonated simultaneously, and between the rows there was a 20 msec delay. The total explosion time was 240 msec and the total yield was approximately 32 tons. The total volume of rocks extracted was 13000-15000 m^3 and the destruction zone volume was 35x15x10 m + 39x10X10 m. The total area of fractures generated by the explosion is estimated at approximately 10,000 - 100,000 m^2. The distance from the shot point to the recording station was 350 m.

An underground explosion was detonated at a depth of 100 m from the surface on August 29 at a point located at 2302 m above sea level. The distance between the shot point and the recording stations varied from 600 m to 650 m. The yield of the explosion was 5.8 tons. The total volume of rocks extracted was 3,000 m^3, and the total area of fractures generated by the explosion was approximately 2,000-20,000 m^2. The recording stations were located along a line at 2665 m. This line was approximately normal to a line connecting the shot point and the first (northern) recording station.

The surface explosion detonated on August 29 was located at 2675 m. The charges were distributed similarly to the explosion detonated on August 22 and the yield was 7.3 tons. The total explosion time was 100 msec. Destruction zone volume was approximately 20x15x10 m. Total volume of rocks extracted was 3,000 m^3. The total area of fractures generated by the explosion was approximately 2,000-20,000 m^2. The distance between the shot point and the first recording station was 250 m. The shot points were located at the same points as the underground explosion and at the same radius to the south from the shot point at 2665 m.

The objectives of these field observations were to check the sensitivity, the current level of the recording system, and the existence of electrical and magnetic effects generated by destruction of the rock by the explosions. The electric and magnetic signals can be recorded earlier, simultaneously and later than seismic signals. The study of the space attenuation of the anticipated electric and magnetic signals was another aim of this experiment.

Methods of Measurements and Parameters of Recording Equipment

The recording stations were located along the radius from the center of the surface explosions. The distance between the points of the recordings for the explosion on August 29 was 100 m and the distances between the shot point and the recording stations varied from 250m to 550 m (Figure 36 top). The only recording station for the explosion on August 22 was located at a distance of 350 m from the center of the surface explosion. One-component-electric and one-component-magnetic fields were measured in the air or in the soil.

Each recording station included a magnetometer designed by S.M. Krylov. The magnetometer was installed on August 22 horizontally and oriented towards the magnetic

pole. Three similar magnetometers were also installed for recording the August 29 explosion at points 1-3 and were oriented along a major geomagnetic vector. In both cases, horizontal projections of the magnetometer axis were oriented approximately along the radius towards the surface explosion centers and perpendicularly to the center of the underground explosions. Spherical capacitance antennas were installed 3m from the magnetometers at 1 m height above the Earth's surface to measure the vertical component of Ea and to measure the radial component of the horizontal Ea with help of two similar antennas.

Accelerometers were installed immediately beneath the antennas on solid hard rock. A 60° angle was produced in the vertical plane between the measuring axis of the magnetometers and a radius to the surface explosion. A measuring electrode was buried at a distance of 1 m from each accelerometer. These electrodes formed dipoles to measure the difference of potentials Ug at points 1, 2, 3 and 4 (Figure 36 bottom). Spherical antennas and measuring electrodes were connected with similar amplifiers having 3×10^6 Ohm input resistance. Signals from magnetometers, accelerometers and amplifiers at points 1 and 2 fed input of the blocks consisting of four channels. The blocks performed the frequency modulation of signals and generated a pilot signal to make a time scale and to eliminate errors caused by uncontrolled variations of recording velocity. Output signals from the magnetometer, the accelerometers and the amplifiers fed input to a TEAC XR-30C 8-channel magnetometer for point 3 and point 4. Sound accompaniment was recorded by channel 8.

An ultrashort-wave radio-synchronizer and radio-receivers that were connected to a tape-recorder were used to synchronize the recordings from different points. The synchronization pulse was recorded several seconds earlier than the surface explosion origin time. This pulse and the "pilot signal" provided rather accurate information on origin time. We assumed that we would be able to record a signal generated by the gas-dust venting with the help of the spherical antenna. Two 12-volt alkaline batteries were used as the power source for each point of the recording. Grounding was made for each point 3 m from the measuring electrodes using a similar electrode and increasing the NaCl concentration. All of the equipment was isolated from the Earth's surface.

Field observations: All elements of the recording system were installed several hours before the explosion. The noise was recorded during the 0.5-1.0 hour after the power and all of the equipment at the pit and the mine were cut off. The tape-recorders were turned on 5 min. before the time of the explosions and were turned off 15 min. later. Recording equipment was calibrated after the explosion recordings by signals generated as a result of 10 kg weight drops.

Equipment parameters:

1. Magnetometer. Signal-to-noise ratio for 1 Hz was greater than 7×10^5. The peak amplitude value of the output signal was ±8 V.

2. Spherical antenna. Capacitance with an unscreened connecting wire was 15 pF. The height above the Earth's surface was 1 m.

3. Accelerometer. The nominal conversion coefficient was 0.5 V sec^2/m. The maximal signal/noise ratio was not less than 106 dB. The peak amplitude value of the output signal was ±10 V. The output resistance was 2 kOhm.

4. The measuring electrodes were made from indium and had the shape of a cross. The electrode parameters were 100x100x100 mm.

5. Block consisting of two amplifiers. Input resistance was 3 MOhm. The coefficient of suppressing for 50 Hz signals was 10^4. These amplifiers were identical and independent. The maximal coefficient of the amplification was 65 Db. The maximal output signal was ±5 V. The maximal signal-to-noise ratio was not less than 5x10^6.

6. The differential preliminary amplifiers were included between the amplifiers mentioned above (see point 5, Figure 36 bottom) and the electrodes. Input resistance was 860 kOhm. The maximal output signal was ±10 V. The maximal signal-to-noise ratio was not less than 10^7.

7. Four-channel blocks. The dynamic range for the frequency modulation was 40 dB. The central frequency of the modulator was 7.5 kHz. The pilot signal frequency was 2.5 kHz. The maximal output signal was 5 V.

8. Magnetograph. The parallel recording of 8 channels to video-cassette was completed. The recording rates were 2.4 sm/sec and 4.8 sm/sec, respectively. Frequency modulation was used. The dynamic range was 45 dB. Frequency range varied from 0 to 625 kHz and from 0 to 1250 kHz for recording rates of 2.4 sm/sec and 4.8 sm/sec, respectively. Maximal output signal was 1 V.

9. Tape-recorders were used with two channel parallel recording to an audio-cassette. Dynamic range was 40 dB for frequency 7.5 kHz. Maximal input signal was 5 V.

10. Radio-synchronizer included a harmonic signal transmitter for a frequency of 100 MHz. Its power was 2.5 Wt. The synchronic pulse was generated by a sharp cut off.

These parameters of the recording equipment archived the following sensitivity of measurements: acceleration of seismic signals - 10^{-2} m/sec^2; magnetic field (magnetograph recordings) - Bi=2πT for frequency 1 Hz and Bi=2πT for frequency 16 Hz; the electric field in air for frequency 1 Hz Eαi=0.13 V/m for magnetograph recordings and 1.3 V/m for tape-recorder recording; electric field in air for frequency 1000 Hz: 1.3x10^{-6} V/m for magnetograph recording and 1.3x10^{-5} V/m for tape-recorder recording; for an electric field in a soil Eαi=2.5x10^{-8} V/m.

Noise Measurements

Noise was recorded continuously by the magnetographs during the two hours before, after and between the explosions detonated on August 29, 1993. The magnetograph has one order greater sensitivity in comparison with a tape-recorder and we used the

magnetograph recordings of noise for analysis. As we mentioned above, sources of noise generated by human activity were eliminated within a distance greater than 1 km from recording points. Dipoles at point 3 and point 4 had a 100 m base and were aligned from north to south. The similar component of the electric field in the soil, the signals from two spherical antennas, the two accelerometers and one magnetometer were recorded (point 3, Figure 36 bottom).

With accelerometers we were able to record the seismic signals generated by explosions, by the people near the recording points and by the fall of the stones after the explosions. With the exception of these moments, noise signals were manifested by the internal noise of the equipment. Signals recorded by other sensors were very complicated.

1. **High-frequency continuous signal.** This signal was recorded by all of the electromagnetic sensors. The dominant frequency of signals recorded with the help of the electrodes and antennas was approximately 300 Hz. Frequency spectra varied slowly with time, important variations happened during minutes or tens of minutes. The typical range of the amplitude variations was observed from 10^{-2} to 10^{-4} V/m and from 2.5×10^{-5} to 10^{-7} V/m for signals recorded with the help of the spherical antennas and electrodes, correspondingly. The general source of the signals located at distances larger than 100 m manifests by synchronism of signals recorded at different points and amplitude similarity. The signals recorded by electrodes have a 90^{0} phase shift in comparison with the signals recorded with the help of spherical antennas that fit a phase shift between the current of displacement and the current of conductivity.

2. **Harmonic low-frequency signal.** This signal was recorded by all of the electromagnetic sensors. The signals recorded by the magnetometer and electrodes immediately before the underground explosion detonated on August 29 had the dominant frequency of 0.2 Hz and amplitudes of 50 πT and 5×10^{-7} V/m, correspondingly. The signals recorded by spherical antennas had frequencies of 0.067 Hz and 1.0 Hz and amplitudes of 0.5 V/m and 0.1 V/m, correspondingly. The signals recorded by electrodes and magnetometers during 44 minutes before the surface explosion, had a frequency of 0.2 Hz and amplitudes of 100 πT and 5×10^{-8} V/m; meanwhile, signals from the spherical antennas had frequencies of 0.2 Hz and 0.7 Hz with corresponding amplitudes of 0.5 V/m and 0.2 V/m. Phase shift between signals from the electrodes and the antennas was approximately 60^{0}; that can be explained by the influence of a conductivity current in the air for the mentioned frequencies.

3. **"Steps" for the magnetometer recordings.** The steps had a positive and a negative polarity. Amplitude reduction with time was exponential with the relaxation period equal to approximately 7 sec. This is a typical value of internal relaxation period for the magnetometer. The amplitudes of the steps varied from 10 to 50 πT. The typical variations of the records from the electrodes and the antennas corresponded to the steps. Atmospheric signals that were greater than the noise level were observed on the average once per minute for the spherical antenna and the magnetometer recordings. Monochromatic harmonic 80 Hz signals were recorded by the magnetometers and were not recorded by

the accelerometers.

Explosion Effects

Electromagnetic signals before the seismic waves were not recorded for any of the three explosions within the dynamic range of observations. Anomalies were observed on spherical antenna recordings simultaneously with the venting of the gas-dust cloud for surface explosions (Figure 37). Arrows on this and other figures mark the origin time of explosions and the arrival time of seismic waves at recording points.

The following effects occurred during and after the propagation of seismic waves.

1). The seismic signal caused by the surface explosion detonated on August 29, 1993 had a waveform typical of multiple events with the second explosion delayed by 1.4 sec. The phase velocity calculated from the arrival time of the seismic signal measured at point 3 and point 4 was 4850 m/sec (Figure 38 and Figure 39). The seismic signal generated by the underground explosion detonated on August 29, 1993 is shown in Figure 40 and 41.

2). The magnetic field increased sharply during seismic wave propagation (Figures 42-45 and Figures 46-47). The relaxation time observed for these anomalies was approximately 7 sec. This time was influenced by the recording system and we can assume that real time was greater. The signal recorded by the magnetometer from the explosion detonated on August 22 had an essentially different waveform (Figure 48) in comparison with the explosion detonated on August 29 (Figure 42). That can be explained by different sensor orientation. The attenuation of the seismic wave amplitude was observed vs. distance. The results of calibration showed that the modulation of the signal recorded at point 3 from the explosion detonated of August 29 was caused by mechanical resonance of the sensor.

3). The results of calibration happened to be very interesting. The magnetometers manifested a step-shape increase of the magnetic field at different observation points similar to the explosion effect. A very specific effect, "memory" was observed during the calibration when the first blows only generated an observed phenomena characterizing a 12 sec relaxation period. The joint analysis of noise recordings and the results of the recording system tests yielded the information that the phenomena can not be explained by an influence of the recording equipment (Figures 49 and 50)

4). Amplitude decreasing of background signals were observed simultaneously with the previously described variations of the magnetic field measured by electrodes and spherical antennas. This phenomenon was observed up to the relaxation of the magnetic field signal (Figures 51-54 and Figures 55-58). It is worth noting that step-by-step pulses, B, having an amplitude equal to tens of πTs remained during the anomalies generated by the explosions. The origin time of the explosions detonated on August 28 coincide with the time arrivals of these pulses (Figures 46 and 47).

5). The decrease in the ratio Eg/Ea for the background signal of low frequency during the 44 minutes between explosions can be explained by the explosion influence.

Discussion of Results

Results of these experiments showed that within measurement errors, and for the frequency range 1-1000 Hz, electromagnetic signals generated by explosions and arriving earlier than seismic signals were not observed. This result corresponds to the source radius $r_0 \sim 15$ m, distance from the explosion center Ro = 350-650 m, the explosion magnitude, and rock composition. If we assume that the source is an electromagnetic dipole, that is the simplest pattern with the smallest attenuation of the field vs. distance, the electric field in the air above the source will be Eao = 0.5 Eai x. $(Ro/ro)^3 < 1800$ V/m for 1 Hz and 18 mV/m for 1 kHz, where Eai is the maximal sensitivity of measurements for underground explosions. The typical value of the electric field at the source, taking into account the size of the measuring dipole, is Ego = Egi $(Ro/ro)^3 < 9 \times 10^{-4}$ V/m.

Meanwhile, Bo = Bi $(Ro/ro)^2 < 1.8$ πT. Actually, local fields can have far larger values but attenuation fields vs. distance will be far larger. The absence of electromagnetic fields recorded earlier than seismic wave arrivals shows that the explosion source is not the source of MEMP with far greater specific power than rock samples destroyed in laboratories and generating usually smaller electromagnetic fields. Electromagnetic radiation can be recorded near the source only.

We believe that events observed during this experiment and recorded by electromagnetic sensors can be explained in terms of the temporary increase of mountain mass conductivity caused by seismic wave propagation. As result, the density of the telluric current and the secondary magnetic field will increase. On the other hand, Eg will be decreased and high-frequency signals will be screened. Amplitude modulation will follow this process. The sharp increase of mountain mass conductivity after the underground explosion detonated on August 29 is not strange.

The increasing of rock conductivity, probably caused by mechanical and chemical factors, was observed after vibrator performance (Volkova et al., 1988) and in laboratories when acoustic waves propagated through marble samples (Sadovskii et al., 1989). This phenomenon has not yet been explained from the point view of physics. Further investigations in this field will give us an additional chance for the remote study of seismic waves within the near zone from the source and the understanding of MEMP anomalies observed from earthquakes.

References

Adushkin, V.V. et al., *Izvestiya of the Academy of Sciences of the USSR, Physics of the Earth*, 3, p. 51, 1989. (in Russian)

Balbachan, M.Ya., *Proceedings of the Academy of Sciences of the USSR*, 303, 3, p. 579, 1988. (in Russian)

Belokon', V.I., *Geophysical Journal*, 14, 3, p. 75, 1992. (in Russian)

Frenkel', Ya.I., Collection of selected papers, v. 2, p. 520. (in Russian)

Gokhberg, M.B. et al.,*Proceedings of the Academy of Sciences of the USSR*, 295, 2, p. 321, 1987. (in Russian)

Gorbachev, L.P., Magnetic hydrodynamics, 2, p. 3, 1987. (in Russian)

Khatiashvili, N.G., *Earthquake prediction, 12, Dushanbe-Tbilisi*, p. 254, 1989. (in Russian)

Oganesyan, S.R., *Izvestiya of the Academy of Sciences of the Armyanskoi SSR, Earth Sciences*, 39, 4, p. 66, 1986. (in Russian)

Sadovskii, M.A. et al., *Proceedings of the Academy of Sciences of the USSR*, 309, 6, p. 1340, 1989. (in Russian)

Sobolev, G.A., V.M. Demin et al., *Proceedings of the Academy of Sciences of the USSR*, 252, 6, p. 1353, 1980. (in Russian)

Volkova, E.N. et al., *Proceedings of the Academy of Sciences of the USSR*, 302, 4, p. 816, 1988. (in Russian)
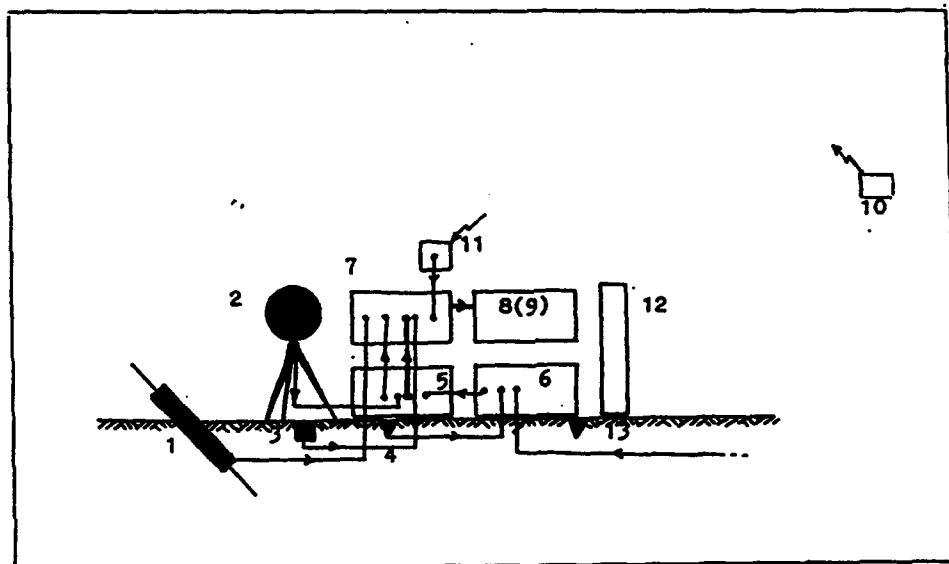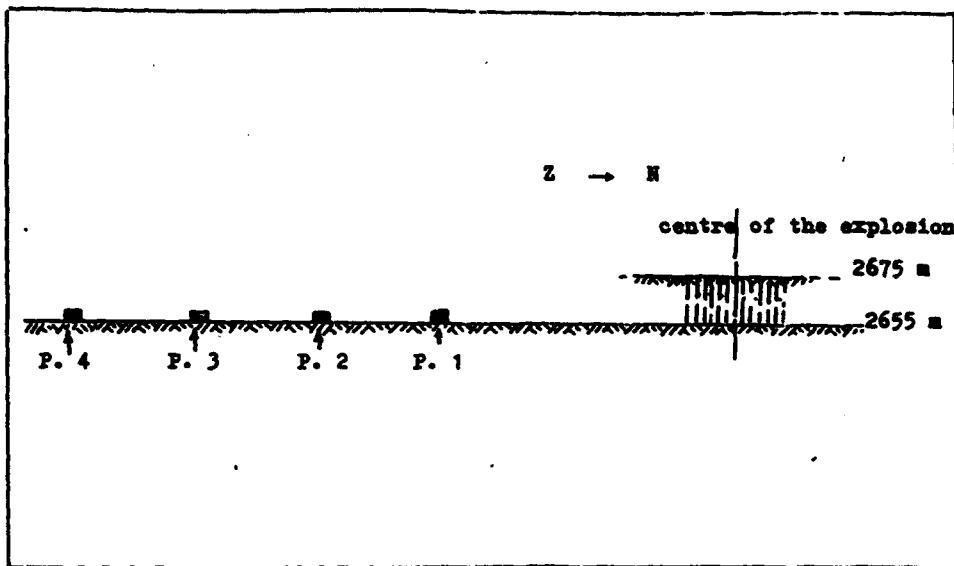
Figure 36: The experiment scheme performed on August 29, 1993.
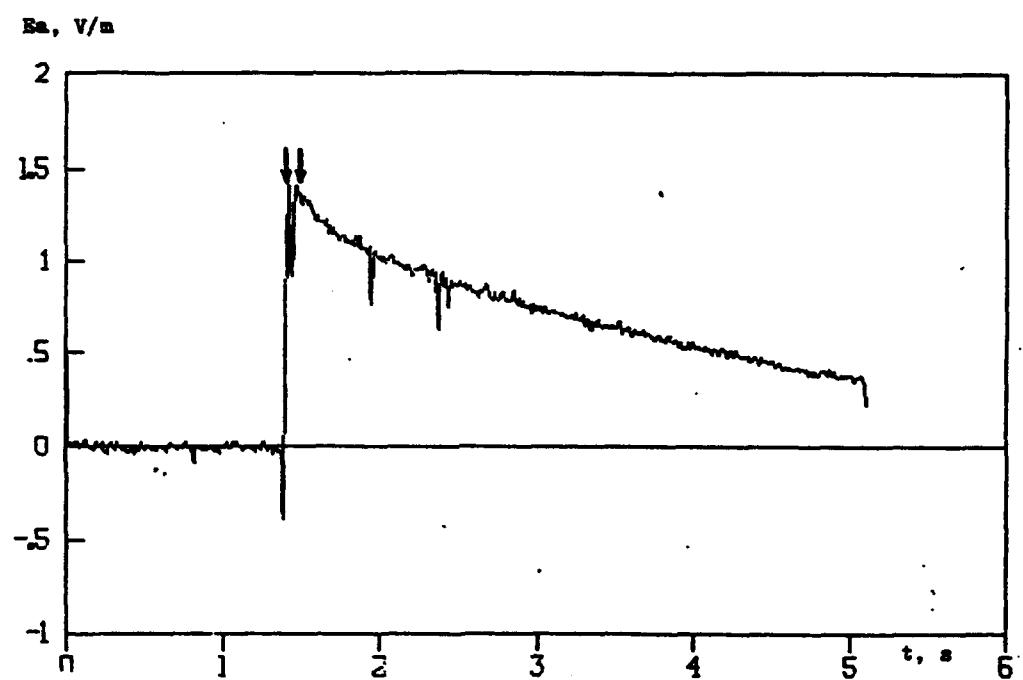
Figure 37: Surface explosion detonated on August 22, 1993, point No. 1 located at a distance of 350 m from the explosion center. Variations of the vertical component of the electric field in air Eα vs. time.

88
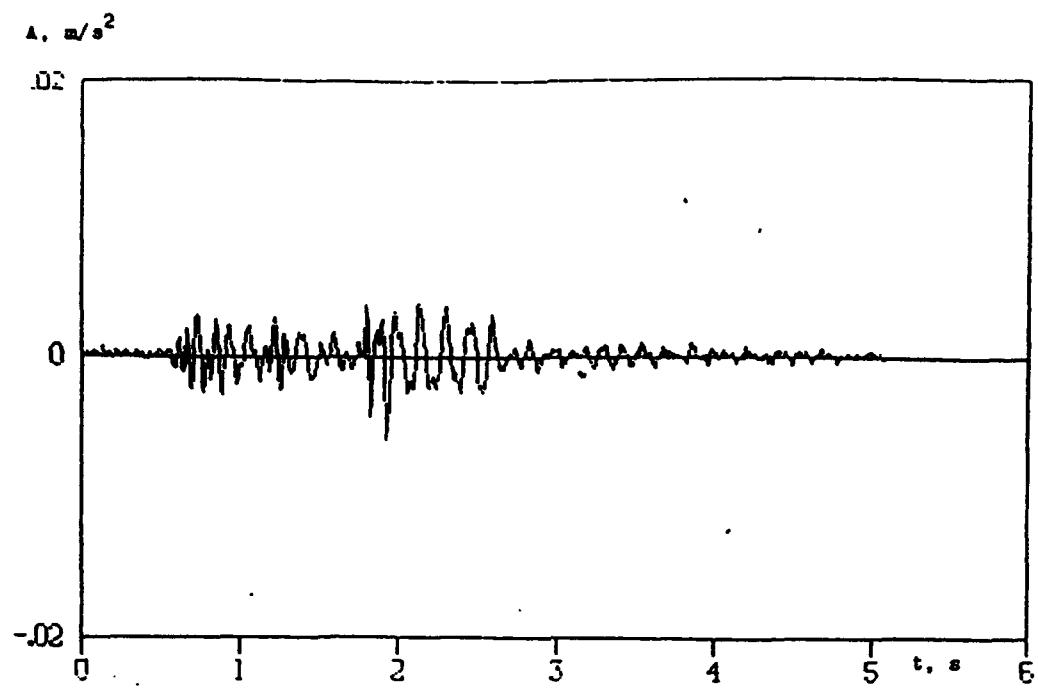
Figure 38: Surface explosion detonated on August 29, 1993; point No. 3. Variations of seismic wave acceleration vs. time.
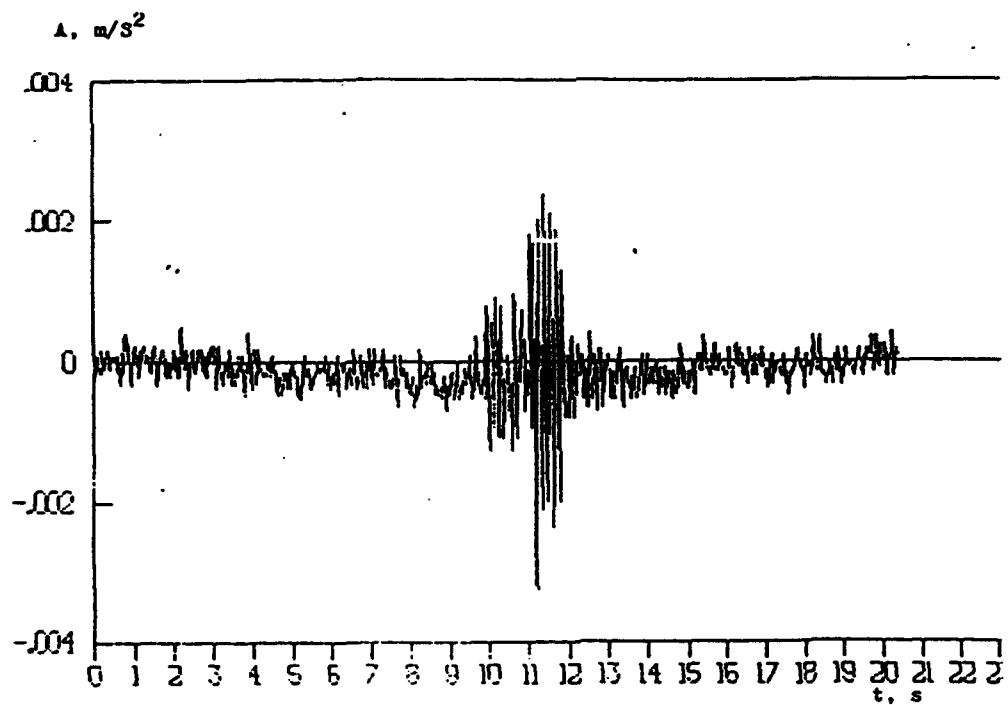
Figure 39: Surface explosion detonated on August 29, 1993; point No. 3. Variations of seismic wave acceleration vs. time. High frequency filter was used.
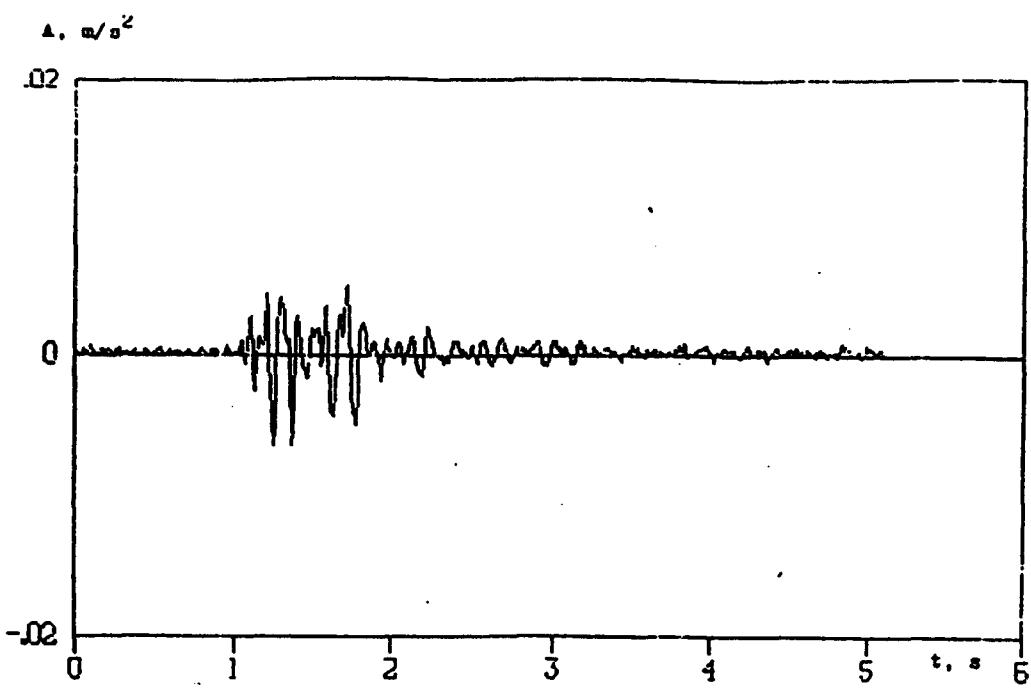
Figure 40:   Underground explosion detonated on August 29, 1993; point No. 3.
Variations of seismic wave acceleration vs. time.
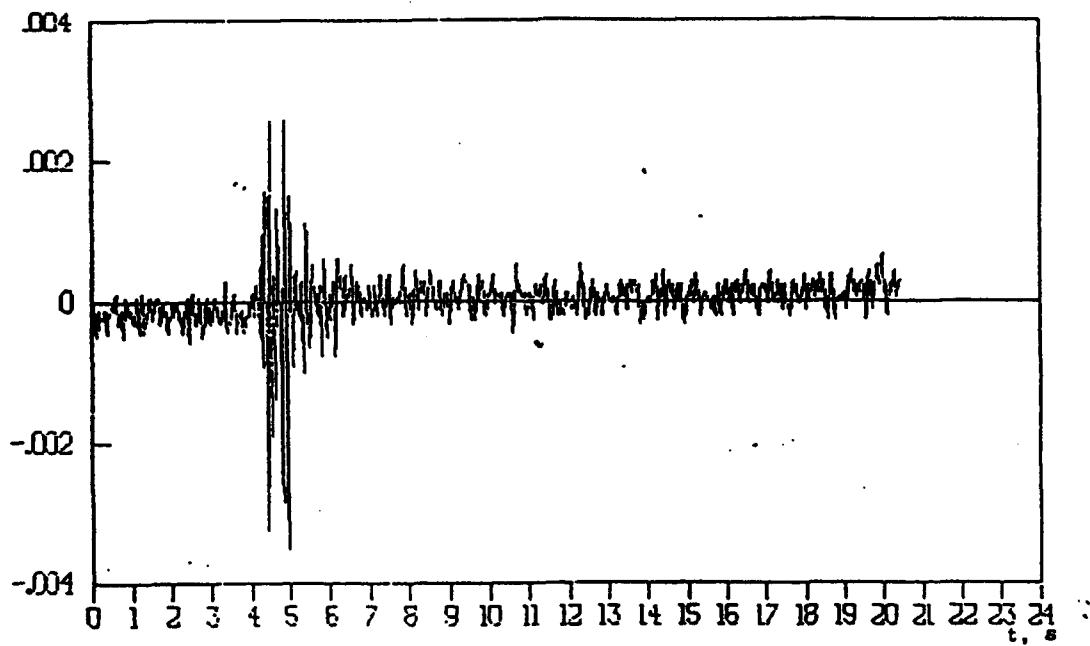
Figure 41:   Underground explosion detonated on August 29, 1993; point No. 3.
Variations of seismic wave acceleration vs. time. High frequency filter
was used.
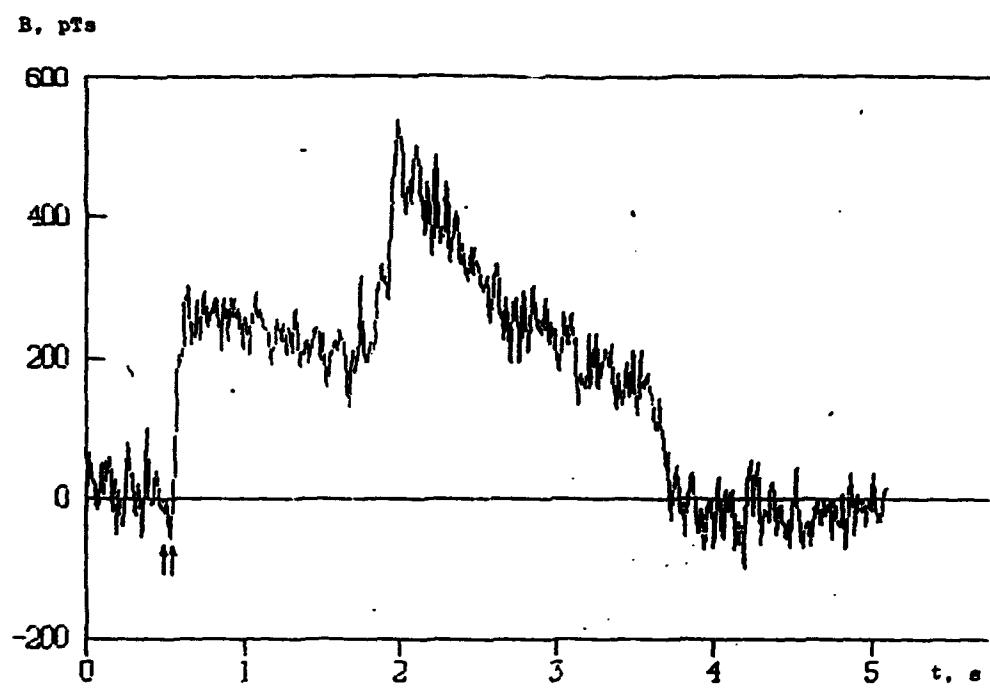
Figure 42: Surface explosion detonated on August 29, 1993; point No. 1 located at 250 m from the explosion center. Variations of the magnetic induction B vs. time.
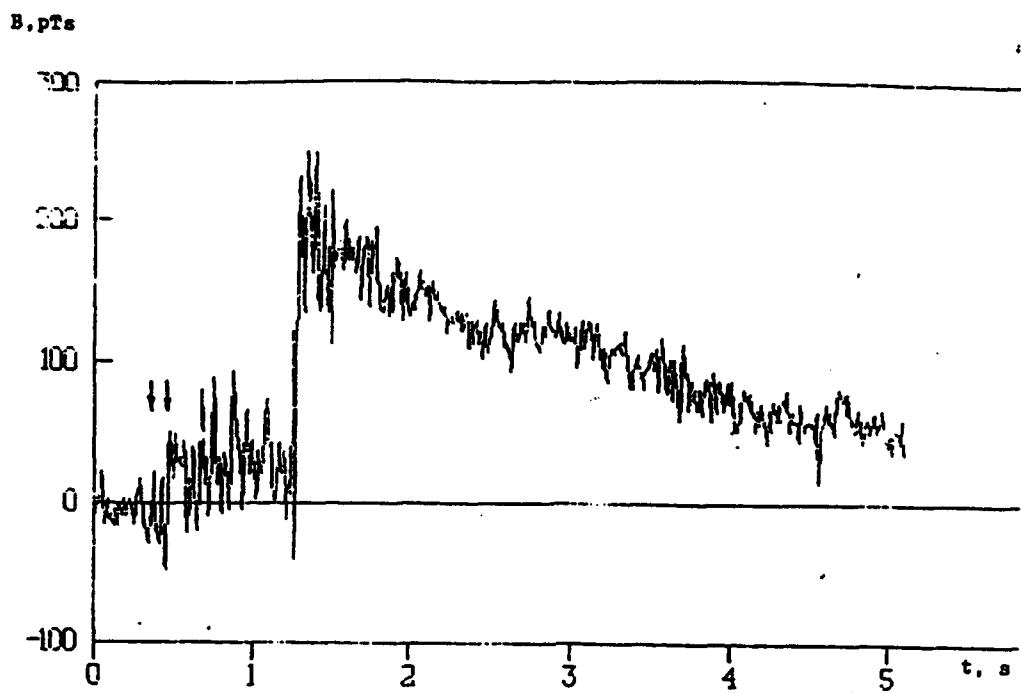
Figure 43: Surface explosion detonated on August 29, 1993; point No. 2 located at 350 m distance from the explosion center. Variations of the magnetic induction B vs. time.
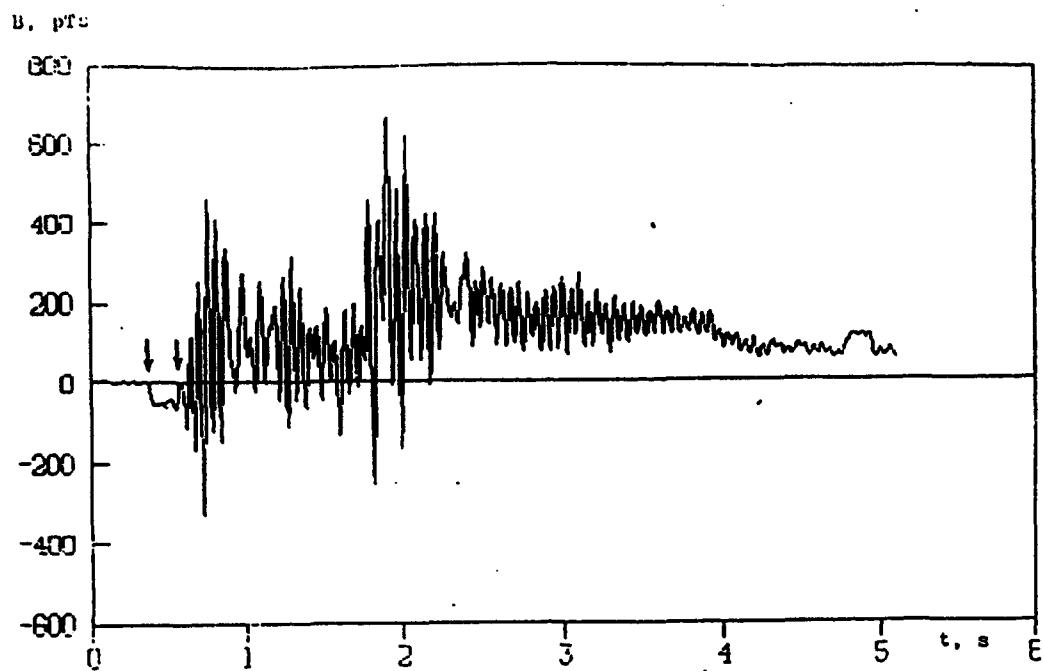
Figure 44:   Surface explosion detonated on August 29, 1993; point No. 3 located at
450 m distance from the explosion center. Variations of the magnetic
induction B vs. time.
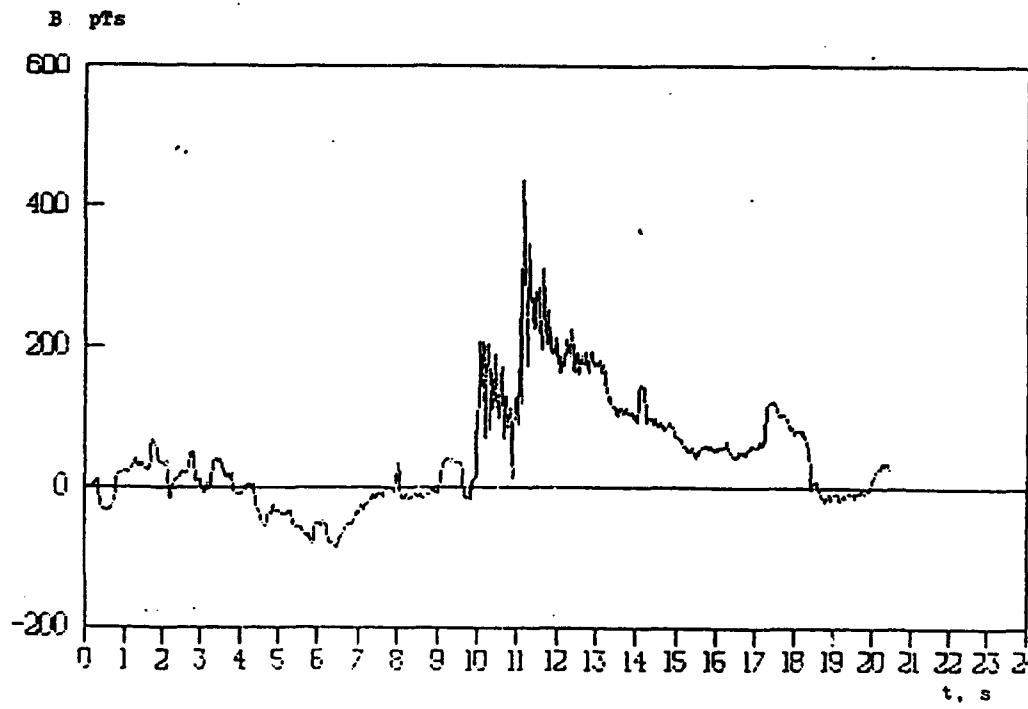
Figure 45:   Surface explosion detonated on August 29, 1993; point No. 3 located at
450 m distance from the explosion center. Variations of the magnetic
induction B vs. time. Low-frequency filter was used

93
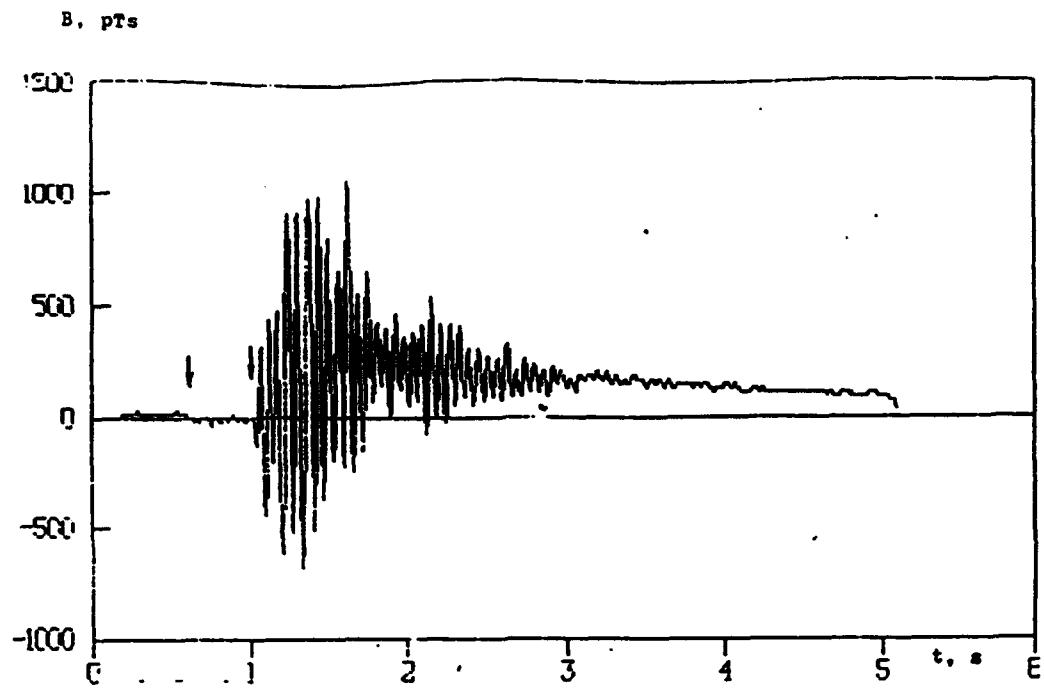
Figure 46: Underground explosion detonated on August 29, 1993; point No. 3 located at 650 m from the explosion center. Variations of the magnetic induction B vs. time.
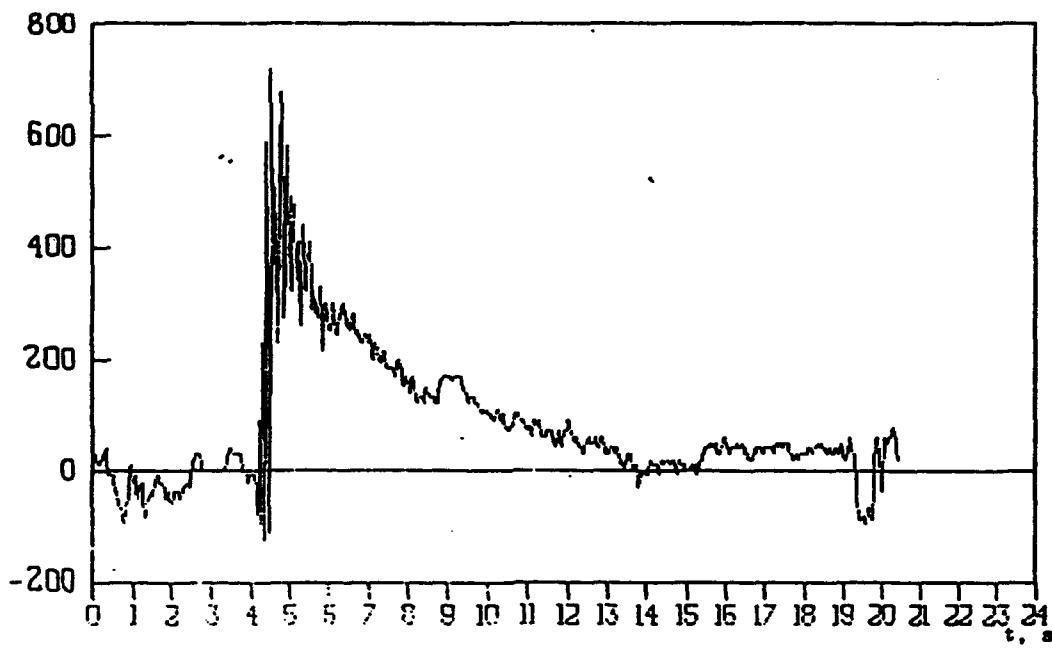
Figure 47: Underground explosion detonated on August 29, 1993; point No. 3 located at 650 m from the explosion center. Variations of the magnetic induction B vs. time. Low-frequency filter was used.
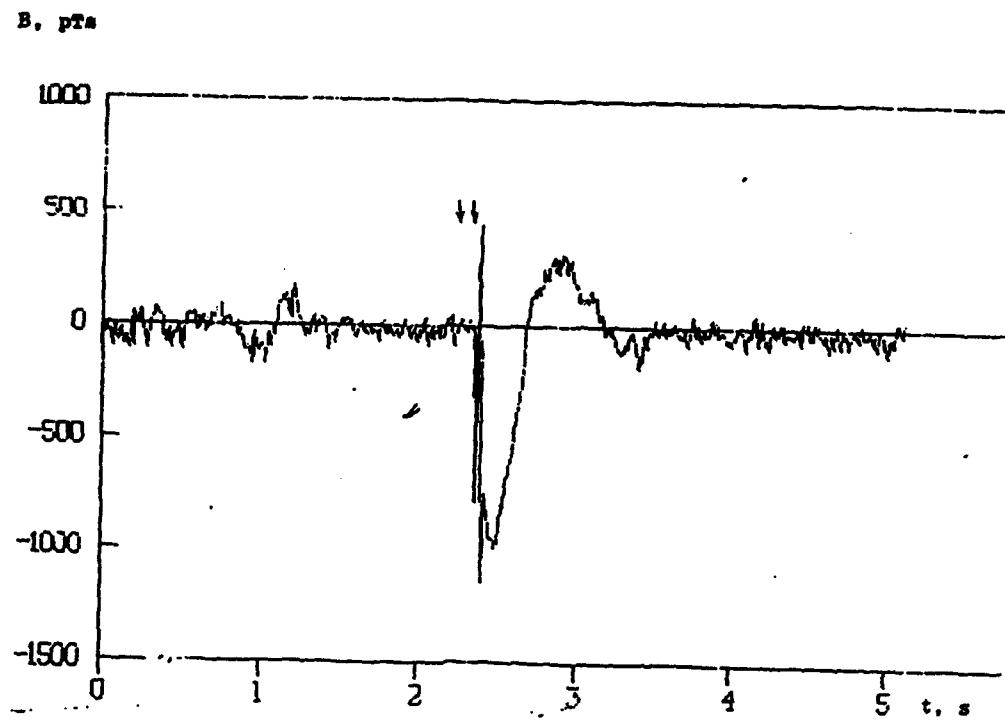
Figure 48: Surface explosion detonated on August 22, 1993, point No. 1. Variations of the radial component of the magnetic induction B vs. time.
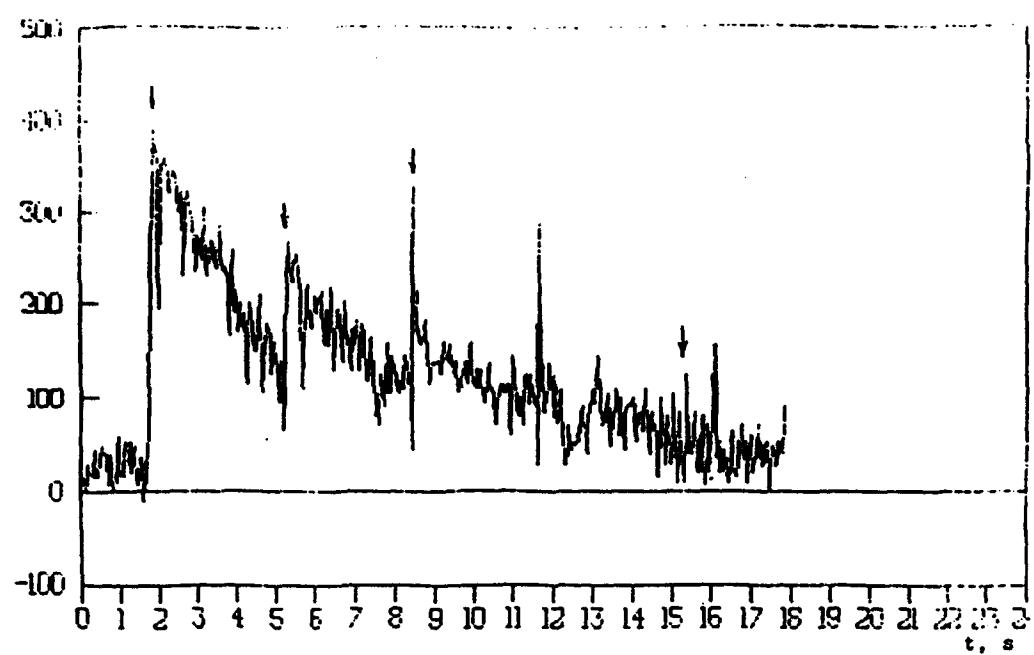
Figure 49: Calibrating signals recorded on August 29, 1993 at point No. 2. Variations of magnetic induction.
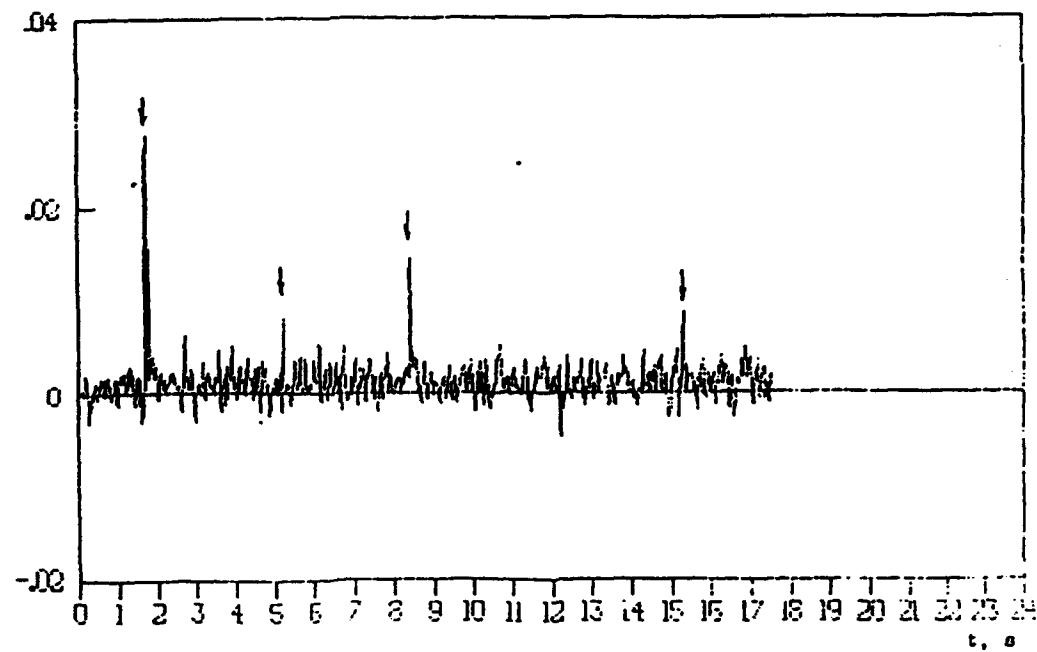
Figure 50: Calibrating signals recorded on August 29, 1993 at point No. 2. Variations of seismic wave acceleration.
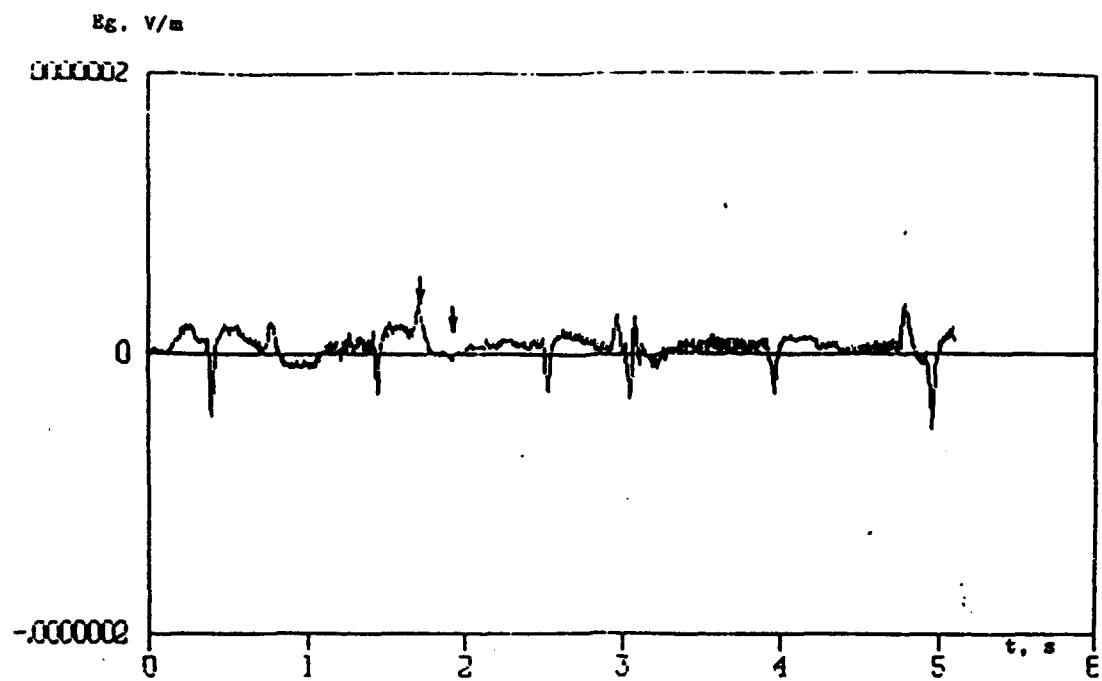
Figure 51: Surface explosion detonated on August 29, 1993; point No. 3. Variations of the radial component of the electric field in soil Eg vs. time.
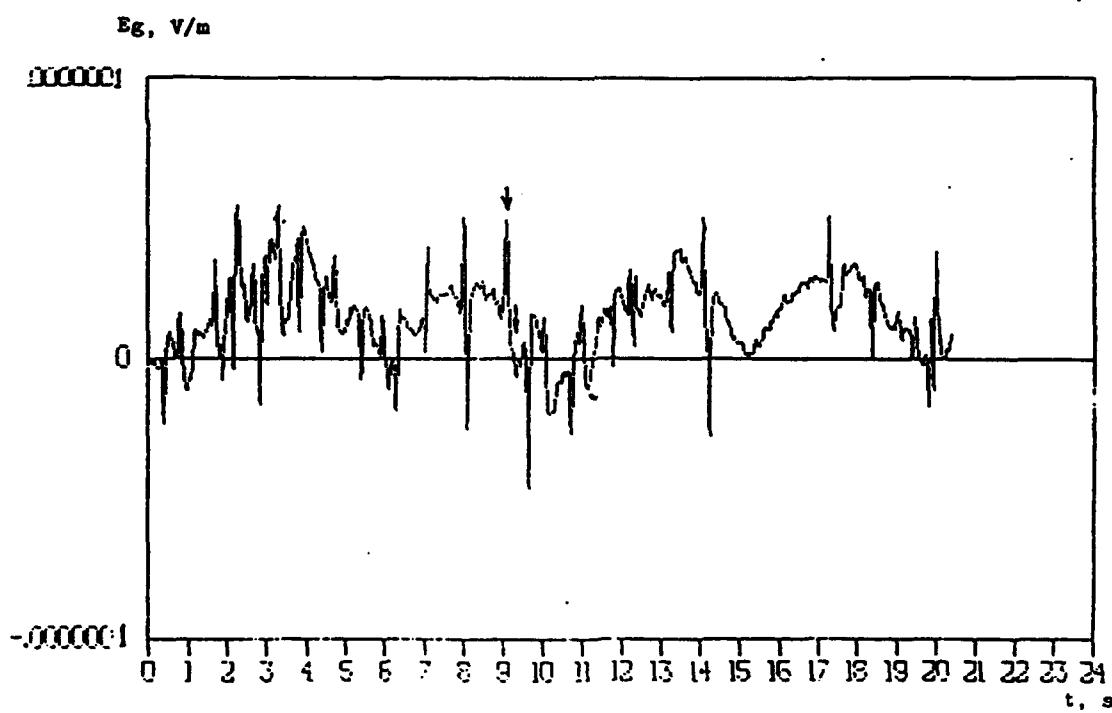
Figure 52: Surface explosion detonated on August 29, 1993; point No. 3. Variations of the radial component of the electric field in soil Eg vs. time. Low-frequency filter was used.
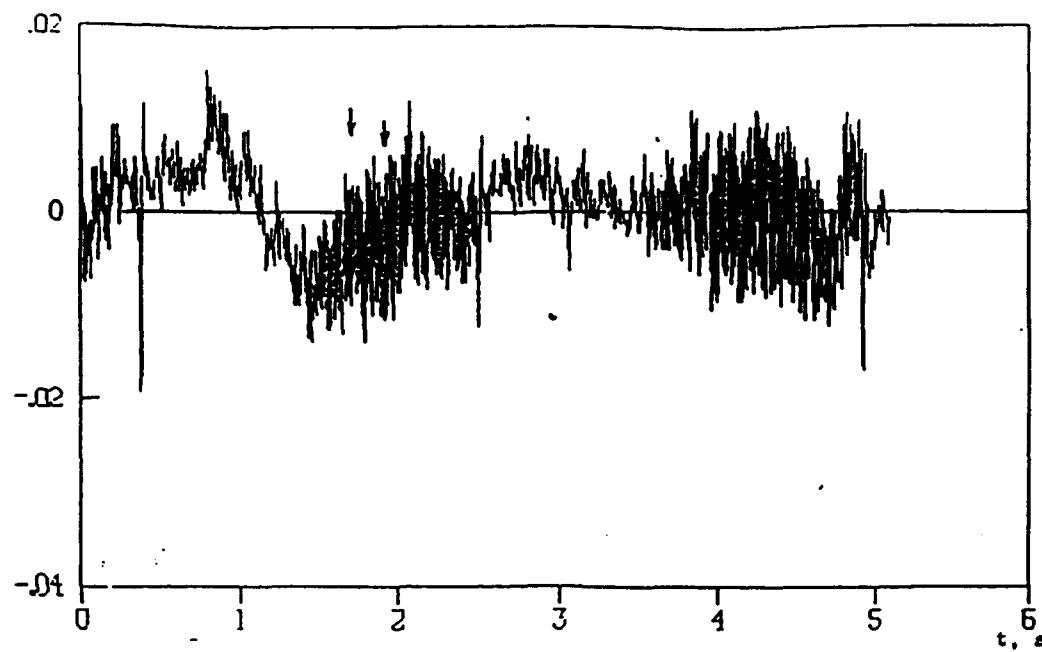
Figure 53:   Surface explosion detonated on August 29, 1993; point No. 3. Variations of the vertical component of the electric field in soil Eα vs. time.
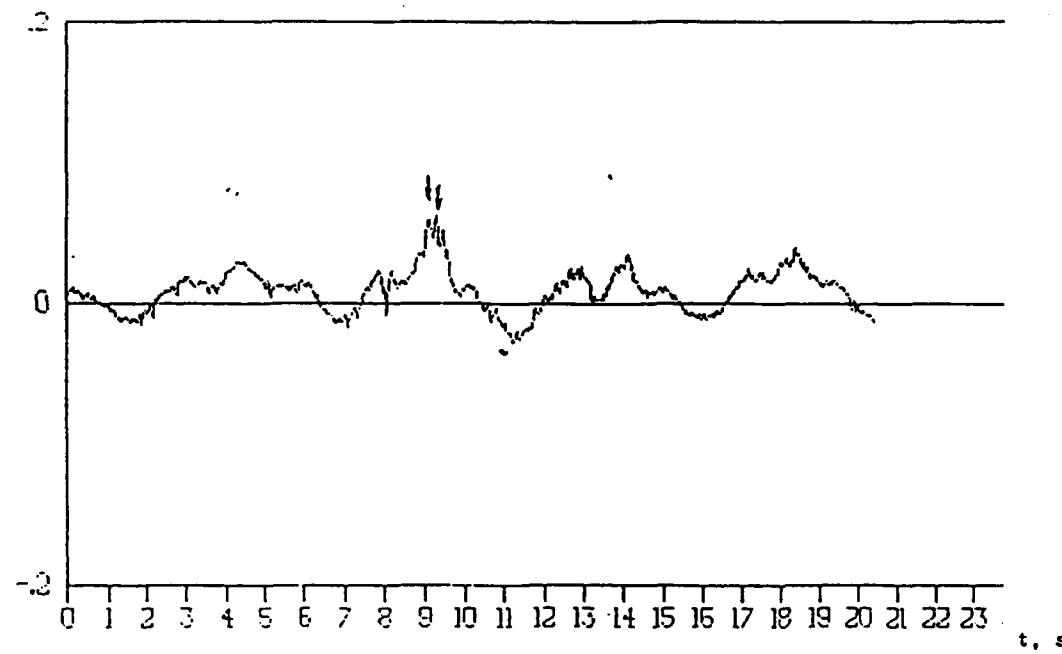
Figure 54:   Surface explosion detonated on August 29, 1993; point No. 3. Variations of the vertical component of the electric field in soil Eα vs. time. Low-frequency filter was used.

Eg, V/m
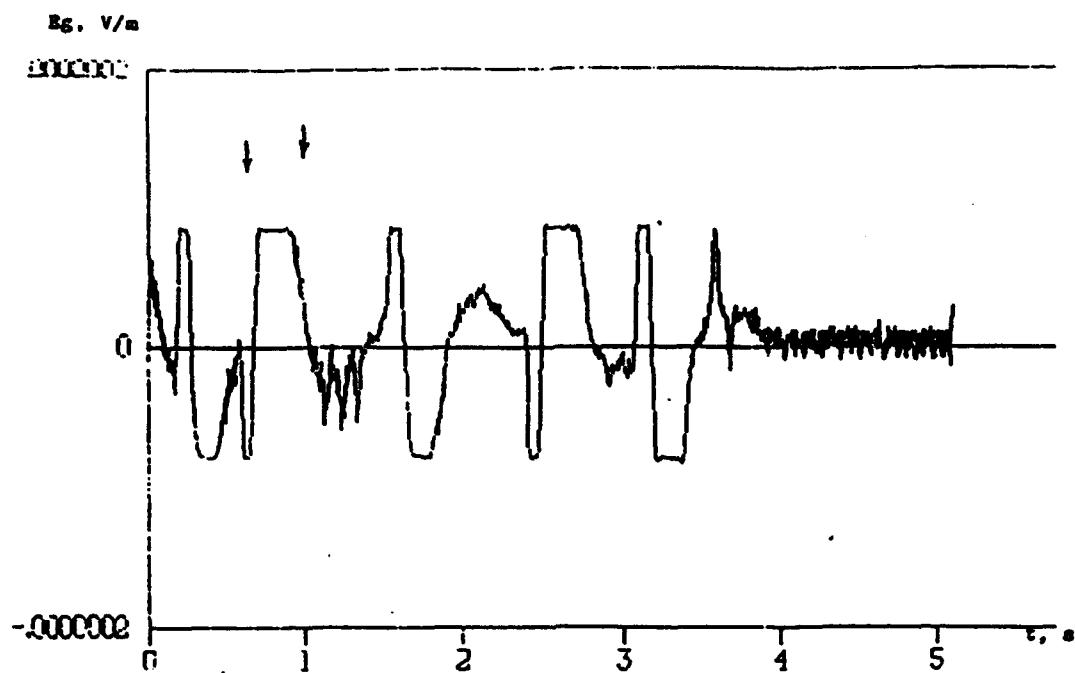
Figure 55: Underground explosion detonated on August 29, 1993; point No. 3. Variations of the radial component of the electric field in soil Eg vs. time.

Eg, V/m
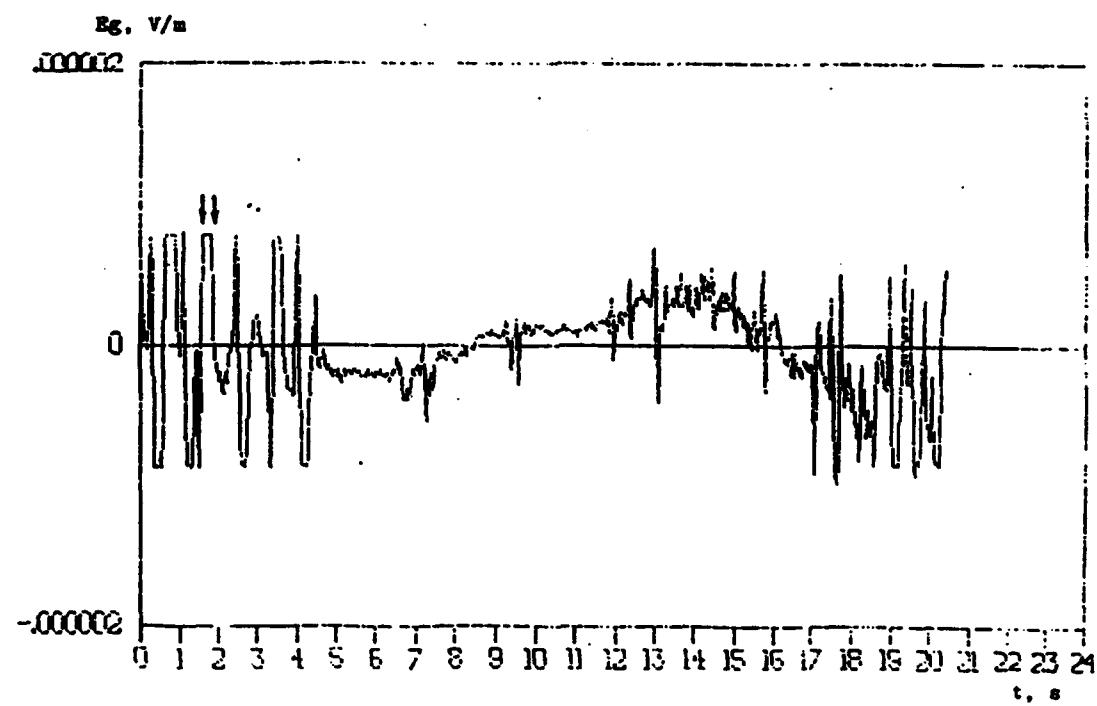
Figure 56: Underground explosion detonated on August 29, 1993; point No. 3. Variations of the radial component of the electric field in soil Eg vs. time. Low-frequency filter was used.

Ea, V/m
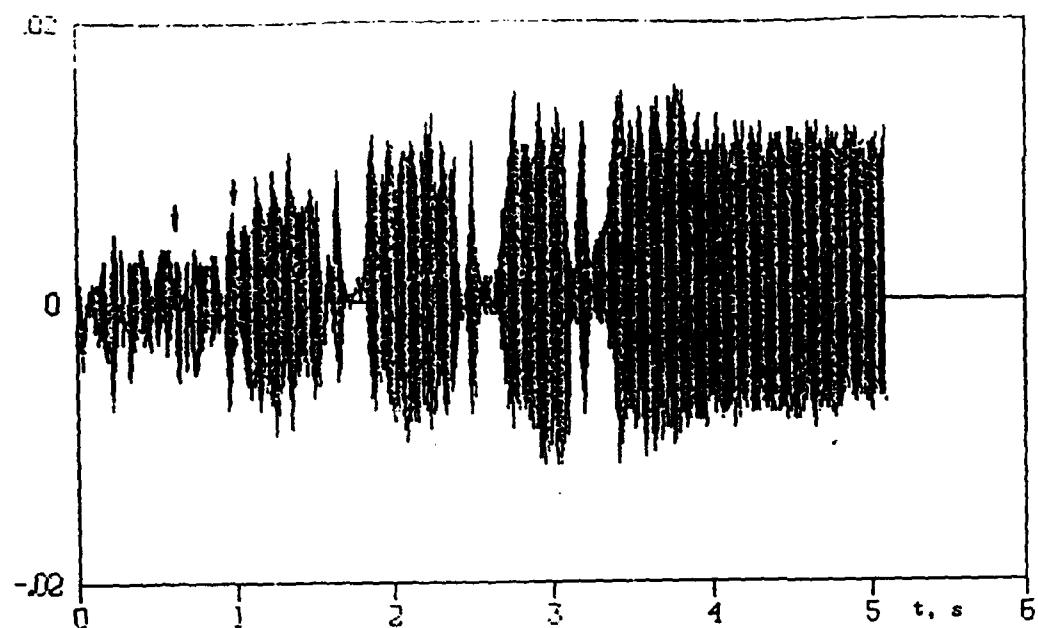
Figure 57:   Underground explosion detonated on August 29, 1993; point No. 3. Variations of the vertical component of the electric field in air vs. time Eα.
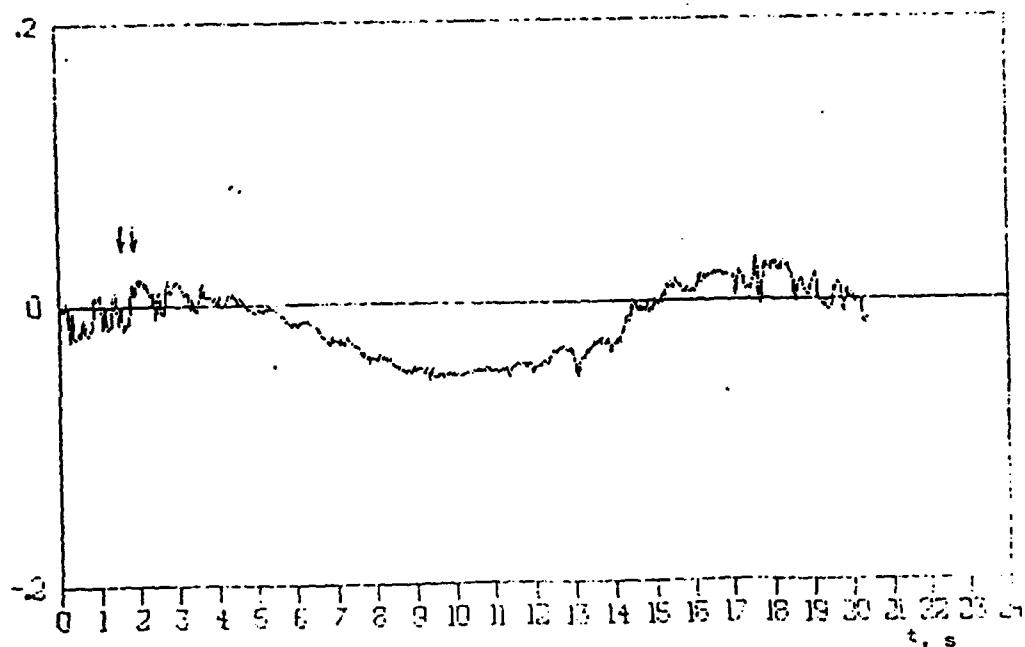

Figure 58:   Underground explosion detonated on August 29, 1993; point No. 3. Variations of the vertical component of the electric field in air vs. time Eα. Low-frequency filter was used.

100

Filming of the Ripple-Fired Explosion at the Tyrnyauz Industrial Complex

By V.I. Tsykanovskii

Institute for Dynamics of the Geospheres

Russian Academy of Sciences

Abstract

High speed filming of the ripple-fired explosion at the open quarry of the Tyrnyauz industrial complex (North Caucasus) has been carried out. Objectives of this project were to obtain information on the detonation of a sequence of charges in drilled holes, on real-time delays and other specific features of a set of chemical explosions.

Project description

According to the explosion plan, two sets of grammonite chemical charges of total weight 45 tons were to be detonated at the Tyrnyauz wolframite-molybdenum industrial complex. The charges were to be placed at two elevations, 2705 m and 2609 m. A general scheme of the benches where explosions were to be detonated and the locations of charges and the high-speed camera are shown at Figure 62. Figure 63 displays a map of the detonation site, cross-sections of the bench and the camera location.

Explosive charges located in 73 drilled holes were to be aligned in 5-6 rows and these charges were proposed to detonate within the upper bench at the 2705 m elevations (Figure 64). The charge in each borehole were to weigh approximately 350 kg, each borehole depth was 14 m, and the total weight of the charges was to be 30 tons. Explosive charges to be located in the 38 drilled holes were aligned in 4 rows and these charges were proposed to detonate within the lower bench at the 2690 m elevation. Each borehole depth and each borehole charge were to be similar to those on the upper bench. Total weight of the explosive charges on the lower bench was to be 15 tons (Figure 65). According to this project plan, the detonation time delay between neighboring rows was to be 20 msec.

The blasted block of rock consists of marble. There are no ore rocks within the block. This rock category is VI by explosion crushing standards and VII for drilling. The predicted distance for a maximum free flight was 300-400 m and the zone of seismic hazard was 60 m. The blast was planned to be detonated on August 22, 1933 at 6:00 a.m approximately, universal time (9:00 a.m., Moscow time).

1 proposed camera position

2 outsized blocks at the upper stage

3 upper stage charge 2705 m

4 outsized blocks at the lower stage

5 lower stage charge 2690 m

6 outsized block at the lower stage

outsized block at the upper stage **7**

⚔, chosen filming position

camera AKS-4

8
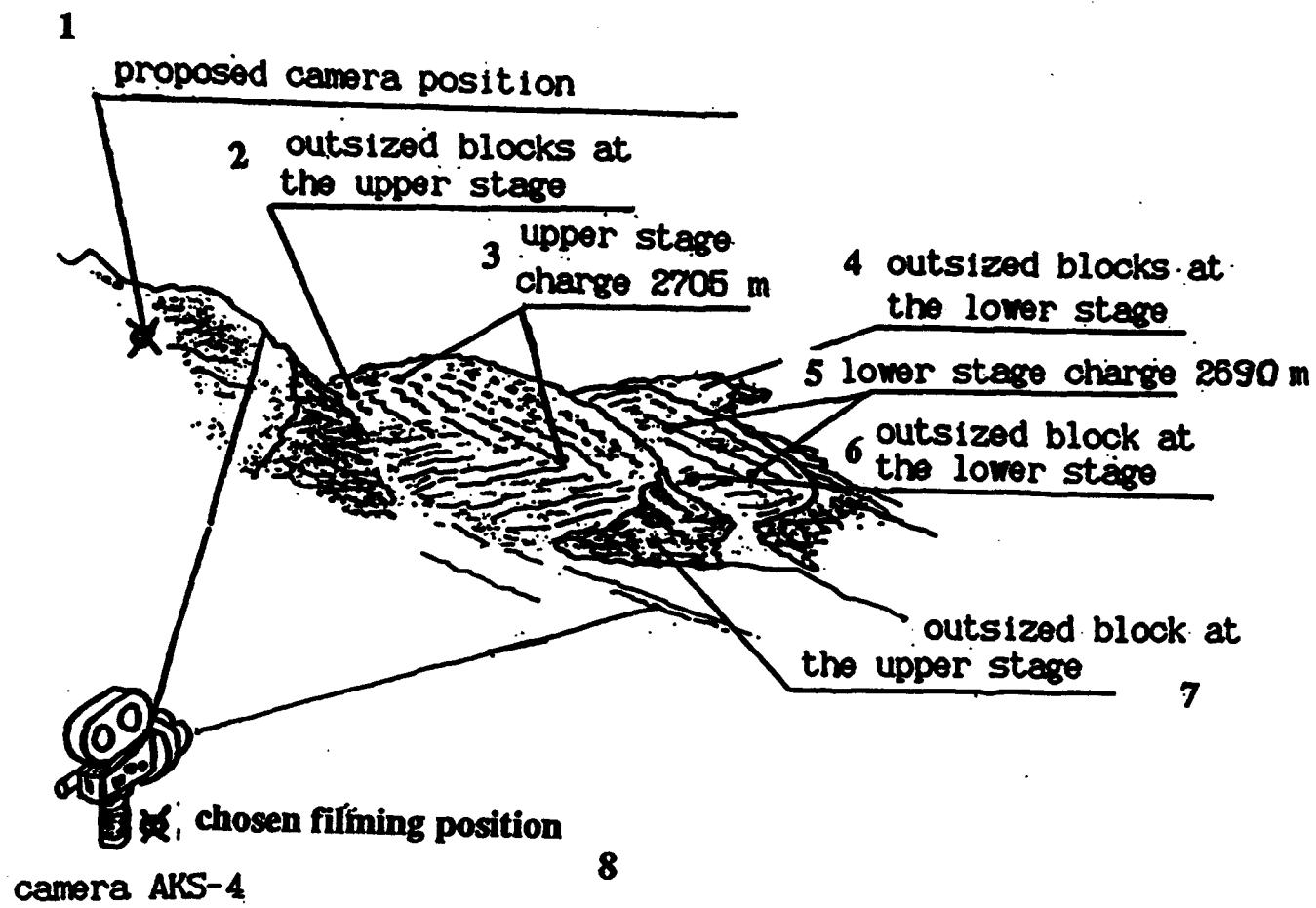
Figure 62: Scheme of the locations of the charges and camera. 1- suggested point for filming, 2 - oversized pieces of rocks on the upper bench, 3 - charge for the upper bench at 2705 m, 4 - oversized pieces rocks on the lower bench, 5 - charge for the lower bench at 2690 m, 6 - oversized pieces of rocks on the lower bench, 7 - oversized pieces of rock on the upper bench, 8 - selected point for filming.
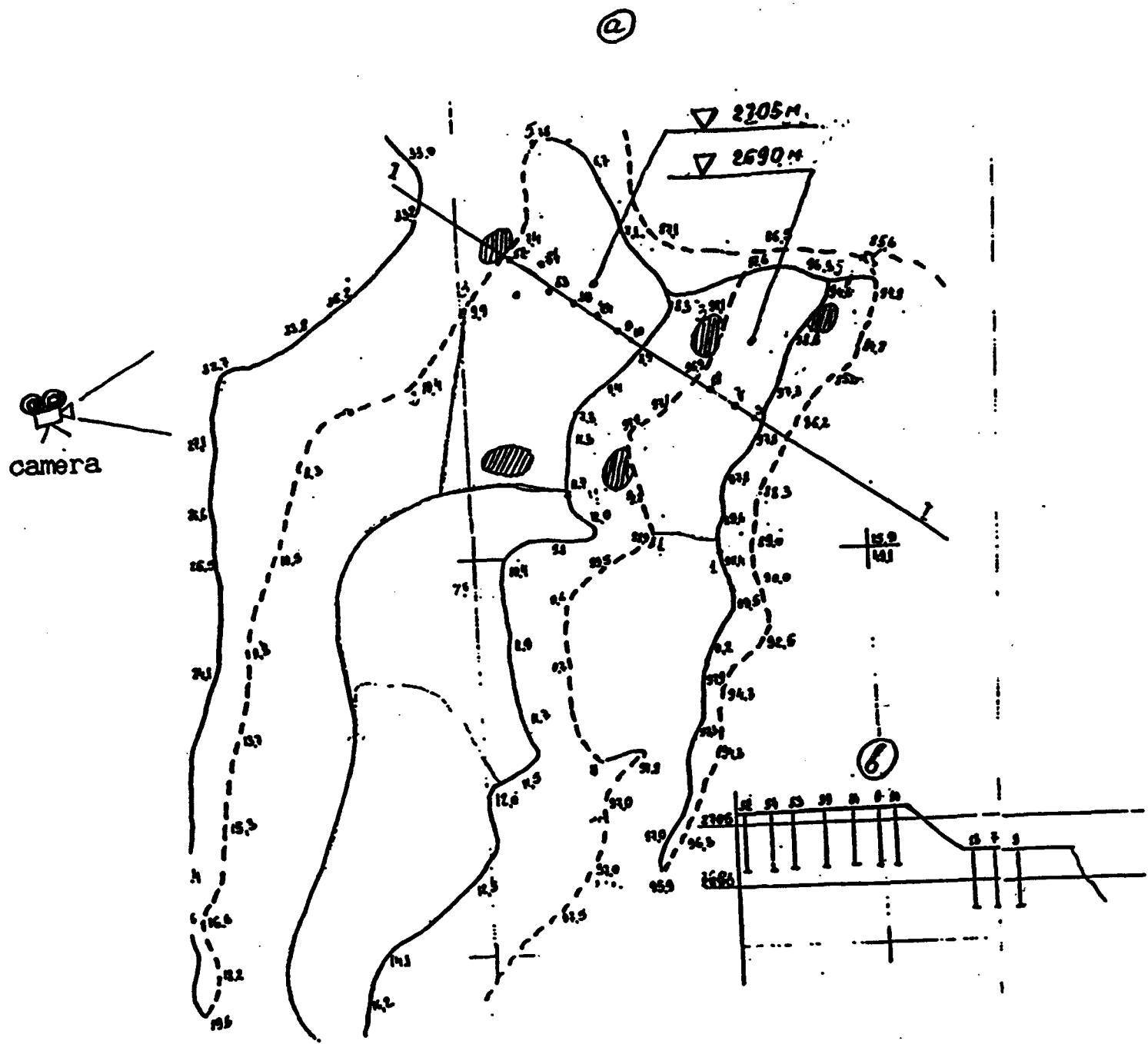
Figure 63: a). Location scheme of a chamber and the explosive charges on the upper and lower bench (shaded areas are the places where oversized pieces of rocks were blown up); b). Cross-section along I - I line.
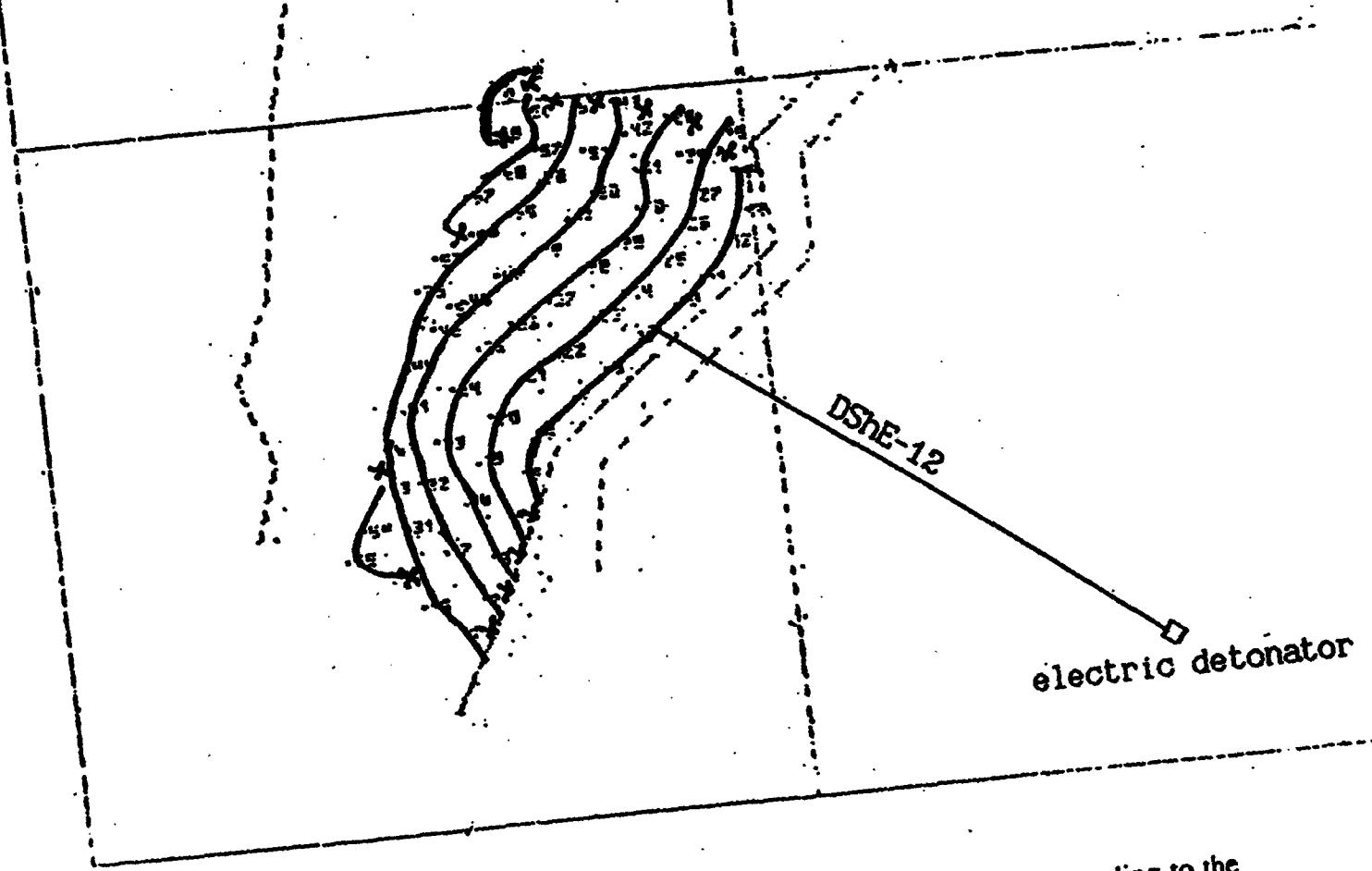
Figure 64: Scheme of the charge distribution for the upper bench, according to the project plan: 1 - DSHE-12 blasting cord, 2 - electric detonator.
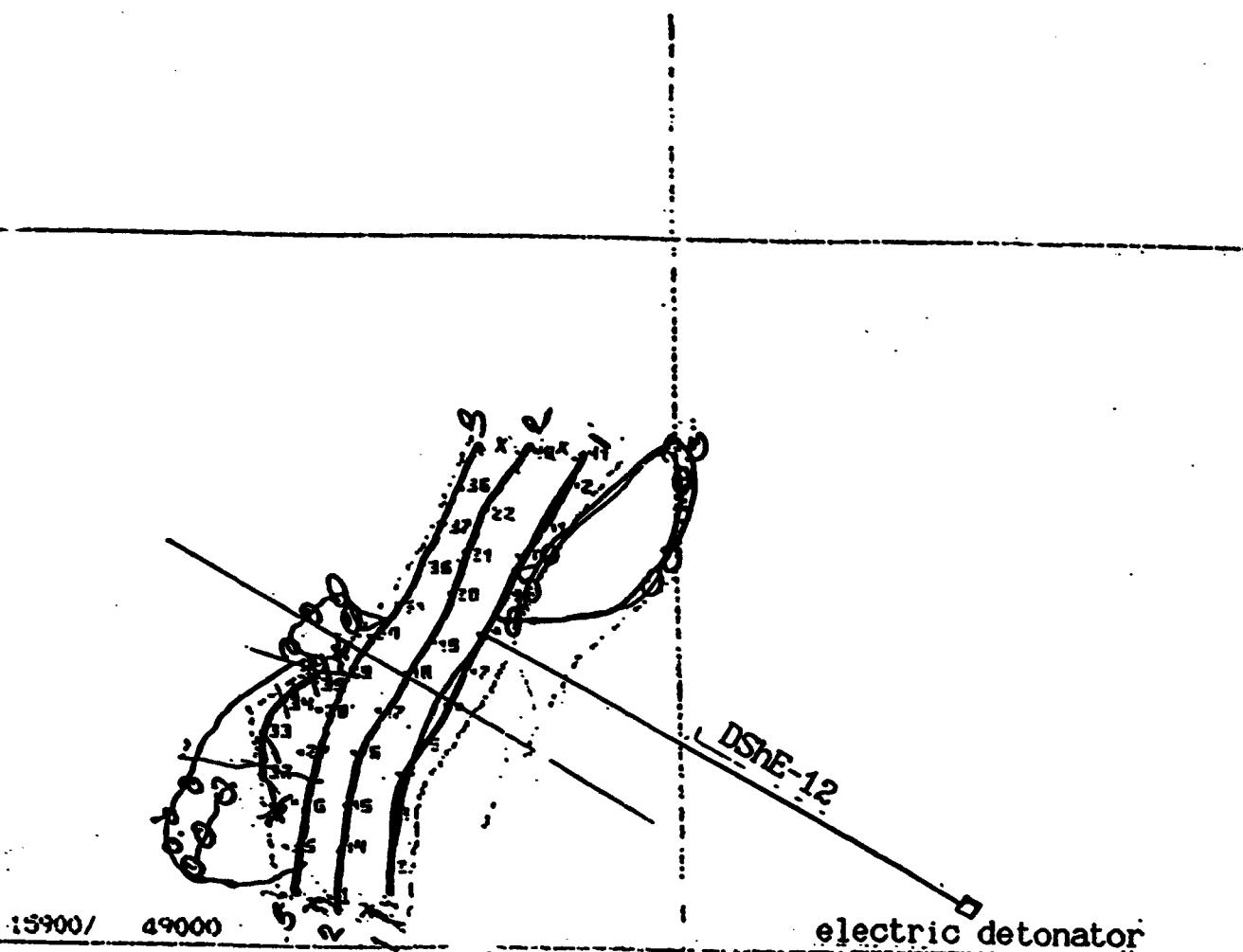
Figure 65: Scheme of the charge detonations on the lower bench, according to information obtained from men responsible for the explosion detonations: 1 - DSHE-12 blasting cord, 2 - electric detonator.

Blast conditions

Weather conditions during the experiment on August 22 were not favorable with fog and low clouds; the air temperature was approximately 4°C. It had been snowing during the night before the experiment. It took approximately 2 hours to prepare for the seismic measurements. A set of underground explosions were detonated on the same day before our experiment, at 9h 9m 39 s (Moscow time). According to the project plan, the total weight of detonated explosive charges was approximately 20 tons.

A position for the camera was selected only on the explosion day. The new position for the camera was chosen because the previously proposed position had to be rejected due to potential hazardous debris. The final camera position was chosen at 10 h 07 m Moscow time. The explosion was detonated at 10 h 27 m 25 sec (Moscow time). Thus, we had little time to install the camera and prepare for filming. The distance from the camera to the blast was approximately 350 m. Due to lack of time, the filming planned before the experiment was not conducted. The camera was placed on a tripod and was switched on by remote control through the timing and device control block. The camera was turned on 2 s before the explosion time.

After the experiment, we were told by men responsible for the explosion detonations that the project was changed during preparations of the charges within boreholes. The changes were mainly made on the upper bench where only 5 rows of boreholes were detonated (Figure 66).

Meanwhile, oversized pieces of rocks were also blown up on the upper and lower benches. Figure 62 shows the locations of the oversized rock pieces. The total weight of the detonated explosives was only 25 tons instead of the 45 tons mentioned in the project plan, and the time delays between the drilled hole rows was 40 msec instead of 25 msec allowed by the project plan. According to the specialists responsible for the explosion detonations, the increased time delay was caused by the large depth of the drilled holes. The blasting circuit was made by DSHE-12 blasting cord. The blasting cord was detonated by an electric detonator using a special blasting device.

As a result, we can assume that changes in the charges and detonation times were carried out arbitrarily, with the deviations from the project plan resulting from local production interests.

Measurement Results

Analysis of the developed film showed that the camera had a short break, approximately 120 msec, immediately after origin time. This break was probably caused by seismic vibrations generated by the explosion on the lower bench. For this reason, explosions detonated in the upper and lower benches were not filmed during the first 120 msec after the origin time. The distance from the camera to the explosions on the upper bench was
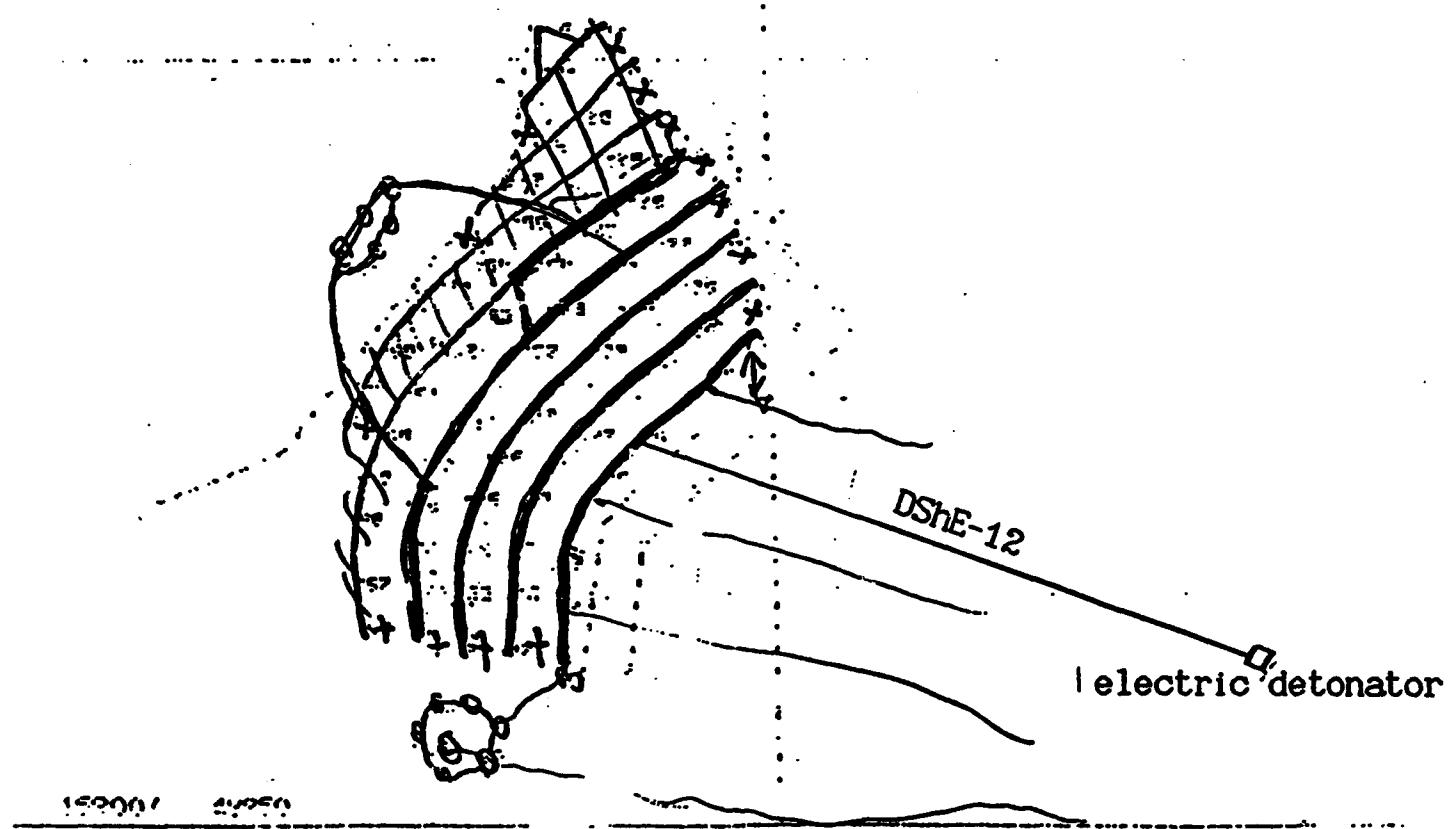
Figure 66: Scheme of the charge detonations on the upper bench, according to information obtained from men responsible for the explosion detonations (locations of detonated drill holes shown by the solid lines): 1 - DSHE-12 blasting cord, 2 - electric detonator.

approximately 350 m (geodetic measurements were not made). The camera focus was 35 mm and the filming speed was 70 exposure per second. The time between exposures was 14.2 sec and signals with a frequency of 50 Hz were used for time calibration. At the end of this report are photos of the explosion evolution. Time measurements shown on these photos were elapsed times after from the origin time of the explosion on the upper bench.

Analysis of the film shows detonations with chaotic and inaccurate time delays. This phenomenon is probably caused by variations in length of the blasting cord. We will consider the explosion evolution in detail.

One can see the evolution of explosions detonated within the first row of the upper bench on the photo at +30 msec. A white cloud, generated by blowing up the oversized pieces of rocks, obscures some of the nearest drill holes.

The photo made approximately 42 msec after the origin time shows explosions detonated within the second row of the drill holes. The following photos show the explosion evolution vs. time. The photos made at approximately 56 msec and 70 msec show the evolution of the explosion detonated within the second row of drill holes. Photos at 84 msec and 98 msec show the detonation of the explosions within the third row of the drill holes. At 112 msec the photo shows the evolution of the explosions detonated within the third and fourth rows of the drill holes and the beginning of the detonation of the oversized pieces of rocks. The photo at 126 msec shows the detonation within the fourth row, the explosion evolution for the oversized pieces of rock, and the beginning of the explosion detonation within the fifth row of the drill holes. At 140 msec the photo shows the whole blast evolution. The initial velocity of the cloud evolution is 400 m/s.

It is impossible to retrieve the actual scheme of blasting because the film analysis shows that the designed plan was not followed during the experiment. We can assume that the blasting plan was changed during the test in the row locations. Moreover, blasting of the oversized pieces of rock created additional difficulties for film analysis of the sequence of explosions in drill holes. The camera location should be chosen based on the exact blasting scheme and explosion features, in particular, for the oversized pieces of rocks.

Analysis of the film results showed that the camera should be attached to a firmer foundation such as a buried wooden bar. Two or three cameras filming from different directions and having a greater speed should be used to measure more accurately the time delays of the explosions.

The explosion improved visibility, probably because of fog condensation caused by the influence of the shock wave. An explosion detonated in a drill hole in the forth row was observed on the photo made at 84 msec after the origin time; this confirms our conclusion on the chaotic character of the blasting.

Conclusions

1. The explosion filming confirms the chaotic sequence of the detonations in the drill holes and deviations of the actual blasting scheme from the design plan.

2. The camera location should be chosen from the exact blasting scheme and the explosion features. Geodetic control of the camera location and exact measurements of the distance from the camera to the explosion are necessary for more accurate analysis of the explosion filming results.

3. Several cameras filming from different directions and having a greater speed should be used to measure the explosion time delays more accurately.

$t = 0$

$\sim +30\,ms$

$\sim +42\,ms$

110

~ + 56 ms

~ + 70 ms

~ + 84 ms

111

~ + 98 ms

~ + 112 ms

~ + 126 ms

$\sim + 140\,ms$

$\sim + 154\,ms$

$\sim + 168\,ms$

113

Explosion evolution

$t = 0$

$$t = 30 \text{ ms}$$

$t = 56$ ms

$t = 70$ ms

116

$t = 84\ m\varepsilon$

$t = 98\ ms$

$t = 112$ ms

$t = 126$ ms

$t = 140$ ms

$t = 154$ ms

Prof. Thomas Ahrens
Seismological Lab, 252-21
Division of Geological & Planetary Sciences
California Institute of Technology
Pasadena, CA 91125

Prof. Keiiti Aki
Center for Earth Sciences
University of Southern California
University Park
Los Angeles, CA 90089-0741

Prof. Shelton Alexander
Geosciences Department
403 Deike Building
The Pennsylvania State University
University Park, PA 16802

Prof. Charles B. Archambeau
CIRES
University of Colorado
Boulder, CO 80309

Dr. Thomas C. Bache, Jr.
Science Applications Int'l Corp.
10260 Campus Point Drive
San Diego, CA 92121 (2 copies)

Prof. Muawia Barazangi
Cornell University
Institute for the Study of the Continent
3126 SNEE Hall
Ithaca, NY 14853

Dr. Jeff Barker
Department of Geological Sciences
State University of New York
 at Binghamton
Vestal, NY 13901

Dr. Douglas R. Baumgardt
ENSCO, Inc
5400 Port Royal Road
Springfield, VA 22151-2388

Dr. Susan Beck
Department of Geosciences
Building #77
University of Arizona
Tuscon, AZ 85721

Dr. T.J. Bennett
S-CUBED
A Division of Maxwell Laboratories
11800 Sunrise Valley Drive, Suite 1212
Reston, VA 22091

Dr. Robert Blandford
AFTAC/TT, Center for Seismic Studies
1300 North 17th Street
Suite 1450
Arlington, VA 22209-2308

Dr. Stephen Bratt
ARPA/NMRO
3701 North Fairfax Drive
Arlington, VA 22203-1714

Dale Breding
U.S. Department of Energy
Recipient, IS-20, GA-033
Office of Arms Control
Washington, DC 20585

Mr Larry Burdick
2780 Ardmore Road
San Marino, CA 91108

Dr. Robert Burridge
Schlumberger-Doll Research Center
Old Quarry Road
Ridgefield, CT 06877

Dr. Jerry Carter
Center for Seismic Studies
1300 North 17th Street
Suite 1450
Arlington, VA 22209-2308

Dr. Martin Chapman
Department of Geological Sciences
Virginia Polytechnical Institute
21044 Derring Hall
Blacksburg, VA 24061

Mr Robert Cockerham
Arms Control & Disarmament Agency
320 21st Street North West
Room 5741
Washington, DC 20451,

Prof. Vernon F. Cormier
Department of Geology & Geophysics
U-45, Room 207
University of Connecticut
Storrs, CT 06268

Prof. Steven Day
Department of Geological Sciences
San Diego State University
San Diego, CA 92182

1

Dr. Zoltan Der
ENSCO, Inc.
5400 Port Royal Road
Springfield, VA 22151-2388

Prof. Adam Dziewonski
Hoffman Laboratory, Harvard University
Dept. of Earth Atmos. & Planetary Sciences
20 Oxford Street
Cambridge, MA 02138

Prof. John Ebel
Department of Geology & Geophysics
Boston College
Chestnut Hill, MA 02167

Eric Fielding
SNEE Hall
INSTOC
Cornell University
Ithaca, NY 14853

Dr. Petr Firbas
Institute of Physics of the Earth
Masaryk University Brno
Jecna 29a
612 46 Brno, Czech Republic

Dr. Mark D. Fisk
Mission Research Corporation
735 State Street
P.O. Drawer 719
Santa Barbara, CA 93102

Prof. Donald Forsyth
Department of Geological Sciences
brown University
Providence, RI 02912

Dr. Cliff Frolich
Institute of Geophysics
8701 North Mopac
Austin, TX 78759

Dr. Holly Given
IGPP, A-025
Scripps Institute of Oceanography
University of California, San Diego
La Jolla, CA 92093

Dr. Jeffrey W. Given
SAIC
10260 Campus Point Drive
San Diego, CA 92121

Dr. Dale Glover
Defense Intelligence Agency
ATTN: ODT-1B
Washington, DC 20301

Dan N. Hagedon
Pacific Northwest Laboratories
Battelle Boulevard
Richland, WA 99352

Dr. James Hannon
Lawrence Livermore National Laboratory
P.O. Box 808
L-205
Livermore, CA 94550

Prof. David G. Harkrider
Seismological Laboratory
Division of Geological & Planetary Sciences
California Institute of Technology
Pasadena, CA 91125

Prof. Danny Harvey
CIRES
University of Colorado
Boulder, CO 80309

Prof. Donald V. Helmberger
Seismological Laboratory
Division of Geological & Planetary Sciences
California Institute of Technology
Pasadena, CA 91125

Prof. Eugene Herrin
Institute for the Study of Earth and Man
Geophysical Laboratory
Southern Methodist University
Dallas, TX 75275

Prof. Robert B. Herrmann
Department of Earth & Atmospheric Sciences
St. Louis University
St. Louis, MO 63156

Prof. Lane R. Johnson
Seismographic Station
University of California
Berkeley, CA 94720

Prof. Thomas H Jordan
Department of Earth, Atmospheric &
   Planetary Sciences
Massachusetts Institute of Technology
Cambridge, MA 02139

Prof. Alan Kafka
Department of Geology & Geophysics
Boston College
Chestnut Hill, MA 02167

Robert C. Kemerait
ENSCO, Inc.
445 Pineda Court
Melbourne, FL 32940

Dr. Karl Koch
Institute for the Study of Earth and Man
Geophysical Laboratory
Southern Methodist University
Dallas, Tx 75275

U.S. Dept of Energy
Max Koontz, NN-20, GA-033
Office of Research and Develop.
1000 Independence Avenue
Washington, DC 20585

Dr. Richard LaCoss
MIT Lincoln Laboratory, M-200B
P.O. Box 73
Lexington, MA 02173-0073

Dr. Fred K. Lamb
University of Illinois at Urbana-Champaign
Department of Physics
1110 West Green Street
Urbana, IL 61801

Prof. Charles A. Langston
Geosciences Department
403 Deike Building
The Pennsylvania State University
University Park, PA 16802

Jim Lawson, Chief Geophysicist
Oklahoma Geological Survey
Oklahoma Geophysical Observatory
P.O. Box 8
Leonard, OK 74043-0008

Prof. Thorne Lay
Institute of Tectonics
Earth Science Board
University of California, Santa Cruz
Santa Cruz, CA 95064

Dr. William Leith
U S. Geological Survey
Mail Stop 928
Reston, VA 22092

Mr. James F. Lewkowicz
Phillips Laboratory/GPEH
29 Randolph Road
Hanscom AFB, MA 01731-3010(2 copies)

Mr. Alfred Lieberman
ACDA/VI-OA State Department Building
Room 5726
320-21st Street, NW
Washington, DC 20451

Prof. L. Timothy Long
School of Geophysical Sciences
Georgia Institute of Technology
Atlanta, GA 30332

Dr. Randolph Martin, III
New England Research, Inc.
76 Olcott Drive
White River Junction, VT 05001

Dr. Robert Masse
Denver Federal Building
Box 25046, Mail Stop 967
Denver, CO 80225

Dr. Gary McCartor
Department of Physics
Southern Methodist University
Dallas, TX 75275

Prof. Thomas V. McEvilly
Seismographic Station
University of California
Berkeley, CA 94720

Dr. Art McGarr
U.S. Geological Survey
Mail Stop 977
U.S. Geological Survey
Menlo Park, CA 94025

Dr. Keith L. McLaughlin
S-CUBED
A Division of Maxwell Laboratory
P.O. Box 1620
La Jolla, CA 92038-1620

Stephen Miller & Dr. Alexander Florence
SRI International
333 Ravenswood Avenue
Box AF 116
Menlo Park, CA 94025-3493

3

4

Thomas J. Sereno, Jr.
Science Application Int'l Corp.
10260 Campus Point Drive
San Diego, CA 92121

Dr. Michael Shore
Defense Nuclear Agency/SPSS
6801 Telegraph Road
Alexandria, VA 22310

Dr. Robert Shumway
University of California Davis
Division of Statistics
Davis, CA 95616

Dr. Matthew Sibol
Virginia Tech
Seismological Observatory
4044 Derring Hall
Blacksburg, VA 24061-0420

Prof. David G. Simpson
IRIS, Inc.
1616 North Fort Myer Drive
Suite 1050
Arlington, VA 22209

Donald L. Springer
Lawrence Livermore National Laboratory
L-025
P.O. Box 808
Livermore, CA 94550

Dr. Jeffrey Stevens
S-CUBED
A Division of Maxwell Laboratory
P.O. Box 1620
La Jolla, CA 92038-1620

Lt. Col. Jim Stobie
ATTN: AFOSR/NL
110 Duncan Avenue
Bolling AFB
Washington, DC 20332-0001

Prof. Brian Stump
Los Alamos National Laboratory
EES-3
Mail Stop C-335
Los Alamos, NM 87545

Prof. Jeremiah Sullivan
University of Illinois at Urbana-Champaign
Department of Physics
1110 West Green Street
Urbana, IL 61801

Prof. L. Sykes
Lamont-Doherty Geological Observatory
of Columbia University
Palisades, NY 10964

Dr. David Taylor
ENSCO, Inc.
445 Pineda Court
Melbourne, FL 32940

Dr. Steven R. Taylor
Los Alamos National Laboratory
P.O. Box 1663
Mail Stop C335
Los Alamos, NM 87545

Prof. Clifford Thurber
University of Wisconsin-Madison
Department of Geology & Geophysics
1215 West Dayton Street
Madison, WS 53706

Prof. M. Nafi Toksoz
Earth Resources Lab
Massachusetts Institute of Technology
42 Carleton Street
Cambridge, MA 02142

Dr. Larry Turnbull
CIA-OSWR/NED
Washington, DC 20505

Dr. Gregory van der Vink
IRIS, Inc.
1616 North Fort Myer Drive
Suite 1050
Arlington, VA 22209

Dr. Karl Veith
EG&G
5211 Auth Road
Suite 240
Suitland, MD 20746

Prof. Terry C. Wallace
Department of Geosciences
Building #77
University of Arizona
Tuscon, AZ 85721

Dr. Thomas Weaver
Los Alamos National Laboratory
P.O. Box 1663
Mail Stop C335
Los Alamos, NM 87545

5

Dr. William Wortman
Mission Research Corporation
8560 Cinderbed Road
Suite 700
Newington, VA 22122

Prof. Francis T. Wu
Department of Geological Sciences
State University of New York
 at Binghamton
Vestal, NY 13901

Prof Ru-Shan Wu
University of California, Santa Cruz
Earth Sciences Department
Santa Cruz
, CA 95064

ARPA, OASB/Library
3701 North Fairfax Drive
Arlington, VA 22203-1714

HQ DNA
ATTN: Technical Library
Washington, DC 20305

Defense Intelligence Agency
Directorate for Scientific & Technical Intelligence
ATTN: DTIB
Washington, DC 20340-6158

Defense Technical Information Center
Cameron Station
Alexandria, VA 22314 (2 Copies)

TACTEC
Battelle Memorial Institute
505 King Avenue
Columbus, OH 43201 (Final Report)

Phillips Laboratory
ATTN: XPG
29 Randolph Road
Hanscom AFB, MA 01731-3010

Phillips Laboratory
ATTN: GPE
29 Randolph Road
Hanscom AFB, MA 01731-3010

Phillips Laboratory
ATTN: TSML
5 Wright Street
Hanscom AFB, MA 01731-3004

Phillips Laboratory
ATTN: PL/SUL
3550 Aberdeen Ave SE
·Kirtland, NM 87117-5776 (2 copies)

Dr. Michel Bouchon
I.R.I.G.M.-B.P. 68
38402 St. Martin D'Heres
Cedex, FRANCE

Dr. Michel Campillo
Observatoire de Grenoble
I.R.I.G.M.-B.P. 53
38041 Grenoble, FRANCE

Dr. Kin Yip Chun
Geophysics Division
Physics Department
University of Toronto
Ontario, CANADA

Prof. Hans-Peter Harjes
.Institute for Geophysic
Ruhr University/Bochum
P.O. Box 102148
4630 Bochum 1, GERMANY

Prof. Eystein Husebye
NTNF/NORSAR
P.O. Box 51
N-2007 Kjeller, NORWAY

David Jepsen
Acting Head, Nuclear Monitoring Section
Bureau of Mineral Resources
Geology and Geophysics
G.P.O. Box 378, Canberra, AUSTRALIA

Ms. Eva Johannisson
Senior Research Officer
FOA
S-172 90 Sundbyberg, SWEDEN

Dr. Peter Marshall
Procurement Executive
Ministry of Defense
Blacknest, Brimpton
Reading FG7-FRS, UNITED KINGDOM

6

Dr. Bernard Massinon, Dr. Pierre Mechler
Societe Radiomana
27 rue Claude Bernard
75005 Paris, FRANCE (2 Copies)

Dr. Svein Mykkeltveit
NTNT/NORSAR
P.O. Box 51
N-2007 Kjeller, NORWAY (3 Copies)

Prof. Keith Priestley
University of Cambridge
Bullard Labs, Dept. of Earth Sciences
Madingley Rise, Madingley Road
Cambridge CB3 OEZ, ENGLAND

Dr. Jorg Schlittenhardt
Federal Institute for Geosciences & Nat'l Res.
Postfach 510153
D-30631 Hannover , GERMANY

Dr. Johannes Schweitzer
Institute of Geophysics
Ruhr University/Bochum
P.O. Box 1102148
4360 Bochum 1, GERMANY

Trust & Verify
VERTIC
Carrara House
20 Embankment Place
London WC2N 6NN, ENGLAND